A STUDY OF THE PROCESS $e^+e^- \to \mu^+\mu^-(\gamma)$ AT $\sqrt{s} < m(Z^\circ)$, $\sqrt{s} = 189$ GeV AND $\sqrt{s} = 192$ GeV USING THE OPAL DETECTOR AT LEP

Shaun Francis Ashby

Thesis submitted for the degree of
Doctor of Philosophy

School of Physics and Astronomy
Faculty of Science
University of Birmingham

August 2000

Synopsis

Measurements of cross-sections, angular distributions and forward-backward asymmetries of the process $e^+e^- \to \mu^+\mu^-(\gamma)$ have been made in two separate analyses which use data recorded using the OPAL detector at LEP in 1993, 1994, 1995 and during 1998 and 1999.

The first analysis involved separating radiative events from LEP I data to make measurements at an effective centre-of-mass energy below the Z° mass threshold. The second analysis involved using data at the highest available collision energies to make similar measurements. However, in this case the data were separated into two classes of event so that measurements could be made using events at full energy and those that had undergone initial state radiation (ISR).

The results from these analyses were compared to the results obtained from similar analyses preformed by the other LEP collaborations, and to the predictions of the standard model theory. No deviations from the theoretical expectations were found.

The Author's Contribution

The work presented in this thesis was performed by the author as a member of the OPAL Collaboration. Because there are many physicists and technicians involved in analysing data and maintaining the experimental apparatus, the input from an individual is sometimes difficult to distinguish. This section serves to highlight the contribution I have made to OPAL during the 3 years of my PhD.

During the first half of my PhD I studied the production of radiative muon pairs from Z° decays at LEP I using a limited data set. I later improved the analysis by including most of the data recorded at LEP I and the results are presented in the first part of this thesis. This was the first time an analysis of this type of process had been undertaken at OPAL using a large data set.

Throughout most of the period that I was permanently based at CERN, I was the Birmingham on-call expert for the muon endcap subdetector which was built in conjunction with the Rutherford Appleton Laboratory. The Birmingham University OPAL group is responsible for the maintenance of this subdetector, and for ensuring smooth day-to-day running and high data quality during the annual data-taking runs from April to November. My responsibilities included daily monitoring of gas and high voltage systems, attending status meetings and responding to problems 24 hrs a day.

While at CERN I was also a member of the LEP II Standard Model Working Group with responsibility for the analysis of muon pairs using the highest-energy data available.

The preliminary results were presented to the Working Group and international conferences, and final results published in leading journals. I also assisted with the tau pair analysis but the results, although published, are not featured in this thesis.

Acknowledgements

I would like to thank Professors John Kinson and John Dowell for giving me the chance to study in the Particle Physics Group at Birmingham. I am also grateful for the financial support provided by the Particle Physics and Astronomy Research Council (PPARC).

I am indebted to Peter Watkins and Nigel Watson for their helpful advice and encouragement throughout the past 3-plus years. I would also like to thank my colleagues in the OPAL Standard Model Working Group, especially Pat Ward and David Strom, for their advice during my stay at CERN. Thanks to my colleagues at Birmingham, especially Scott Talbot for help with analysing muons, John Wilson for help with understanding the Muon Endcaps and Dave Charlton for answering my frequent LINUX[(a)] questions.

I think it would have been impossible for me to have maintained any level of sanity without my friends in Geneva and Birmingham. While not an exhaustive list (sorry if you're not mentioned . . .), here are a few of those names I'll choose to record for posterity: Leanne and Andy for providing me with shelter when I decided to escape Birmingham and teaching me everything I ever wanted to know about motorbikes, Mark and Charlette for lifts from Crozet to CERN (definitely better than walking) and help with moving flat, Alain and Carolyn (les Canadiens) for helping me to improve my French, Nick ("Nick") Robertson (apologies for the head injury) and Dave ("Detective Inspector") Futyan (see you next year!) for company in the mountains, Mark ("Mark") Wigmore, Claire, Claire,

[(a)] Penguin Power!

Claire, Ant, Giles and the Birmingham crew and my fellow students at CERN: Alun, George, Tom, Steve, Russell and Kevin.

Finally, I would like to thank my mother and sister for their love and unfailing support during my time as a student.

Shaun, August 2000

This thesis is dedicated to my father, Ronald Frank Ashby,

June 21st 1943 - March 1st 1996.

Contents

List of Figures

List of Tables

Chapter 1

The Theory of Particle Interactions

1.1 Introduction

The search for an understanding of the origins of matter and the Universe has culminated in the development of a theory describing the fundamental interactions between elementary (pointlike) particles— the Standard Model, a non-Abelian gauge theory of the SU(3)⊗SU(2)⊗U(1) group. The standard model describes the behaviour of subnuclear matter at very small distance scales in the presence of the fundamental forces but presently excludes gravity.

This chapter describes the important aspects of this theory from which important predictions have been made with impressive accuracy.

1.2 The Standard Model

The standard model is a well-tested and verified physical theory describing the behaviour of two families of pointlike (*i.e.* structureless) fermions, *quarks* and *leptons*, when influenced by the weak, strong and electromagnetic forces. A fundamental interaction proceeds through exchange of massive or massless *gauge bosons* [1]. These field quanta can

be thought of as mediators of an interacting (non-Abelian) or non-interacting (Abelian) gauge field.

The members of the first generation of elementary particles are found in all matter. The other generations are only produced in high-energy collisions in research laboratories where they can be studied in detail, or as a result of cosmic ray collisions in the upper atmosphere.

1.2.1 Quarks and Leptons–the Matter Fields

The quarks and leptons, the matter fields of the standard electroweak theory, are arranged in three generations. There are six *flavours* of quarks – *up*(u), *down*(d), *strange*(s), *charm*(c), *bottom*(b) and *top*(t). The u, c and t quarks have charge $+(2/3)e$ while the d, s and b quarks have charge $-(1/3)e$. The top quark is the heaviest and was discovered in 1995 [2]. To complement the quarks there are six leptons– the electron (e^-), muon (μ^-) and tau (τ^-) plus a neutrino for each (ν_e, ν_μ and ν_τ). Each generation consists of lepton and quark doublets (Table 1.1). Both quarks and leptons are fermions and have half-integer spin (*i.e.* $S = 1/2\hbar$). Quarks can interact via the electromagnetic, weak and the strong forces, while leptons only participate in electromagnetic interactions if they are charged, and weak interactions.

Quarks are assigned a "colour" quantum number in quantum chromodynamics (QCD)- the field theory describing the strong interaction- and each can have three colour states, *red*, *green* and *blue*, and must form bound states which are colourless. The non-observation of free quarks is a direct result of "colour confinement" in the strong interaction. Colourless combinations can be formed from quark-antiquark states (*mesons*) or triplets of quarks or antiquarks (*baryons* and *antibaryons*). Together, these two groups describe all known types of hadronic matter. For each quark and lepton there is a corresponding antiparticle.

There is no experimental evidence to suggest that there are any further additions to the numbers of quark or lepton generations. This is deduced through measurements of the

width of the Z° resonance peak. Since each possible decay of the Z° boson to neutrinos contributes to the *invisible* width, any measurement of the Z° width can be used to infer the width for decays to invisible particles, assuming standard model couplings, and hence the number of light neutrinos (those having a mass less than $m(\mathrm{Z}^\circ)/2$).

	Generations			**Charge**
	I	II	III	
Quarks	$\begin{pmatrix} \mathrm{u} \\ \mathrm{d} \end{pmatrix}$	$\begin{pmatrix} \mathrm{c} \\ \mathrm{s} \end{pmatrix}$	$\begin{pmatrix} \mathrm{t} \\ \mathrm{b} \end{pmatrix}$	$+\frac{2}{3}$ $-\frac{1}{3}$
Leptons	$\begin{pmatrix} \nu_e \\ \mathrm{e}^- \end{pmatrix}$	$\begin{pmatrix} \nu_\mu \\ \mu^- \end{pmatrix}$	$\begin{pmatrix} \nu_\tau \\ \tau^- \end{pmatrix}$	0 -1

Table 1.1: The fundamental fermion generations.

1.2.2 Gauge Bosons–the Mediators of Fundamental Interactions

Four known interactions (or forces) exist in Nature–

- The weak interaction which gives rise to β radioactivity;
- The strong interaction which binds quarks into matter;
- The electromagnetic interaction which is responsible for coupling between charged particles;
- The gravitational interaction which holds the universe together.

The theoretical framework of quantum field theory suggests that the first three of these forces occur via exchange of vector particles known as gauge bosons which are field quanta

with spin $S = 1\hbar$. During each interaction, momentum and quantum numbers are conserved. The weak force is mediated by the W^+,W^- and Z° bosons. The electromagnetic force is mediated by the photon and an octet of gluons transmits the strong force. The range of the force is dependent upon the mass of the transmitting boson. For example, photons are massless and transmit the electromagnetic force over an infinite range whereas the weak force acts over a range of about 10^{-18}m as a result of the very high masses ($\approx$100 GeV) of the W^+,W^- and Z°. The comparative ranges of these interactions are shown in Table 1.2. In high energy physics experiments the effect of gravity can be

	Gauge Boson	Spin	Charge	Range
Strong	Gluons, $g_1 ... g_8$	1	0	∞
Electromagnetic	Photon, γ	1	0	∞
Weak	W^+	1	+1	10^{-18}m
	W^-	1	-1	
	Z°	1	0	
Gravitational	Graviton	2	0	∞

Table 1.2: The fundamental forces and their field quanta, with their respective ranges shown.

neglected because the influence on a sub-nuclear level is immeasurably small.

The graviton, for the present, remains undiscovered but because of the *attractive* nature of the interaction, knowledge of quantum mechanics allows us to predict that these quanta should have spin $2\hbar$.

1.3 Quantum Field Theory

Of three formulations of classical mechanics – Newtonian, Hamiltonian and Lagrangian – only two can be used to extend our understanding of classical systems to those of quantum systems. The Newtonian method relies on the use of inertial coordinates, for example using x and y, and forming equations of motion from these.

If the problem is redefined in terms of Lagrangian mechanics, any coordinate system can be used. Then it becomes much easier to describe the motion by introducing a *Lagrangian*, L, and using Lagrange's equations which are functions of the coordinates and L. The Lagrangian is given by

$$L = T - V \tag{1.1}$$

where T is the kinetic energy and V the potential energy. By using Lagrangian mechanics, the motion of a system can be described now by a single second-order differential equation.

The Hamiltonian method can further simplify the problem by deriving a quantity from the Lagrangian, H, which is the sum of kinetic and potential energy. This quantity is called the *Hamiltonian* and describes the dynamics of a system with first-order differential equations.

Both the Hamiltonian and Lagrangian methods can be used as a basis for quantum mechanics and quantum field theory. However, for relativistic quantum field theories in particle physics, the Lagrangian approach is used because of explicit Lorentz covariance.

The principle that quantities are conserved under certain transformations (for example, a translation or rotation) which can be described by group theory is central to the understanding of the structure of particle interactions. The descriptive mathematical framework for particle interactions is called a gauge theory which is a subclass of quantum field theory having the important property of local gauge invariance. The prototype gauge theory is quantum electrodynamics (QED) [3] which is the field theory for electromagnetism.

1.3.1 Quantum Electrodynamics

To determine the structure of electromagnetic interactions, gauge symmetry is imposed on the Lagrangian. Fermions are described by wavefunctions which are complex and have phase-dependency. This is also true for fermion fields. The Lagrangian should remain invariant under some transformation of this phase. These transformations take the form

$$\psi \rightarrow \psi' = e^{ie\phi(x)}\psi(x) \tag{1.2}$$

and reflect the fact that the phase ϕ of the wavefunction depends on the position in space-time. For this reason these are termed *local gauge transformations*, and their generators form a continuous U(1) gauge symmetry group.

For an electron of mass m which obeys the Dirac equation and propagates in free space with wavefunction $\psi(x)$, the Lagrangian has the form

$$L = i\bar{\psi}\gamma^{\mu}\partial_{\mu}\psi - m\bar{\psi}\psi \tag{1.3}$$

where $\partial_{\mu} = \frac{\partial}{\partial x^{\mu}}$ and γ^{μ} are the Dirac matrices [4].

Suppose that a new Lagrangian, L', is formed from the transformed wavefunction, ψ', instead of ψ. Because there is now a derivative term in x, clearly $L \neq L'$ because extra elements will be obtained when $\partial_{\mu}\psi'(x)$ is evaluated. Therefore, to ensure that any phase change leads to an invariant Lagrangian, the derivative ∂_{μ} should transform in the same way as the wavefunction. This is achieved through definition of a "covariant" derivative

$$D_{\mu} \equiv \partial_{\mu} - ieA_{\mu}(x) \tag{1.4}$$

The vector field $A_{\mu}(x)$ is a gauge field (sometimes called the *electromagnetic vector potential*) which transforms like

$$A_{\mu}(x) \rightarrow A_{\mu}(x) + \frac{1}{e}\partial_{\mu}\phi(x). \tag{1.5}$$

The second term cancels the extra term introduced in the transformed Lagrangian and local gauge invariance will be maintained when

$$D_{\mu}\psi \rightarrow D'_{\mu}\psi' = e^{ie\phi(x)}D_{\mu}\psi. \tag{1.6}$$

The gauge field has field quanta that transmit the electromagnetic force– the photon. Since the generators of the group are commutative, QED is an Abelian gauge theory. This implies that there are no interactions between photons (no photon-photon vertices in Feynman diagrams). Experiment supports this argument.

There are other gauge theories for the strong interaction (quantum chromodynamics [5]), which is based on the SU(3) group, and the unified theory of weak and electromagnetic interactions (the electroweak theory) which is presented in Section 1.5.

1.3.2 Renormalisation

Detailed mathematical theories can only be useful to experimenters if predictions can be verified. Physical calculations made from quantum field theory use perturbation theory. Such a technique allows predictions of amplitudes to be obtained to leading order by using "tree"-level Feynman graphs and excluding any QED or weak corrections.[(a)] For precise comparisons between data and theory, higher order radiative corrections must be included. The Feynman diagrams for e^+e^- annihilation are shown for the tree-level (lowest-order) process in Figure 1.1(a). Figure 1.1(b) shows a first-order contribution which is calculable to high precision. Other processes can include Feynman diagrams where there are internal loops of virtual $f\overline{f}$ pairs (Figure 1.1(c)), or internal photon lines (Figure 1.1(d)). When evaluating such diagrams, an integration over all possible energies and momenta of the loop particles must be performed. These terms lead to divergent integrals and unphysical amplitudes.

The divergences are avoided by a re-definition of certain parameters in the Lagrangian. Such re-definition is called renormalisation. Coupling constants found at the vertices of the loop diagrams are expressed as functions of their experimentally observed values, rather than some theoretical value. For example, the coupling to fermions in the photon exchange process $e^+e^- \to \gamma \to \ell^+\ell^-$ is proportional to the charge on the electron e. Experimenters

[(a)] Radiative corrections are discussed in Section 3.2

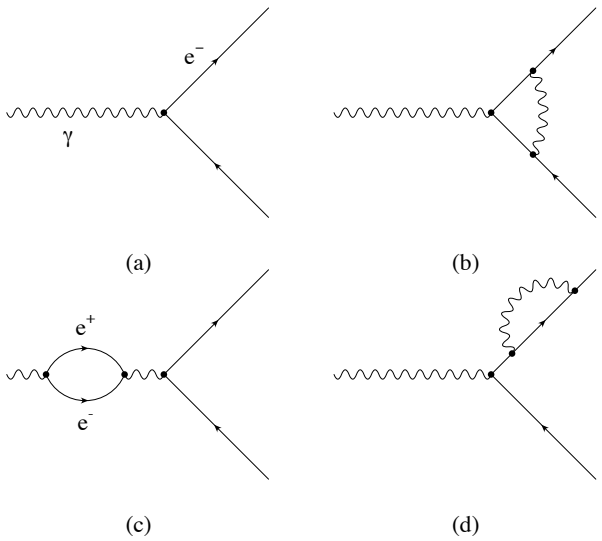

Figure 1.1: Feynman diagrams for tree-level and higher order contributions to e^+e^- annihilation:
(a) the tree-level (lowest order) diagram;
(b) a first-order perturbation;
(c) a process with an internal $f\overline{f}$ loop;
(d) a process with an internal photon line.
Diagrams (c) and (d) are typical divergent processes.

do not see effects of the "bare" charge of the electron because the electron continually emits and re-absorbs virtual photons which lead to more e^+e^- pairs. Therefore, the electron is surrounded by a virtual charge cloud and the bare charge is "screened". By assuming that the bare charge is infinite, the observed charge must become finite as a result of the screening effect. Using the measured charge in the Lagrangian, the divergences from the higher-order effects are absorbed. As the centre-of-mass energy increases, the larger momentum transfer (Q^2) of reactions gives values of the couplings that are nearer to the bare values. This effect manifests itself as the running of the electromagnetic (fine structure) constant α with energy.

All of the standard model gauge theories are renormalisable and this is true of all gauge theories, as demonstrated by Gerard t'Hooft [6] and Martinus Veltman who were awarded the Nobel Prize for Physics in 1999 for this work.

1.4 The CKM Matrix

The three quark generations are irreducible representations of the SU(2)⊗U(1) group algebra which describes electroweak theory. The quark states that propagate outwards from high energy collisions and are detected are called *mass eigenstates*. The states that are involved in the physics of the weak interaction are called *weak eigenstates*. The gauge bosons of the weak interaction couple to these weak eigenstates which were introduced to explain the absence of strangeness-changing neutral currents: generally, there are no flavour-changing neutral current interactions in the standard model. A 3×3 unitary transformation matrix called the Cabibbo-Kobayashi-Maskawa (CKM) matrix [7] relates the mass eigenstates and weak eigenstates (shown primed) through the expression

$$\begin{pmatrix} \mathrm{d}' \\ \mathrm{s}' \\ \mathrm{b}' \end{pmatrix} = \begin{pmatrix} V_{ud} & V_{us} & V_{ub} \\ V_{cd} & V_{cs} & V_{cb} \\ V_{td} & V_{ts} & V_{tb} \end{pmatrix} \begin{pmatrix} \mathrm{d} \\ \mathrm{s} \\ \mathrm{b} \end{pmatrix} \tag{1.7}$$

The current values [8] of the elements of the CKM matrix, obtained through experiment, are shown below.

$$\begin{pmatrix} V_{ud} & V_{us} & V_{ub} \\ V_{cd} & V_{cs} & V_{cb} \\ V_{td} & V_{ts} & V_{tb} \end{pmatrix} = \begin{pmatrix} 0.9745 \text{ to } 0.9760 & 0.217 \text{ to } 0.224 & 0.0018 \text{ to } 0.0045 \\ 0.217 \text{ to } 0.224 & 0.9737 \text{ to } 0.9753 & 0.036 \text{ to } 0.042 \\ 0.004 \text{ to } 0.013 & 0.035 \text{ to } 0.042 & 0.9991 \text{ to } 0.9994 \end{pmatrix}$$

The CKM matrix illustrates the decays of the heavier quarks into the lighter ones, *i.e.* decays from one family to another, by virtue of the high values of the diagonal terms V_{ud}, V_{cs} and V_{tb}. The decay t→b was the signature for the top quark and was the key to its discovery. The small off-diagonal terms indicate that cross-generational decays also occur but these are less probable. Each of the three lepton families conserves lepton number in all reactions.

1.5 Electroweak Theory

The electroweak theory [9] was proposed by Glashow-Salam-Weinberg and unifies the electromagnetic and the weak interactions, describing them using a Lagrangian that has gauge invariance under rotations that are generated by the SU(2)⊗U(1) gauge group.

The nature of weak interaction couplings to fermions depends on their chirality. The parity-violating form of the weak charged current implies that the coupling is to left-handed fermions only. The fermions are thus grouped into left-handed doublets and right-handed singlets (Table 1.3). There are no right-handed neutrino singlets because

Doublets:	$\begin{pmatrix} \nu_{\mathrm{e}} \\ \mathrm{e} \end{pmatrix}_L$	$\begin{pmatrix} \nu_{\mu} \\ \mu \end{pmatrix}_L$	$\begin{pmatrix} \nu_{\tau} \\ \tau \end{pmatrix}_L$	$\begin{pmatrix} \mathrm{u} \\ \mathrm{d}' \end{pmatrix}_L$	$\begin{pmatrix} \mathrm{c} \\ \mathrm{s}' \end{pmatrix}_L$	$\begin{pmatrix} \mathrm{t} \\ \mathrm{b}' \end{pmatrix}_L$
Singlets:	$(\mathrm{e})_{\mathrm{R}}$	$(\mu)_R$	$(\tau)_R$	$(\mathrm{u})_{\mathrm{R}}$	$(\mathrm{c})_{\mathrm{R}}$	$(\mathrm{t})_{\mathrm{R}}$
				$(\mathrm{d})_{\mathrm{R}}$	$(\mathrm{s})_{\mathrm{R}}$	$(\mathrm{b})_{\mathrm{R}}$

Table 1.3: The assignment of left-handed weak isospin doublets and right-handed weak isospin singlets in electroweak theory.

the neutrino is understood to be massless and therefore it would be impossible to boost to a reference frame in which the observer could view the neutrino with right-hand spin. The $\mathrm{SU}(2)_L$ transformations are rotations in weak isospin space and act on the left-handed isospin doublets, rotating one element into another; an example would be e^- into ν_{e} and u into d′ for the first generation of leptons and quarks respectively. The transformations have the form

$$\begin{pmatrix} \nu_{\mathrm{e}} \\ \mathrm{e} \end{pmatrix}_L \rightarrow \begin{pmatrix} \nu_{\mathrm{e}} \\ \mathrm{e} \end{pmatrix}_L e^{i\phi_\alpha(x)\tau^\alpha} \tag{1.8}$$

and similarly for the other generations. Here, the generators of the group are the Pauli

matrices τ^{α} (where α= 1,2,3). To maintain the gauge invariance after this kind of transformation, three gauge fields must be introduced. The covariant derivative has the form

$$D_{\mu} \equiv \partial_{\mu} + ig\frac{1}{2}\tau.\mathbf{W}_{\mu} \tag{1.9}$$

The gauge fields $\mathrm{W}_{\mu}^{\alpha}$ (α= 1,2,3) couple with strength g to the left-handed doublets. Two of these fields can immediately be associated with the carriers of the charged-current interactions, the W^{+} and W^{-} bosons. There is an anomaly, however, when assigning a field describing weak neutral currents since the Z° couples to both right and left-handed particles. The solution is an additional unitary group that couples to weak hypercharge Y, $\mathrm{U}(1)_{Y}$, related to the generator of the group Q by

$$Q = T^{3} + \frac{Y}{2}. \tag{1.10}$$

where T^{3} is the third component of weak isospin. This ensures that, by imposing local gauge invariance under $\mathrm{SU}(2)_{L}\otimes\ \mathrm{U}(1)_{Y}$ transformations, two extra neutral gauge fields are developed. The photon field, A_{μ}, and the neutral current field, Z_{μ}, are generated by two linear combinations of the neutral weak isospin field, W^{3}, and the weak hypercharge field B

$$Z_{\mu} = W^{3}\cos\theta_{W} - B\sin\theta_{W} \tag{1.11}$$

$$A_{\mu} = W^{3}\sin\theta_{W} + B\cos\theta_{W} \tag{1.12}$$

The degree of mixing between the fields is given by the weak mixing angle, θ_{W}. The angle relates the electromagnetic and weak field coupling strengths via

$$e = g\sin\theta_{\mathrm{W}} \tag{1.13}$$

where e is the proton charge and can be determined by experiment.

Unfortunately, the electroweak Lagrangian does not contain explicit mass terms for the fermions, apparently contradicting our experience of a world where the fundamental fermions are known to be massive. By simply adding a mass term to the Lagrangian, the gauge invariance and renormalisability of the theory are lost. How do the physical particle states acquire masses? The answer to this question is believed to be explained satisfactorily by the Higgs mechanism and spontaneous electroweak symmetry breaking.

1.6 The Higgs Mechanism

The Higgs mechanism [10] is thought to be a suitable way to explain how three gauge bosons and the matter fields in the standard model acquire mass. The electroweak gauge symmetry is "spontaneously broken" at an energy scale comparable to the boson masses whereby the residual symmetry group is $\mathrm{U}(1)_Y$ and the photon field remains massless. The other gauge bosons acquire their large masses with the introduction of a scalar Higgs field. The presence of this extra field ensures that gauge invariance is maintained and permits spontaneous breaking of the symmetry.

In the standard model, the Higgs sector of the electroweak Lagrangian consists of four complex scalar fields configured as a weak isospin doublet

$$\phi = \frac{1}{\sqrt{2}} \begin{pmatrix} \phi_1 + i\phi_2 \\ \phi_3 + i\phi_4 \end{pmatrix} \tag{1.14}$$

The interaction potential energy V is

$$V(\phi^\dagger\phi) = -\mu^2\phi^\dagger\phi + \lambda(\phi^\dagger\phi)^2 \tag{1.15}$$

with μ and λ constants. The vacuum state is characterised by a non-zero expectation value because the Higgs field potential has the "wine bottle" shape with minima at $\mu^2/2\lambda$ (Figure 1.2). The important aspect here is that, using the minimum expectation value

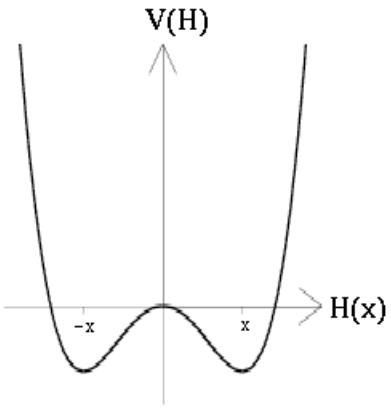

Figure 1.2: The form of the Higgs field potential. The minima are situated at $x=\pm\mu^2/2\lambda$ where μ and λ are constants.

of the Higgs field and applying perturbation theory, extra terms are generated which, when included in the electroweak Lagrangian, provide suitable masses for the weak gauge bosons. The symmetry of the Lagrangian itself is not broken (so it remains gauge invariant), but the underlying electroweak gauge symmetry is broken spontaneously when the Lagrangian is in the vacuum-state. Three of the four fields are absorbed and generate the boson masses, but one remains. This leftover field is that of the Higgs boson, the quanta of the Higgs field.

The discovery of the Higgs boson is crucial for the standard model.

1.6.1 Constraints on the Higgs Mass, m_H

There are a number of constraints on the Higgs mass that are imposed by both experimental evidence and by theoretical requirements. All of the LEP experiments are presently undertaking direct searches for the Higgs particle. There is no direct evidence in currently available data to support its existence but for each increase in accelerator energy, the lower limit on the Higgs mass is increased. The present lower limit on the Higgs mass using data from all LEP experiments is 107.9 GeV/c^2 at a 95% confidence level [11]. Figure 1.3

shows the m_H range already excluded by direct searches at LEP and the constraints on m_H through indirect measurements using global fits to LEP I electroweak data. In addition, the precise measurements of lepton-pair asymmetries made during the LEP I phase further constrain m_H through knowledge of the electroweak radiative corrections. This indicates a preference for a light Higgs boson having a mass of around 130 GeV (Figure 1.4). The search for the Higgs boson will continue post-LEP at the TEVATRON collider at the Fermi National Laboratory in the United States, and at the next particle collider to be developed at CERN– the Large Hadron Collider (LHC) – a proton-proton machine which will operate at a centre-of-mass energy of 14 TeV.

1.7 What Lies Beyond the Standard Model?

There is general acceptance in the high energy physics community that, although it is very successful, the standard model may not be the complete picture but rather the low-energy limit of a more complete theory. There are several factors that influence this line of thought. Firstly, there are 19 free parameters in the standard model that are not predicted and must be measured by experiment and input by hand. This is obviously not an ideal situation for a final theory. Recent measurements of neutrino oscillations using atmospheric neutrinos from the Super-Kamiokande [14] experiment also appear to suggest that the neutrino may in fact have a very small mass. The impact of this discovery on the standard model is not yet known.

The difference in energy scale between the standard model boson masses and the expected unification scale is a factor of 10^{13}. This is known as the *Hierarchy Problem*. At 10^{15} GeV, the coupling constants in the strong and electroweak theories are the same and lead to Grand Unification of these forces. There is also a considerable difference between the magnitudes of the fermion and boson masses. Any new theory must provide solutions to these factors and also introduce gravity into the framework. At the Planck scale (of order 10^{15} GeV), all four forces are united and would therefore be described by a single

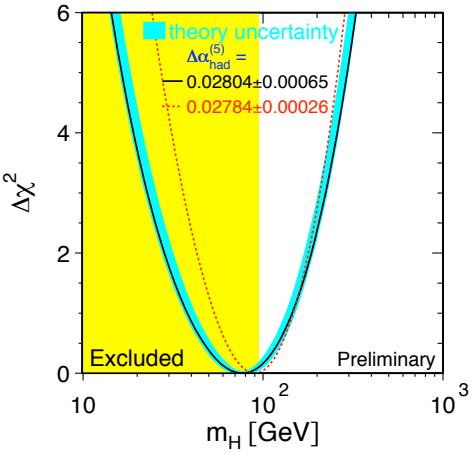

Figure 1.3: The change in the χ^2 of a global fit to electroweak data for possible Higgs masses in the range $10 < m_H < 400$ GeV. The light grey shading shows the Higgs mass region already excluded by direct searches at LEP. The dark grey band indicates the uncertainty in the fit arising from missing higher-order corrections. Figure taken from [12].

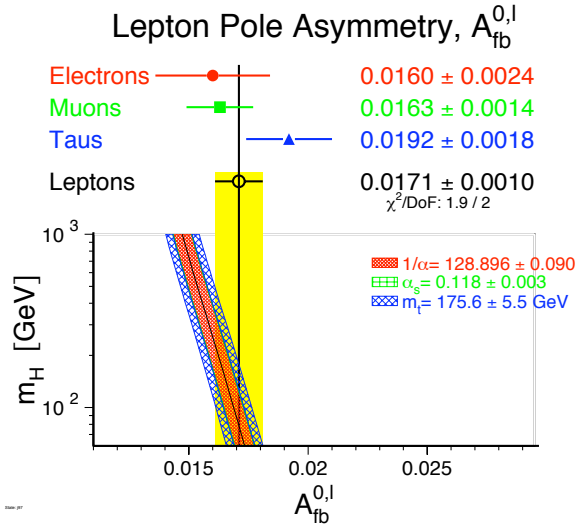

Figure 1.4: The limits on the Higgs mass from precision measurements of lepton-pair forward-backward asymmetry at LEP. Figure taken from [13].

"Theory of Everything".

The Minimal Supersymmetric Standard Model (MSSM) is the simplest theoretical model based on a theory called Supersymmetry (SUSY) and is a possible candidate for a unified theory. Supersymmetry postulates that every standard model particle has a partner with the same quantum numbers, but with spin differing by $1/2\hbar$. Thus, all standard model fermions have supersymmetric partners that are bosons, and standard model bosons have partners that are fermions. The supersymmetric bosons are called sleptons and squarks and the forces are mediated by fermions called gauginos.

Supersymmetry is favoured for several reasons. Because the fermionic and bosonic terms in the electroweak radiative corrections to the Higgs mass and $W^{\pm}$ or Z° processes at energies around 1 TeV have opposite sign, cancellations occur which ensure that the divergent integrals are removed and renormalisability maintained. To develop supersymmetry as a local symmetry would require the introduction of a spin-2 gauge field and this therefore facilitates the inclusion of the gravitational interaction into a gauge theoretical framework.

Searches for superpartners in the LEP experiments continue but no evidence has yet been found. This implies that SUSY must be a broken symmetry to allow the superpartner masses to be larger than their standard model counterparts.

Chapter 2

LEP and Particle Detection at OPAL

Following the discovery of the $W^{\pm}$ and Z° intermediate vector bosons by the UA1 and UA2 Collaborations in 1983, the construction of an $e^{+}e^{-}$ collider at CERN began. Known as the Large Electron-Positron (LEP) Collider [15], it straddles the French-Swiss border and is the largest particle accelerator in the world.

2.1 The Large Electron-Positron Collider

LEP is a synchrotron particle accelerator designed to collide electrons and positrons in the centre-of-mass energy range of 80–200 GeV. Situated in an approximately circular tunnel, it has a circumference of 27km and lies at a depth ranging from 51m to 143m below ground level. The two counter-rotating beams are made to collide at four of the eight intersections in the ring.[(a)] At these points are sited the four experimental detectors—ALEPH [16], DELPHI [17], L3 [18] and OPAL [19].

[(a)] At the odd-numbered points the beams are separated vertically using electrostatic separators.

2.1.1 Particle Injection

Electrons and positrons must be produced, accumulated and pre-accelerated before injection into LEP. The first stage of this process, production of the particles themselves, begins in the LEP Injector Linac (LIL). Electrons are produced readily through thermionic emission from a heated cathode and are accelerated toward a tungsten target, attaining an energy of 200 MeV before rapid deceleration on striking the tungsten. The emitted bremsstrahlung radiation creates electron-positron pairs, from which positrons are separated using a magnetic field. Both the electrons and positrons are accelerated to 600 MeV in a second linear accelerator before storage in the Electron Positron Accumulator (EPA). Once there are sufficient numbers of each species available, they are injected into the Proton Synchrotron (PS) and accelerated from 600 MeV to 3.5 GeV. The Super Proton Synchrotron (SPS) increases their energy to 20 GeV before the final stage of introduction into the LEP ring where acceleration to the desired interaction energy occurs. A schematic of the accelerators at CERN is shown in Figure 2.1.

2.1.2 Particle Acceleration

Accelerated charged particles emit synchrotron radiation and thus lose energy. The energy loss per electron, per cycle within LEP is a function of the electron energy E, the electron mass and the radius of the orbit R, and is given by $\Delta E \propto E^4/m^4R$. This amounts to hundreds of MeV. Thus, with large numbers of particles, the energy loss is appreciable: a power output of order 1kW is produced as synchrotron radiation per metre of the beampipe. In order to minimise this loss, a large diameter ring was necessary. The energy loss is counteracted by the use of radio frequency (RF) cavities which use electromagnetic waves to accelerate the bunches of (charged) particles as they pass through each cavity.

The evolution of LEP has taken place through several phases. The initial phase, known as LEP I, ran from 1989 to 1995 at a centre-of-mass energy centred on the Z° production threshold, with some "scanning" on either side of the pole. At this time,

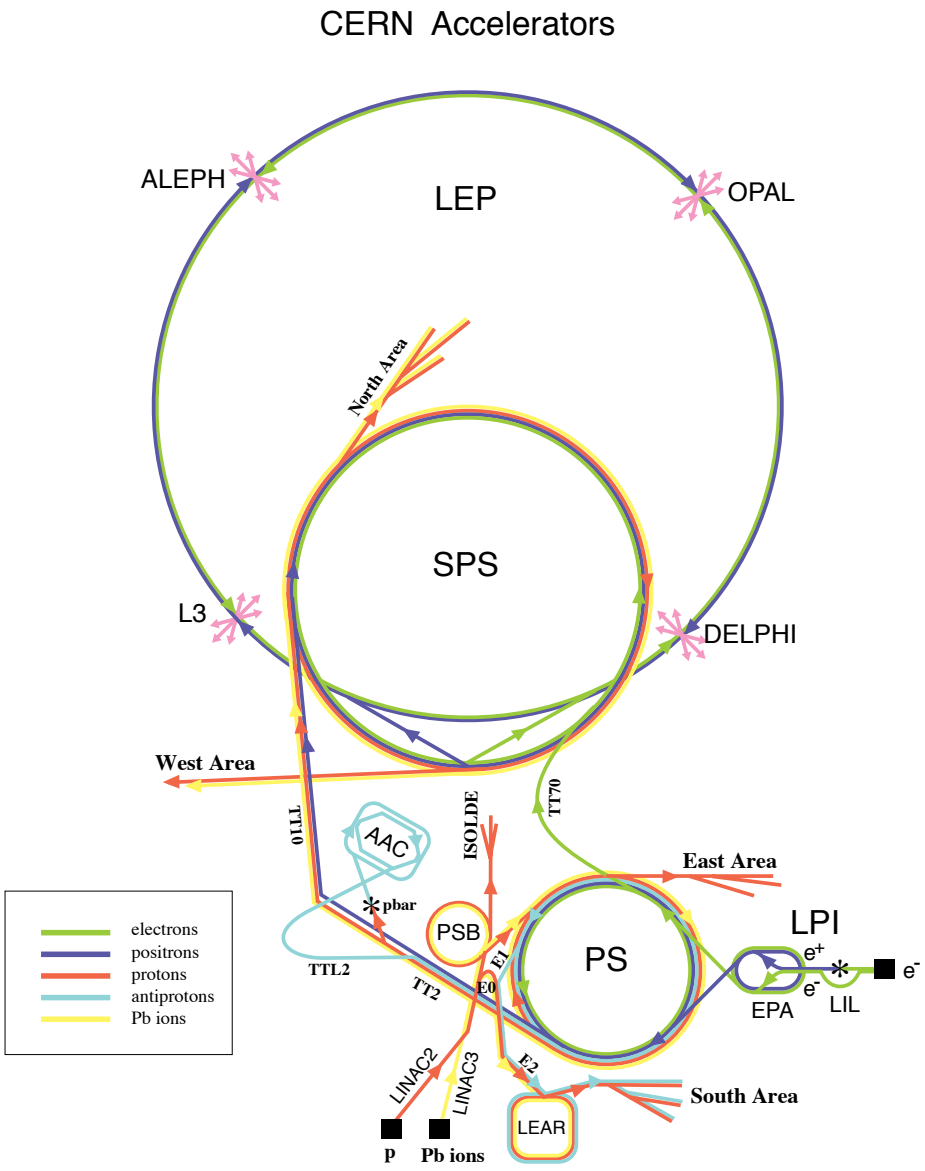

LEP: Large Electron Positron collider
SPS: Super Proton Synchrotron
AAC: Antiproton Accumulator Complex
ISOLDE: Isotope Separator OnLine DEvice
PSB: Proton Synchrotron Booster
PS: Proton Synchrotron
LPI: Lep Pre-Injector
EPA: Electron Positron Accumulator
LIL: Lep Injector Linac
LINAC: LINear ACcelerator
LEAR: Low Energy Antiproton Ring

Rudolf LEY, PS Division, CERN, 02.09.96

Figure 2.1: The accelerator layout at CERN.

LEP had 128 copper RF cavities powered by 16 1MW klystrons to provide the necessary accelerating power. During 1995 running, an energy of 136 GeV was attained and this intermediate phase, known as LEP1.5, was followed by higher energy running in 1996-1998 at 161 GeV, 172 GeV, 184 GeV and 189 GeV – the LEP II phase. These higher energies are sufficient to produce W^+W^- pairs. Because of increased energy losses at higher energy, many copper radio-frequency cavities were replaced with more efficient, niobium-coated, superconducting cavities both at the beginning, and throughout the LEP II era. In 1999, approximately 30.0 pb^{-1} of data was collected at $\sqrt{s} = 192$ GeV and 78.0 pb^{-1} at $\sqrt{s} = 196$ GeV. With most of the remaining copper RF cavities replaced by superconducting ones, the extra available accelerating gradient permitted the design target of 100 GeV per beam to be exceeded, with 79.0 pb^{-1} of data collected at $\sqrt{s} = 200$ GeV and 38.0 pb^{-1} collected at $\sqrt{s} = 202$ GeV. In 2000, increases in beam energy have been achieved by fine-tuning machine operating parameters: around 80 pb^{-1} of data has been collected at an average $\sqrt{s} = 205$ GeV and 95 pb^{-1} at $\sqrt{s} = 207$ GeV. Beyond 2000, LEP will be decommissioned to be replaced by the Large Hadron Collider (LHC) which will be situated in the LEP tunnel.

2.1.3 Beam Transport

To ensure beam circulation for a substantial period of time to enable high statistics data to be collected, the beams are contained within a vacuum pipe at a pressure of 3×10^{-9} torr. This very low pressure is attained through both the use of vacuum pumps and non-evaporable "getter strips". The strips are made from a material that can locally absorb stray gas molecules. The beams are guided by an arrangement of 3000 bending (dipole) magnets and 2000 focussing (quadrupole) magnets surrounding the beampipe.

Focussing is achieved with pairs of quadrupoles. One quadrupole focusses in the vertical plane while defocussing in the horizontal plane and the second provides focussing in the horizontal plane and defocussing in the vertical plane. The defocussing action of

the second quadrupole is of smaller magnitude than the focussing action of the first in the particular plane while the focussing action of the second quadrupole is of larger magnitude than the defocussing effect of the first. Thus a net focussing effect is applied to the beam. This is important for several reasons: firstly, to minimise background processes due to off-momentum particles, and secondly to increase the luminosity of the accelerator by reducing the cross-sectional area of the beam.

2.2 The OPAL Detector and Subdetectors

The OPAL (Omni-Purpose Apparatus for LEP) detector (Figure 2.2) is a multi-purpose detector able to detect final states resulting from Z° decays with good resolution in momentum and energy determination, over an almost 4π solid angle.

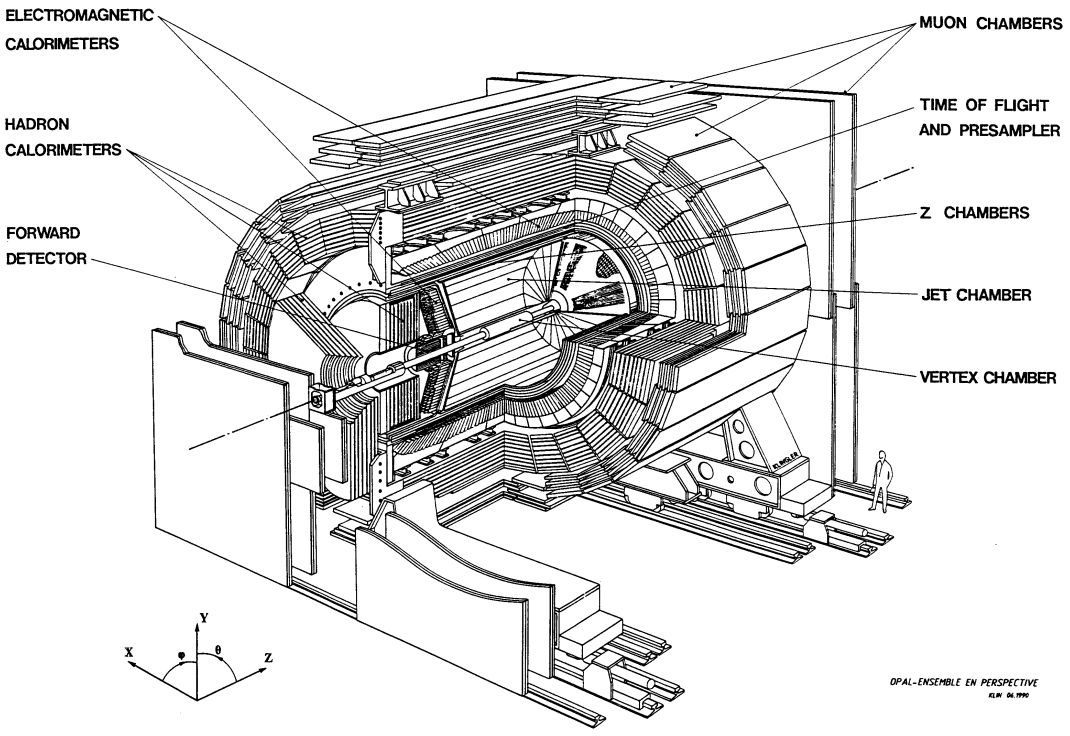

Figure 2.2: The OPAL detector.

In an ideal world, it would be possible to have a homogeneous particle detector which could detect and identify all particles perfectly. Although there are some geometric limitations in all detectors, for example, poor coverage near to the beam pipe, present-day detectors are built from many sub-components. Each of these is designed with a specific range of tasks in mind to ensure a high overall efficiency. The OPAL detector consists of a series of cylindrical detectors, starting at the beam-pipe near the vertex and moving outwards to the final layer, the muon barrel. The ends are capped by additional muon chambers. A cutaway view of the detector, showing the layers of subdetectors, is shown in Figure 2.3. The detector can be divided into two main parts: the central detector and the outer subdetectors. The components of these two, the subdetectors, are described in more detail in the following sections.

In describing the subdetectors, the OPAL coordinate system is used. This is a right handed Cartesian system, with the origin defined as the centre of the jet chamber (CJ) at the approximate position of the e^+e^- interaction point. The direction of the electron beam passing through OPAL defines the z-axis, with the x-axis pointing towards the centre of the LEP ring and the y-axis being approximately vertical.[(b)]

2.2.1 Central Detector

The determination of the position of the primary vertex of a particle interaction is particularly important for identification of short-lived particles like the τ lepton or mesons containing charm or bottom quarks. The purpose of the central detector is to do this accurately and enable reconstruction of particle tracks in 3-dimensions.

The central detector consists of a 0.11cm thick beryllium beam-pipe surrounded by a microvertex detector (in close proximity to the beam pipe) and, enclosed in a pressure vessel, three drift chambers: the vertex chamber (CV), the jet chamber (CJ), and the Z-chambers (CZ). The pressure vessel is maintained at a pressure of 4bar and is contained

[(b)] In fact, the LEP ring is inclined at 0.8° to the horizontal

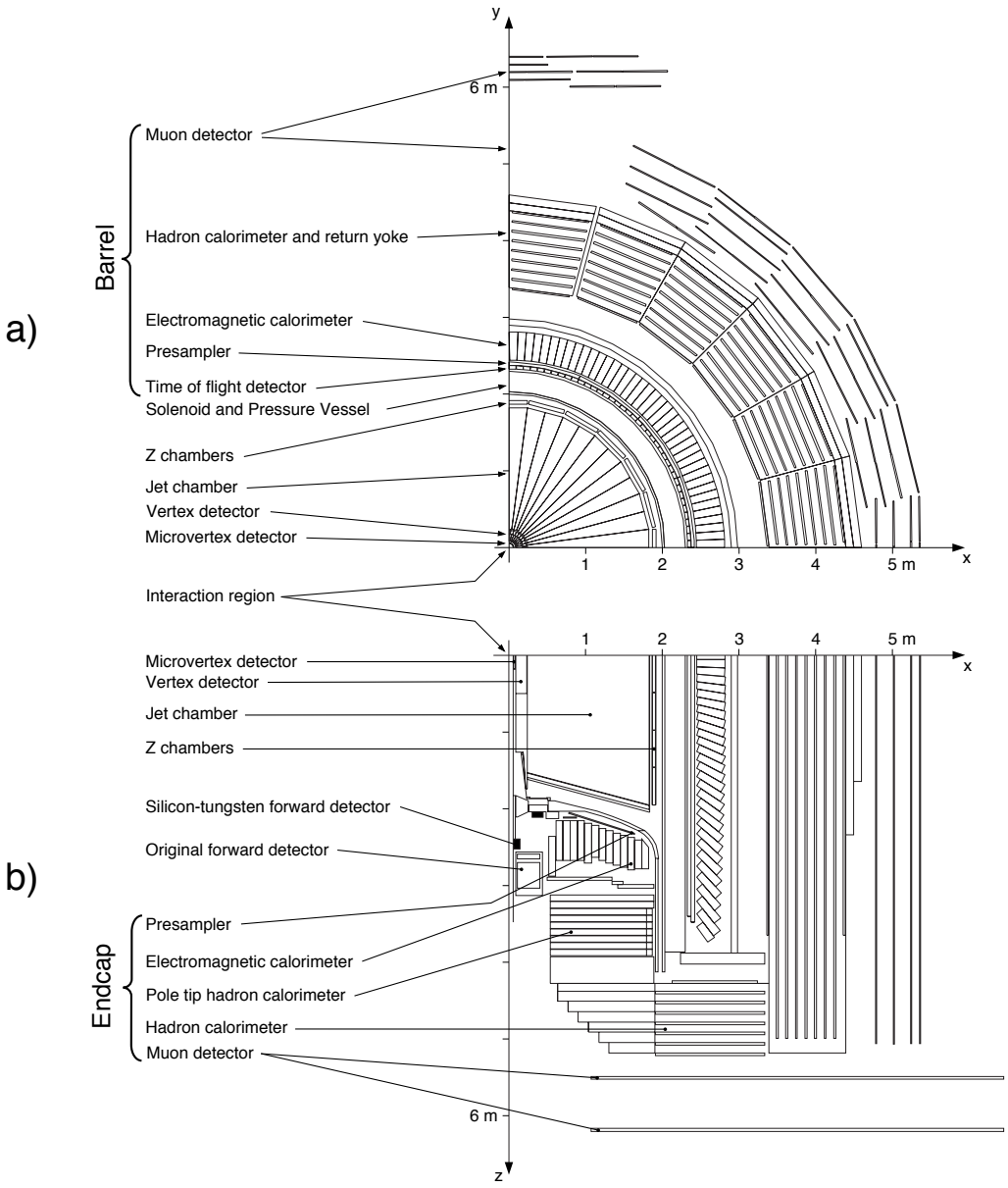

Figure 2.3: Cutaway of the OPAL detector showing the barrel (a) and endcap (b) regions.

inside a solenoidal magnet coil. The presence of the axial magnetic field allows particle charge and momentum to be determined from the curvature of the reconstructed particle track. Particle identification is also possible by using the measure of energy loss, $\mathrm{d}E/\mathrm{d}x$.

Silicon Microvertex Detector

The silicon microvertex detector (SI) [20] was first installed in 1991, with further improvements introduced in 1993, 1995 and 1996. Initially used to provide just $r-\phi$ co-ordinates, the 1993 upgrade additionally allowed measurement of the $r-z$ co-ordinates.

The present configuration consists of two barrels of single-sided microstrip detectors, constructed from silicon, arranged at radii of 6.0cm and 7.5cm from the centre of the beam pipe. There are 12 ladders in the inner barrel, 15 in the outer barrel and each ladder is 18cm long, consisting of 5 silicon wafers connected in a 'daisy-chain' format. The ladders are also tilted to close gaps in ϕ. This gives a spatial resolution of 5-10μm in both planes which is necessary for precise measurements of short-lived particles, accurate reconstruction of vertices and determination of track parameters.

Central Vertex Detector

This vertex detector [21] is a high precision cylindrical drift chamber, 100cm long with an inner radius of 10.3cm and an outer radius of 23.5cm, lying between the microvertex detector and the jet chamber. It is divided into two concentric cylindrical layers, representing 36 sectors in azimuthal angle. The inner layer has groups of 12 wires running parallel to the beam axis, termed 'axial wires', while the outer layer has 6 wires, 'stereo wires', inclined at 4 degrees to the beam axis. Precise measurement of the drift time onto the axial wires permits calculation of the position in $r-\phi$ with a resolution of 55μm. The combination of axial and stereo wires allows determination of the position in z with a resolution of 700μm.

Jet Chamber

The jet chamber [22] is a cylindrical multiwire detector which is 4m in length. It has an inner radius of 24.5cm, an outer radius of 185cm and is divided into 24 sectors of equal azimuthal angle. Each sector has 159 sense wires (the anode plane) parallel to the beam axis with an inter-wire spacing of 10mm. The anode plane runs through the centre of the sector. In between the sense wires are the potential wires: the cathode planes lie at an angle of 7.5° degrees with respect to these wires. The sense wires are staggered by $\pm 100\mu$m, alternately to the left and right hand side of the plane determined by the potential wires. Since the jet chamber is a multihit chamber and records more than just the closest ionisation site to the wires, much more information can be gained. A charged particle passing through the detector produces local ionisation of the gas mixture. The time taken for drift electrons to move towards the anode plane and reach the wires fixes the track coordinate in $r - \phi$, while the relative fractions of the total charge recorded at each end of the wire yields the z coordinate. The total charge collected on the wire can permit a determination of the rate of energy loss, $\mathrm{d}E/\mathrm{d}x$. This is a very important tool for the discrimination of different particle types, especially hadrons. Figure 2.4 shows an example of a $\mathrm{d}E/\mathrm{d}x$ plot for multihadronic tracks and muon-pairs. An average resolution in $r - \phi$ of 135μm and in z of 6cm is attainable. The accuracy of track reconstruction is degraded in the region $|\cos\theta| > 0.73$, since there are fewer hits likely if a particle passes through this region of the detector. Maximum information is gained from tracks contained within the detector volume, $|\cos\theta| < 0.73$, where hits can be recorded on all 159 sense wires.

Z-Chambers

The Z-chambers (CZ) [23] form a barrel around the jet chamber and are the last of the central subdetectors to lie within the magnet. Angular coverage is over the region $|\cos\theta| < 0.72$. Constructed from 24 panels 4m in length, each divided into 8 drift cells,

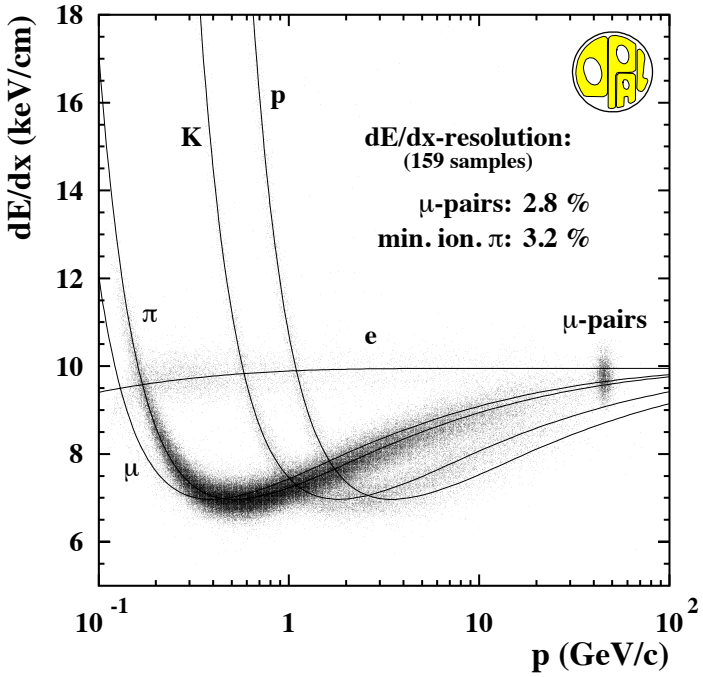

Figure 2.4: Scatter plot of $\mathrm{d}E/\mathrm{d}x$ against track momentum p for multihadrons and $\mu^+\mu^-$ pairs. The solid lines show the expected functional form. Also indicated are the $\mathrm{d}E/\mathrm{d}x$ resolutions for pions in multihadronic Z° decays, having momenta p = 0.4 - 0.8 GeV/c, and muon pairs having the maximum number of hits in the jet chamber.

these chambers provide a precise measurement of the z-coordinate of tracks leaving the jet chamber. Each drift cell has six sense wires, perpendicular to the beam axis, with the measurement of drift time giving the z-coordinate of charged tracks with a resolution of 300μm. A coarser $r-\phi$ measurement, with a resolution of 15mm, is also achieved by reading out each end of the resistive anode wires.

2.2.2 The OPAL Magnet

The OPAL magnet is a water-cooled solenoid designed to produce a field of 0.435T parallel to the z-axis which is uniform throughout the central detector volume to within a fraction of a percent. The coil itself is wound from a hollow aluminium conductor which is insulated using epoxy-impregnated glass tape. The iron return yoke, constructed from steel plates,

also acts as a showering material for the hadron calorimeter which lies beyond the magnet coil. A current of $\approx$ 7000A is supplied to produce the required field. The residual field outside the magnet is reduced by utilising a coil wound as a single unit (stray magnetic flux has a detrimental effect on field-sensitive detector instrumentation like photomultiplier tubes).

2.2.3 Time-Of-Flight Counters

The time-of-flight (TOF) system is split into two detectors covering the barrel and endcap regions. The barrel time-of-flight detector (TB) comprises 160 scintillation counters of length 684cm, arranged around the magnet coil with angular coverage of the region $|\cos\theta| < 0.82$. This provides trigger information, some low-momentum (p = 0.6 - 2.5 GeV/c) charged particle identification and aids in cosmic ray background rejection. The latter is achieved for muon pairs by measuring the time difference between hits on opposite sides of the central detector. Time differences much different from zero indicate anomalous events and these are flagged as such by the event reconstruction software (see Section 2.3.3). The timing resolution of the barrel detector system is approximately 200ps.

The Tile Endcap/MIP Plug

The tile endcap (TE) [24] was added to OPAL in 1998 to improve the trigger redundancy in the forward region and provide extra time-of-flight information for improved cosmic rejection. It consists of a layer of scintillating tiles, 10mm thick, with light output via wavelength-shifting optical fibres to photomultiplier tubes situated outside the magnet coil.

The Minimum Ionising Particle (MIP) plug consists of 4 layers of scintillator tiles at each end of the forward region. Two layers (separated by 5mm of lead to reduce the effects of synchrotron radiation) are located near to the forward detector, with an angular acceptance of 126-220 milliradians. The third layer, which lies behind the first two layers,

has an acceptance of 45-160 milliradians. These three layers are divided into quadrants in ϕ. The final outermost layer, between the silicon-tungsten luminosity monitor and the forward detector, covers the angular region 43-130 milliradians and is divided into octants in ϕ. The TE/MIP plug is shown in Figure 2.5.

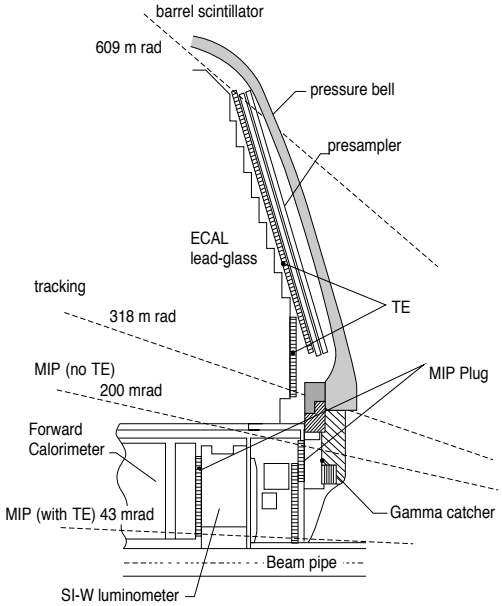

Figure 2.5: The tile endcap (TE) subdetector configuration.

2.2.4 Electromagnetic Calorimeter

The role of the electromagnetic calorimeter (ECAL) is to detect and measure the energies of photons and electrons. It is a lead-glass total absorption calorimeter situated between the central detector and the magnet yoke, comprising a barrel detector and two endcap arrays. When combined with the two lead scintillator calorimeters of the forward detector, angular acceptance for detection of photons and electrons approaches 99% of the solid angle. As the charged leptons or photons pass through the dense lead glass, significant deceleration occurs producing Bremsstrahlung radiation. These photons create electron-positron pairs which also undergo deceleration. This "showering" process continues until all of the energy of the incident particle is absorbed. The Čerenkov radiation emitted by

the relativistic charged particles passing through the lead glass is recorded by the phototubes: the signal read out is proportional to the energy deposited in the calorimeter. There are approximately 1.5 radiation lengths of aluminium between the central detector and the barrel lead glass which can initiate showering prematurely. Presampling devices are used in front of the barrel and endcap electromagnetic detectors to measure the position and energy of these showers. This improves the energy and spatial resolution of the calorimetry, yielding additional discrimination between photons and π^0 and between electrons and hadrons.

Presampler Barrel

The presampler barrel (PB) [25] is an arrangement of 16 chambers of length 662cm, forming a cylinder of radius 239cm. Each chamber is a double layer of streamer chambers, with anode wires running parallel to the z-axis and 1cm wide cathode strips positioned at 45 degrees. Read out of each end of the strips and measurement of the charge at each end of the wire gives the spatial position with a resolution of 2mm. The calorimeter shower energy can be corrected by using the PB hit information: the hit multiplicity is approximately proportional to the energy deposited in material at the front of the presampler.

Electromagnetic Calorimeter Barrel

The electromagnetic calorimeter barrel detector (EB) [26] is a cylindrical array of lead glass blocks, 9440 in total, with an angular acceptance of $|\cos\theta| < 0.82$. Each block has a cross section of 10×10 cm^2 and a depth of 37 cm. In order to maximise detection efficiency the longitudinal axis of each block is angled towards the interaction region. The focus of this pointing geometry is slightly offset from the collision point in order to minimise particle losses in the gaps between blocks. Čerenkov light is collected by 3in diameter photomultiplier tubes mounted at the base of the blocks. There are about 24 radiation lengths of material between the front and back of the lead glass: this gives

almost total absorption of electrons and photons with an intrinsic energy resolution of $\sigma_E/E \simeq 15\% \ /\sqrt{E}$.

Presampler Endcaps

The presamplers in the endcap region (PE) [27] use narrow-gap multiwire proportional chambers instead of the limited streamer mode chambers due to a lack of space. There are 32 chambers arranged in 16 sectors. The wires lie perpendicular to the beam axis and strips run radially on one side of each chamber. A position resolution of 4mm is achieved.

Electromagnetic Calorimeter Endcaps

The electromagnetic calorimeter endcaps (EE) [28] are dome-shaped arrays, each comprising 1132 lead glass blocks. There are three different depths of block– 38cm, 42cm and 52cm, with the block cross section being approximately the same as in the barrel. The endcaps extend the angular acceptance of the ECAL detector to $|\cos\theta| < 0.98$. Čerenkov light is recorded using vacuum photo-triodes, not photomultilier tubes, because the endcap arrays are contained within the full magnetic field generated by the OPAL solenoid. A non-pointing geometry is applied to the assembly of blocks in the endcap which results in a different form of shower development compared to the barrel. Intrinsic energy resolution in the endcaps is $\sigma_E/E \simeq 20\% \ /\sqrt{E}$.

2.2.5 Hadron Calorimeter

The purpose of the hadronic calorimeter (HCAL) is to determine the energy of hadronic decay products. The calorimeter has three components: the hadron barrel, hadron endcap and hadron poletip detectors, each covering different $\cos\theta$ regions. The detectors, positioned between layers of the magnet return yoke, form a sampling calorimeter and give coverage of 97% of 4π, offering at least 4 interaction lengths of iron absorber to particles emerging from the electromagnetic calorimeter. This detector structure ensures

that there is sufficient material to absorb most hadrons that reach the HCAL, allowing mainly muons to be recorded by the muon chambers.

Hadron Calorimeter Barrel

The hadron barrel (HB) detector [29] consists of 9 layers of limited streamer tube chambers with anode wires 1cm apart. The outer surface of each chamber comprise 8 pads and the charge induced on these pads is summed to give an estimate of the local hadronic shower energy. Aluminium strips centred above the anode wires run the entire length of the inside of chamber, parallel to the beam direction, and are read out to provide extra tracking information. The chambers alternate with 8 iron slabs and span radii from 3.39m to 4.39m. The iron slabs are 100mm thick with 25mm gaps and provide 4 or more interaction lengths of absorber. The barrel ends are then closed off by the endcap regions. This portion of the HCAL covers the region for which $|\cos\theta| < 0.81$.

Hadron Calorimeter Endcap

The hadron endcap (HE) detector is similar to HB but has one fewer layer, consisting of 8 layers of chambers sandwiched around 7 slabs of iron. The principle of operation is exactly the same. The endcaps extend the coverage to the region $0.81 < |\cos\theta| < 0.91$.

Hadron Poletip

The hadron poletip (HP) detector extends the acceptance of hadron calorimetry further, down to $|\cos\theta| = 0.99$. The number of samples in this region is increased to 10 and the detectors are 0.7cm thick multiwire proportional chambers, strung with anode wires at a spacing of 0.2 cm. Like HB and HE, the chambers have pads on one side and strips on the other.

2.2.6 Muon Detectors

The muon detectors are the final layer of the detector because muons are very penetrating particles and undergo little attenuation by any of the other subdetectors or the iron magnet yoke. The acceptance of the muon chambers extends over approximately 93% of the solid angle and the detection efficiency for sufficiently high momentum muons is close to 100% inside this acceptance.

There are two arrangements of detectors–the muon barrel and muon endcaps.

Muon Barrel

The muon barrel (MB) detector [30] contains 110 drift chambers, each 1.2m wide and 90mm thick, arranged in four layers. Most of these chambers are 10.4m long. Some are shorter to avoid interference with the magnet support structures. Each chamber is split into two adjoining cells each containing an anode signal wire running the full length of the cell, parallel to the beamline. The arrangement of wires within these cells allows charge-drifting of up to 30cm, with the drift time providing the $r-\phi$ measurement to an accuracy of 1.5mm. An array of diamond-shaped cathode pads directly opposite the anodes allows a z coordinate to be calculated by using the difference in time and pulse height of the signals arriving at both ends of the anode wire. A better z coordinate measurement is achieved by using induced signals on two sets of cathode pads whose diamond shape repeats every 17.1 cm and 171 cm respectively. This gives a z-coordinate resolution of around 1.5mm. The acceptance for MB covers the region for which $|\cos\theta| < 0.72$.

Muon Endcaps

The muon endcap (ME) detectors [31], one at each end of the OPAL detector, consist of four quadrant chambers which are approximately 6m square and 2 patch chambers that are 3m by 2.5m. This arrangement of quadrants and patches was designed to give the maximum coverage around the beam pipe after allowing for cabling for inner detectors and the

magnet supports. Each detector is made from two crossed double-layers of streamer-tubes, 0.9cm by 0.9cm in cross section. The gas flowing through the chambers is a composition of 25% argon and 75% isobutane. The isobutane is used as a quenching agent to limit the charge avalanche in the streamer tube. The pairs of planes are situated aproximately 5.5m from the vertex and separated in z by 67cm, providing two measurements of x and y across a significant lever arm. Each of the layers of streamer tubes has two planes of readout strips, which are aligned both parallel and perpendicular to each tube. The spatial resolution achieved is around 3mm for the parallel wires and 1mm for the perpendicular wires. ME extends the coverage of the muon detectors down to $|\cos\theta| = 0.985$.

2.2.7 Luminosity Measurement At OPAL

For many analyses, knowledge of the experimental luminosity is required. Equation 2.1 expresses how often we should expect to see a particular event process $ab \longrightarrow xy$ with a cross-section $\sigma_{ab\rightarrow xy}$:

$$\mathcal{L} = \mathrm{N_{ab\rightarrow xy}}/\sigma_{\mathrm{ab\rightarrow xy}} \tag{2.1}$$

where $N_{ab\rightarrow xy}$ is the number of observed events.

$\mathcal{L}$ is known as the *integrated luminosity* because it takes the intensities of both particle beams and the total experimental running time into consideration. Bhabha scattering has a very high cross-section $\sigma_{\mathrm{e^+e^-\rightarrow e^+e^-}}$ which is proportional to $1/\theta^3$ where θ is the measured scattering angle. The luminosity can be calculated from Equation 2.1 by recording the number of Bhabha events ($N_{\mathrm{e^+e^-\rightarrow e^+e^-}}$) in the known acceptance of the forward region of the detector.

The Forward Detector and SiW Luminosity Monitor

Two subdetectors are used to derive the experimental luminosity– the forward detector (FD) [32] and the silicon-tungsten luminosity monitor (SW) [33]. The acceptance for these

detectors is from 26 to 200 mrad and this is ideal for detecting Bhabha events. The forward detector consists of a combination of two electromagnetic calorimeters (of lead-scintillator sandwich design utilising 40 lead plates and layers of scintillating plastic material) and radial drift chambers for determining the position of showers. The detectors are located in two symmetric positions, ±2.6m from the interaction point. In 1993, a silicon tungsten luminosity monitor was added to improve the resolution of luminosity measurement at OPAL. Each of the silicon tungsten calorimeters is constructed from 19 layers of silicon detectors and 18 interleaved plates of tungsten. They are situated ≈ ±2.4m from the interaction region.

2.3 OPAL Online Software

The raw information obtained by each subdetector consists of track charges, pulse heights and magnitudes of signals from calorimeter clusters. This section describes the methods employed to reduce the quantity of raw data, which enables faster data-processing, and how these raw data are combined to reconstruct the event.

2.3.1 The OPAL Trigger

During the LEP I data-taking period the bunchlet configuration of the two colliding beams was optimised to ensure that high currents could be accumulated in each bunchlet while minimising beam-beam effects. This also permitted as high a luminosity as possible to be attained. In 4×4 mode, four bunch trains of four bunchlets each (labelled A, B, C and D) were employed.

At LEP II the electrons and positrons are accelerated in a 4×1 configuration having four bunches, each containing a single bunchlet of electrons/positrons in position A. The beam crossing rate of around 45kHz produces a possible collision every 22μs. Full read-out of an event takes much longer than the time between successive bunch crossings. To maintain a high overall detector efficiency and minimise detector dead time, and hence

a loss of possible interesting physics, a "triggering" system is employed. The trigger [34] reduces the data rate by using information from each subdetector. This allows checking of each event and discrimination against unwanted processes. These include cosmic ray backgrounds, interactions between beam and gas or the wall of the beampipe and electronic noise in the detector.

Most subdetectors supply signals to the central trigger. There are two types of trigger signals. Firstly, there are *stand-alone* triggers: examples of these are track multiplicities and calorimeter energy sums. The second type of trigger is derived from correlations between subdetectors in the *theta-phi matrix*. The solid angle covered by the OPAL detector is divided into overlapping volumes and the boundaries of these volumes are fixed in θ and ϕ: there are 6 divisions in θ and 24 in ϕ. Each subdetector provides information for the trigger matrix elements and these are processed alongside the stand-alone signals to decide whether an e^+e^- collision has occurred.

LEP is capable of running in 8×8 mode, with 8 bunches of electrons and positrons colliding. This increases the available luminosity but doubles the bunch crossing rate to 90kHz. A pre-trigger system was introduced during 1993 to improve the central trigger under these conditions, using similar techniques. By employing a coarser $\theta - \phi$ matrix, with 12 volumes, and stand-alone pre-trigger signals, a more rapid response could be achieved. The pre-trigger was retained when LEP ceased using 8×8 mode though most signals have become redundant.

If the event is selected by the trigger, each of the subdetectors is read out by the data acquisition system. If not, a reset signal is sent in time for the next bunch crossing.

2.3.2 The OPAL Data Acquisition System

The OPAL subdetectors each have one or more local system crates (LSC) into which the data are individually read out by the front-end electronics. Within the LSC, the data are reformatted and reduced in size before being sent via a network link to a high-speed

workstation– the event builder – where each sub-event is combined to produce a single set of data that describes the entire event. The event builder synchronises the readout of every subdetector. Having been assigned a trigger number, the data are sent from the event builder to a second workstation for preliminary classification into a physics category (multihadron, $\ell^+\ell^-$-pair, etc.). This filter machine helps to reduce the quantity of semi-processed data that is recorded on tape by rejecting additional non-physics events that were selected by the trigger. The physics data are then compressed and stored on disk and tape media.

2.3.3 Event Reconstruction Using ROPE

After data acquisition, the raw data must be converted into a set of real physical quantities on an event-by-event basis. This is achieved within an OPAL software package called ROPE (Reconstruction of OPal Events) [35]. The input to ROPE can be either raw data or simulated data (see the following section) and both are treated in the same way. Using a database of calibration constants (OPCAL [36]), ROPE determines momenta, energy deposits in clusters, charges of certain tracks and the identity of particles. The data are then available for analysis.

2.3.4 OPAL Detector Simulation

Simulated data can be obtained by using a Monte Carlo program which generates specified physical processes (for instance μ or τ pair production) or hadrons from a certain decay channel. Examples of such generators are KORALZ [37], which simulates the decay of the Z° to leptons, JETSET [38] for multihadronic decays and KORALW [39], a generator for W^+W^- decay channels. A package called GOPAL (GEANT at OPAL) [40] is used to model the detector and incorporates details such as detector geometry, detector response and materials used in the construction. Generated particles are used as input to GOPAL and the resulting hits data are processed by ROPE as if they were real data. The "tree level"

information, *i.e.* the actual particle identity or momentum, is also available so that checks of the efficiency or purity of an event selection can be made.

Chapter 3

A Theoretical Overview of the Process $e^+e^- \rightarrow \mu^+\mu^-(\gamma)$

The mechanism by which fermions couple to the Z° boson is of great importance in testing the validity of the standard electroweak theory and in searching for new physics.

Final state neutrinos are undetectable and so it is not possible to study the decays $Z^\circ \rightarrow \nu_e\overline{\nu}_e$, $Z^\circ \rightarrow \nu_\mu\overline{\nu}_\mu$ or $Z^\circ \rightarrow \nu_\tau\overline{\nu}_\tau$ directly. Electrons can be identified very easily but $Z^\circ \rightarrow e^+e^-$ is a reaction that can proceed by either s-channel decay of a Z°/γ after e^+e^- annihilation, or by the t-channel scattering of the initial e^- and e^+ by the exchange of a photon or Z°: to study the s-channel vertex using final-state e^+e^- would require a correction for the effects of the t-channel process. However, $Z^\circ \rightarrow \mu^+\mu^-$ only proceeds via s-channel process and offers a particularly clean and well defined final state for electroweak studies.

The work in this thesis concerns the production of muon pairs at collision energies below $m(Z^\circ)$ and at high energy ($\sqrt{s}$ = 189 and 192 GeV). In this chapter, the theory describing muon pair production from e^+e^- collisions is summarised.

3.1 The Differential Cross-section

The differential cross-section is an energy dependent expression for the Z° cross-section and angular distribution of decay products. This expression, excluding any corrections for radiation of photons (*i.e.* at tree level), is shown in Equation 3.1.

$$\begin{aligned}\frac{d\sigma_0}{d\cos\theta} = \frac{\pi\alpha^2}{2s}\beta_e\big\{&(1+\beta_f^2\cos^2\theta)[Q_f^2 + c_1\mathrm{Re}(\chi) + c_2|\chi|^2] \\ &+ \beta_f\cos\theta[d_1\mathrm{Re}(\chi) + d_2|\chi|^2] \\ &+ (1-\beta_f^2)\sin^2\theta[Q_f^2 + c_1\mathrm{Re}(\chi) + c_3|\chi|^2]\big\}\end{aligned} \tag{3.1}$$

where α is the fine structure constant, s is the square of the centre-of-mass energy, β_e and β_f are the speeds of the incoming electron and the outgoing fermion in the Z° centre-of-mass frame, expressed as a fraction of the speed of light, Q_f is the charge of the final state fermion (-1 for muons in this case) and θ is the angle between the incoming electron and the outgoing fermion (or between the positron and outgoing antifermion). $\mathrm{Re}(\chi)$ is the real part of χ, the Breit-Wigner resonance form, described by

$$\chi = \frac{s}{(s - m(\mathrm{Z}^\circ)^2) + \mathrm{i}m(\mathrm{Z}^\circ)\Gamma(\mathrm{Z}^\circ)} \tag{3.2}$$

where $m(\mathrm{Z}^\circ)$ is the mass of the Z° and $\Gamma(\mathrm{Z}^\circ)$ is its total width. The constants c_1, c_2, c_3, d_1 and d_2 are functions of the vector and axial-vector couplings of the Z° boson to electrons and muons.

For lowest order s-channel production of a $\mu^+\mu^-$ pair, there are two contributing Feynman diagrams. The first involves possible annihilation to a photon, the second production of a Z° boson (Figure 3.1). These two processes contribute to the total amplitude which is squared to obtain the cross-section expression. Therefore, there are three contributions to the total cross-section, arising from pure γ exchange, pure Z° exchange and $\gamma - \mathrm{Z}^\circ$

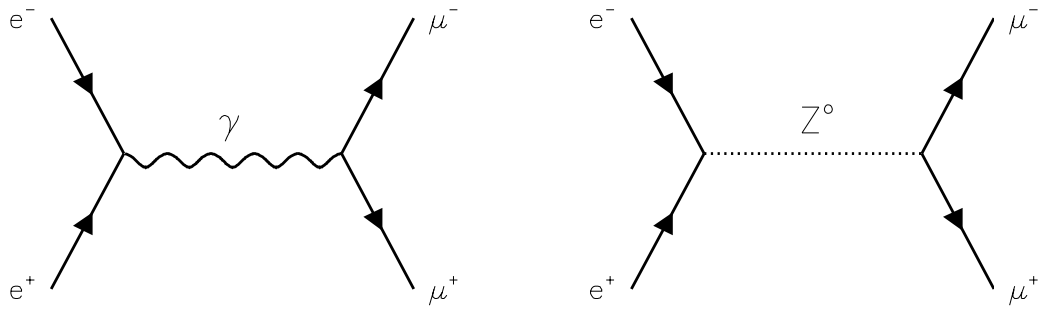

Figure 3.1: Feynman diagrams for the process $e^+e^- \rightarrow \mu^+\mu^-$ involving exchange of a virtual photon or a Z° boson.

interference:

$$\sigma_0 = \sigma_0^{\gamma} + \sigma_0^{Z^\circ} + \sigma_0^{\gamma/Z^\circ} \tag{3.3}$$

There are $1 + \cos^2\theta$, $\cos\theta$ and $\sin^2\theta$ terms in the differential cross-section expression although the latter is very small as $\beta_f \approx 1$. Each term is multiplied by a factor which is a function of χ and the coupling constants. The Breit-Wigner resonance function is complex, and is dependent on s. This energy dependence of the resonance peak leads to different contributions of each of the three terms that are functions of θ. At $\sqrt{s} = m(Z^\circ)$, $s - m(Z^\circ)^2$ is zero and so χ becomes purely imaginary. At this energy, the $1 + \cos^2\theta$ term is predominant with a small $\cos\theta$ dependence because the Z° boson couplings to left and right handed particles are not the same. The small forward-backward asymmetry resulting from the $\cos\theta$ term is also a manifestation of $\gamma - Z^\circ$ interference, from which the contributions to the total cross-section increase at energies away from the Z° mass. Away from the Z° pole, there is a $1/s$ dependence of the cross-section from the photon contribution. The cross-section variation with $\sqrt{s}$ is illustrated in Figure 3.2.

The forward-backward asymmetry is usually expressed as

$$A_{FB} = \frac{\sigma_F - \sigma_B}{\sigma_F + \sigma_B} \tag{3.4}$$

with the cross-sections for the forward ($\cos\theta > 0$) and backward ($\cos\theta < 0$) hemispheres

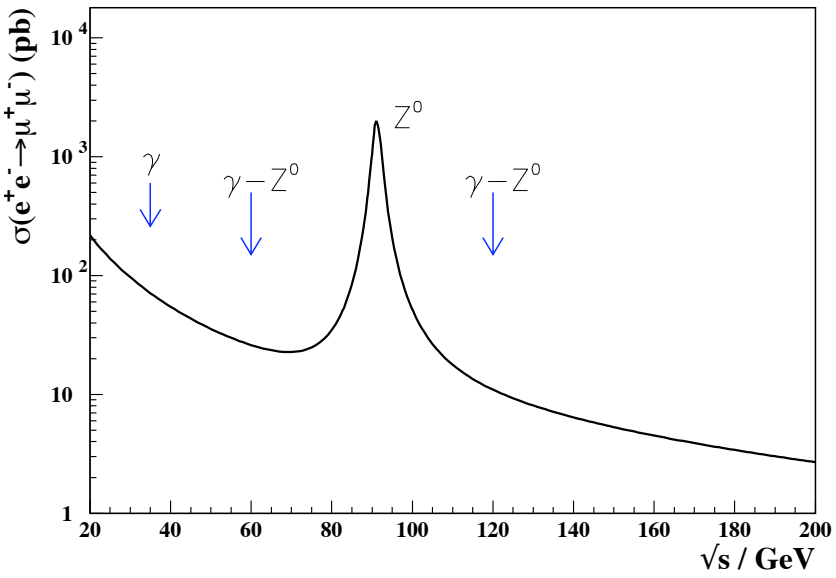

Figure 3.2: The Z° lineshape, illustrating the regions in $\sqrt{s}$ where γ exchange, γ−Z° interference and Z° exchange occur.

obtained by integration with respect to $\cos\theta$

$$\sigma_F = \int_0^{+1} \frac{d\sigma}{d\cos\theta} d\cos\theta \qquad \sigma_B = \int_{-1}^{0} \frac{d\sigma}{d\cos\theta} d\cos\theta \tag{3.5}$$

where the respective hemispheres are denoted by the F or B subscripts. This method is referred to as the counting method, and usually the cross-sections are expressed as the numbers of events populating each hemisphere of the $\cos\theta$ distribution:

$$A_{FB} = (N_F - N_B)/(N_F + N_B) \tag{3.6}$$

with an associated statistical error given by

$$\Delta A_{FB} = \sqrt{(1 - A_{FB}^2)/(N_F + N_B)} \tag{3.7}$$

where N_F and N_B are the number of events in the forward and backward hemispheres respectively. Simplification of Equation 3.1, for β_e=β_f=1, leads to

$$\frac{d\sigma}{d\Omega} = \frac{\alpha^2}{4s}\Big[A_0(1+\cos^2\theta) + A_1\cos\theta\Big] \tag{3.8}$$

where dΩ is an element of solid angle. The coupling constants have now been included in the terms A_0 and A_1. The standard model lowest-order lepton asymmetry, $A_{FB}^{0,l}$ is obtained by integration of Equation 3.8 and yields

$$A_{FB}^{0,l} = \frac{3}{8}\frac{A_1}{A_0} \tag{3.9}$$

3.2 Electroweak Corrections

Near the Z° resonance peak, the effects of radiative processes must be included in any calculation to enable the Z° width or other parameters to be extracted. For predictions to be made from the theoretical models, corrections must also be included for reactions at $\sqrt{s}$ above m(Z°). The electroweak corrections change the shape of the resonance peak. They can be divided into two types–

- QED (photonic) corrections, which involve one or more additional photon lines in the Born level Feynman diagrams. These photons can be emitted from the initial or final state, and can be real or virtual photons. Figure 3.3 shows some of the contributing Feynman diagrams for the virtual corrections to electron-muon scattering. There will also be a set of corrections where there are real photons emitted from any of the fermion lines in the diagrams.

- Weak radiative corrections, where virtual loops are introduced in propagator terms or the vertex factors. Examples include diagrams containing quark-antiquark loops (Figure 3.4) or loops that include virtual Higgs or electroweak bosons.

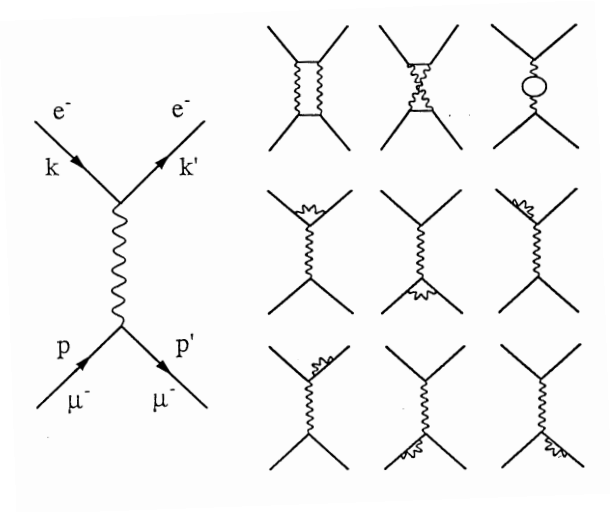

Figure 3.3: Feynman diagrams showing some of the virtual radiative (photonic) corrections to electron-muon scattering. A set of real corrections includes the above diagrams where there is real photon emission from any of the fermion lines. The initial fermion momenta are denoted by p and k; the momenta of the scattered fermions are denoted by $p^{'}$ and $k^{'}$.

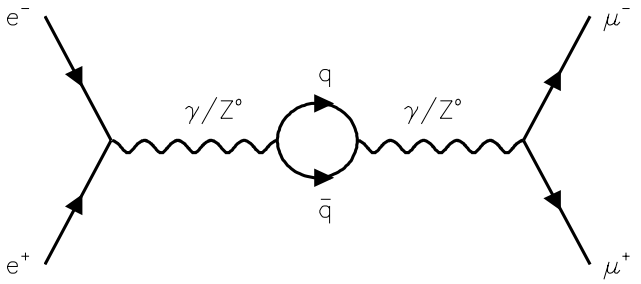

Figure 3.4: Feynman diagram showing virtual $q\bar{q}$ loops in weak radiative corrections to $e^+e^- \rightarrow \mu^+\mu^-$, where q can be any flavour of quark.

The photonic corrections can be divided into three categories, arising from initial-state radiation (ISR), final-state radiation and initial-final state interference. The magnitudes of the effects of these three types of process are significantly dependent on the experimental setup and applied cuts. The reason for this is that emission of photons changes the measured polar and azimuthal angles of the tracks of the produced muon pairs. The largest correction is due to ISR, because radiation of photons before the e^+e^- collision lowers the available centre-of-mass energy of the reaction. For reactions at high energies, $\sqrt{s} \gg m(Z^\circ)$, there is a large enhancement of the cross-section after initial state radiation.

The typical photonic corrections to Born level result in a reduction of the peak height by about 30%, a shift in the peak towards high energy of around 100 MeV and a hard radiative tail. A semi-analytical program called ZFITTER [41] can be used to calculate standard model parameters at Born level, and convolute these lowest-order processes with radiator functions to include higher order QED effects. The standard model prediction for the $e^+e^- \to \mu^+\mu^-$ cross-section before and after application of all corrections is shown in Figure 3.5(a). The forward-backward asymmetry for $e^+e^- \to \mu^+\mu^-$ changes sign at $\sqrt{s} = m(Z^\circ)$ and is greatly affected by QED corrections which cause a shift in the zero position and a global change of shape. The standard model prediction for A_{FB} is shown in Figure 3.5(b). In the region of s near to $m(Z^\circ)$, the magnitudes of the corrections can vary appreciably and the photonic corrections dominate: there is at least an order of magnitude effect when QED corrections are included, relative to the Born-level prediction with weak corrections only.

To achieve a precision measurement of Z° parameters at the 1% level, final state corrections must also be included though these are numerically smaller than those of ISR. The overlap of initial and final state photon wavefunctions introduces interference which also contributes to the set of photonic corrections. Although initial and final state corrections are dependent only upon s, the interference is dependent on the scattering angle of the fermions too. This implies that the size of the interference correction will depend on the applied cuts. The interference correction includes the interference between Feynman

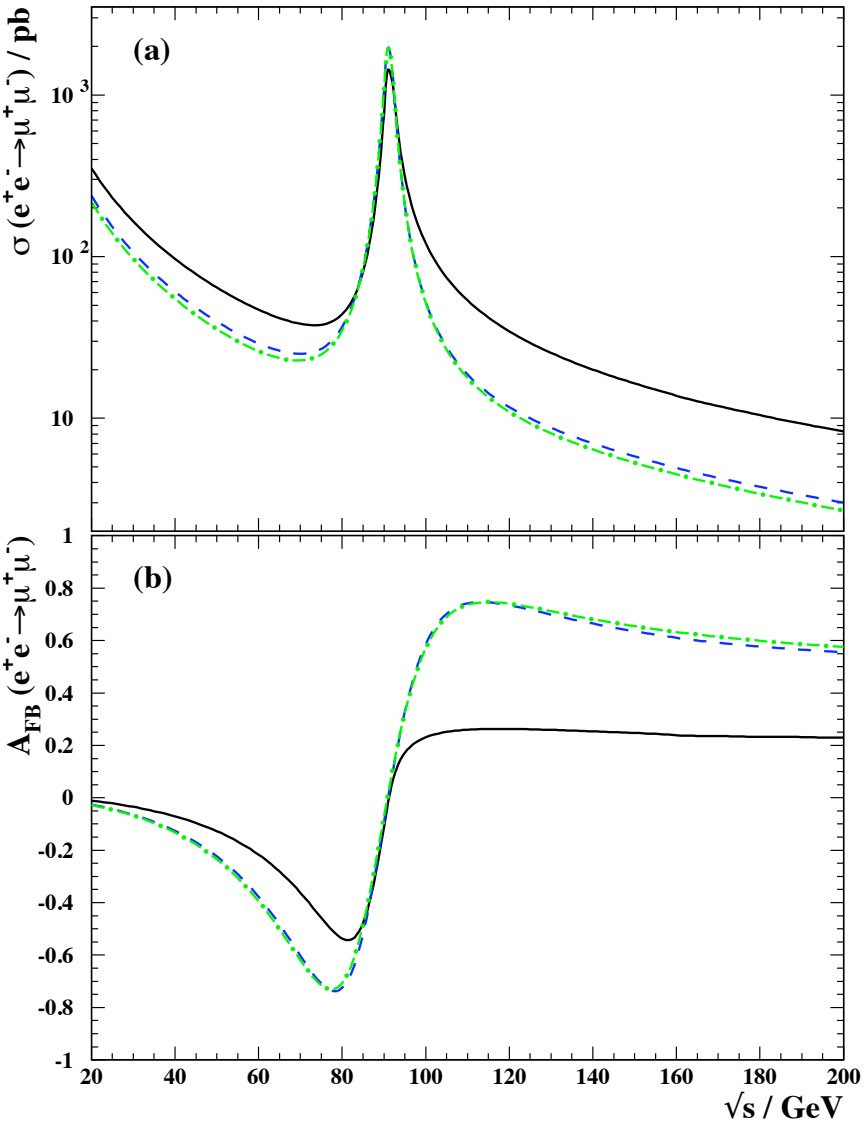

Figure 3.5: The standard model prediction for: (a) the cross-section and (b) the forward-backward asymmetry, for $e^+e^- \to \mu^+\mu^-$ as a function of $\sqrt{s}$. The solid line shows the cross-section with all radiative corrections included. The dashed line includes only weak radiative corrections and the dotted line is the Born level prediction.

diagrams with real photons, tree-level amplitudes and boxes. The dominant angular-dependent terms are of a form that leads to numerically small inteference corrections for loose angular cuts. At $\sqrt{s} = m(\mathrm{Z}^\circ)$, the initial-final state interference is of order 10^{-3}. For experimental setups or cuts that are more restrictive, the interference correction can become more significant.

The weak corrections commonly consist of extra loops or boxes of virtual particles which are purely internal and are not detected. For this reason, the magnitude of the effects of weak radiative corrections are not dependent on the experimental setup or any applied cuts, but are sensitive to the masses of the loop particles.

The theoretical background to the production of muon pairs via s-channel annihilation of a photon or a Z° has been introduced in this chapter. By making measurements of some of the important parameters, the theory can be tested. This can be achieved by comparison of the measured values with those expected from calculational tools. Such comparisons allow scope for looking for evidence of new physics.

In the following two chapters, measurements of cross-sections and asymmetries in muon pair production are made. In Chapter 4, the region of $\sqrt{s}$ below the Z° production threshold is explored while in Chapter 5, data recorded at energies as high as 192 GeV are used.

Chapter 4

A Study of Radiative Muon Pair Events at $\sqrt{s} < m(\mathrm{Z}^\circ)$

In 1989, the Large Electron Positron collider (LEP) at CERN was completed and collisions between electrons and positrons were seen for the first time at a centre-of-mass energy ($\sqrt{s}$) centred on the mass of the Z° gauge boson. Real Z° bosons produced at rest can subsequently decay to $\mu^+\mu^-$. Although a large proportion of e^+e^- collisions occur at full energy (*i.e.* on-peak), it is possible that either (or both) incoming lepton beams may undergo initial state radiation (ISR) before collision which lowers the centre-of-mass energy to an effective value, $\sqrt{s'}$. Muon pairs produced after such collisions can be used to make measurements of forward-backward asymmetries and cross-sections at energies below $\sqrt{s}$. This is especially useful since the energy region between LEP and the Japanese collider TRISTAN, which ran at a $\sqrt{s}$ of 58 GeV, has not been explored directly: no other colliders have run in this energy range.

During the period 1993 to 1995, the OPAL experiment recorded 121.4 pb^{-1} of data including some taken at energies ± 2 GeV "off-peak". This chapter describes the method employed to select radiative events from this dataset, and make electroweak measurements. The first sections describe the techniques and cuts used to initially pre-select

muon pair candidates from raw Opal data, and then classify them as muon pairs through application of tighter selection cuts and event vetos. The later sections describe additional event selection cuts used to isolate radiative events. Finally, results are presented and compared to those of the other Lep experiments.

4.1 Trigger Requirements for Muon Pairs

During the early stages of Lep I data-taking, many studies of trigger efficiency were performed and the trigger system optimised. No further studies have been made for this analysis but a brief description of the important trigger details relevant for muon pairs is given here.

In order to select muons, there are four subdetectors that provide inputs to the trigger logic– the central detector track trigger (TT), the time-of-flight counters (TO), the electromagnetic calorimeter (EM) and the muon chambers (MU). The track trigger is a programmable hardware processor that takes its input from the vertex and jet chambers. For the barrel region of the Opal detector, the trigger fires if there are coincidences in the theta-phi matrix from two or more of these four detectors. If there are collinear track triggers, an additional separate collinear trigger fires. The availability of more than one trigger ensures good redundancy in the triggering of muon pair events. This is especially important for events with tracks that lie in geometric regions where there are holes in the acceptance for a subdetector. These holes are necessary to allow access for cabling and structural supports and consequently the acceptance is degraded in the overlap between the barrel and endcap muon chambers. Because the muon signature is very clear, there are typically several trigger signals that will ensure that the event is recorded. The high level of redundancy implies a high trigger efficiency, typically around 99.9% [42], for muon pair events used in this analysis.

4.2 Data Selection

There are three stages involved in obtaining muon pair events – preselection from raw data, event veto and classification as muon pair candidates. A complete description of each of these stages can be found in [43]. A summary of the important points is presented below.

4.2.1 Preselection of $Z^\circ \rightarrow \mu^+\mu^-$ Decays

The general preselection is designed for high efficiency tagging of most Z° decay channels. The preselection is a set of basic requirements that are quite loose and specific decays are selected by imposing tighter cuts at the classification stage. For lepton pair preselection, a standard set of routines is available within the OPAL reconstruction software.

An event is preselected if it satisfies any of the following conditions:-

1. TRACK PROPERTIES. At least one track with

   - transverse momentum $p_t > 0.7$ GeV that satisfies $|d_0| < 1$cm and $|z_0| < 50$cm where d_0 is the distance from the vertex to the point of closest approach in the $r-\phi$ plane and z_0 is the z-coordinate when the track is at the point of closest approach in the $r-\phi$ plane.
   - a minimum of 20 hits in the central detector (vertex chamber, jet chamber and z-chambers combined).

   These criteria ensure that tracks are good (*i.e.* well reconstructed) and originate close to the interaction region. A track that meets the quality requirements above is called a "high p_t" track.

2. MUON ENDCAPS. A track in the muon endcap detector which is not more than 20cm from the collision point when extrapolated back to the $z = 0$ plane. There must be less than four muon tracks in total in the endcap.

3. ELECTROMAGNETIC CALORIMETERS. At least two calorimeter clusters, each having total corrected transverse energy $E_t > 6$ GeV and measured to be collinear to within 25°.

The effectiveness of the first requirement above is shown in Figure 4.1(a) for raw data recorded at $\sqrt{s} = 91$ GeV. The first selection ensures that many different types of event are kept, while the second and third selections provide a means by which muons with endcap hits, or electrons and taus with calorimeter energy deposits, may be selected independently of the central tracking subdetectors.

The very loose preselection will include multihadronic or cosmic ray events and further, tighter, preselection cuts are required to veto these types of event.

4.2.2 Multihadronic Event Veto

Z° decays to multihadrons typically have many tracks in the detector. Electromagnetic clusters are usually associated with these tracks. Therefore most multihadronic events can be rejected by ensuring that the sum of the numbers of tracks, N_{tracks}, and number of clusters, $N_{clusters}$, satisfies

$$N_{tracks} + N_{clusters} > 18 \tag{4.1}$$

A track is counted if $p_t > 0.1$ GeV, $|d_0| < 1$cm and $|z_0| < 20$cm. Electromagnetic calorimeter clusters in the barrel are counted if there is a raw energy deposit of more than 0.1 GeV while in the endcap calorimeter, the energy deposit must be more than 0.2 GeV in two blocks with less than 99% of the total energy of the cluster in the highest energy block. Figure 4.1(b) shows the distribution of the sum of tracks and clusters for raw data.

This is a fairly loose cut but removes a large number of multihadrons while minimising the loss of $e^+e^- \rightarrow \tau^+\tau^-$ events which decay hadronically in the detector. Emission of final state photons can result in the appearance of two extra tracks arising from pair-production (photon conversion to e^+ and e^-). There may also be track reconstruction

deficiencies leading to split tracks when charged particles pass close to the cathode wires of the jet chamber. These types of event are also retained by such a loose veto requirement.

4.2.3 Cosmic Ray Veto

As cosmic rays passing through the detector can generate hits in the subdetectors, a pre-selection requirement may be satisfied. Such events can therefore be mistaken for $e^+e^- \rightarrow \mu^+\mu^-$ events. These may be rejected using timing information provided by time-of-flight counters or by using measurements of track parameters at the vertex. For an event to be classified as a muon pair candidate, the following criteria must be met according to the geometric region of the detector in which the tracks are reconstructed. Events are removed if they are not in time with the beam crossing, distinguishing between cosmic ray events crossing the detector and pairs of particles produced simultaneously at the vertex.

Distributions of the time-of-flight and vertex cut quantities are discussed in more detail in the next chapter and are shown in Figure 5.1 and Figure 5.2 respectively, for data recorded at $\sqrt{s} = 189$ GeV.

Events in the barrel region

For events to be classed as barrel events, both tracks must have $|\cos\theta| < 0.8$ and satisfy timing criteria using information from the barrel time-of-flight counters. If a cosmic ray travels through the detector from above, it would be expected that hits in the lower counters record a later time than the upper counters. For pairs of muons produced at the interaction point, hits in these counters would both occur at similar times. A quantity, Δt, is defined as the difference between the time determined by the lower counter and that determined by the upper counter. For good muon events, Δt should be in the range $|\Delta t| <$ 10ns. For these events, t_0, the smallest absolute time recorded by either TOF counter, must also be no more than 10ns from that expected for a $\beta = 1$ particle originating at

the vertex, when corrected for flight-time. Any events having $|\Delta t| > 10$ns or $|t_0| > 10$ns are rejected. If a barrel event has only a single TOF counter hit then only the absolute time cut must be satisfied.

For events in the barrel that have no TOF hits, the matching of the tracks to the nominal interaction point is checked using a tight vertex association cut. These events must pass a tight vertex requirement based on the sums of the d_0 and z_0 of each track, satisfying $\Sigma|d_0| < 0.08$cm and $\Sigma z_0 < 10$cm.

Events in the endcap region

Because there is no available time-of-flight information for events in the endcap region for data recorded during LEP I, cosmic ray rejection is achieved by using vertex cuts only. Because the position resolution in the endcaps is somewhat poorer than in the barrel, a looser vertex cut with $\Sigma|d_0| < 0.6$cm and $\Sigma z_0 < 50$cm is required.

4.2.4 Muon Pair Classification

In order to select a sample of muon pair events from the preselected data, event candidates must pass tighter selection cuts which are part of the identification and classification stage. Identifying muon tracks involves looking for activity in the muon chambers or the hadron calorimeter, or looking at track momentum and energy deposits in the electromagnetic calorimeter.

A "high p_t track" is identified as a muon if any of the following requirements are met:-

- there are at least two muon chamber hits (muon barrel and muon endcap combined) associated with the track.
- there are at least four hadron calorimeter strips with hits, with an average number of hits of less than two per layer. For $|\cos\theta| < 0.65$ there must be at least one hit in the last three layers of strips.

- track momentum p > 15 GeV and the sum of the energy deposits in the electromagnetic calorimeter associated to the track is less than 3 GeV.

To further suppress the likelihood of including multihadronic events, a tighter track multiplicity cut is imposed. Any event with more than three tracks that pass the "high p_t track" requirement in Section 4.2.1 is rejected.

To be classified as a muon pair, the event must contain at least two tracks identified as muons in the region $|\cos\theta| < 0.95$, separated in azimuth by at least 320mrad. If there are more than one pair of suitable tracks then the pair of tracks having highest momentum sum is selected. In addition, to assist with the rejection of background events from tau pairs, the visible energy must exceed $0.6\sqrt{s}$. The visible energy, E_{vis}, is defined as the sum of the two muon momenta plus the highest energy electromagnetic calorimeter cluster in the event. The distribution of this quantity for raw data is shown in Figure 4.1(c).

4.2.5 Data Quality and Luminosity

Each OPAL subdetector has a status flag which indicates the operating condition of the trigger and detector for a particular period of data-taking. This flag is set to 0 if the status of the subdetector is unknown, 1 if the detector was not functioning at all, 2 if there were minor problems (but data still usable) or 3 to indicate good data quality. As some analyses are more dependent on some subdetectors than others, the use of the detector/trigger operating status flagging allows data to be used, even if a subdetector had a problem during a run. The minimum detector and trigger status requirements for the analyses of muon pairs presented in this thesis is shown in Table 4.1.

The forward detector (FD) and silicon tungsten luminosity monitor (SW) are used to detect the small-angle Bhabha scattering events for determination of the luminosity. Both of these detectors have an operating status and the integrated luminosity is obtained for the three possible combinations of this status: both $SW = 3$ and $FD = 3$, $SW = 3$ and $FD \neq 3$ or $SW \neq 3$ and $FD = 3$. If both subdetectors have a status less than 3 then the

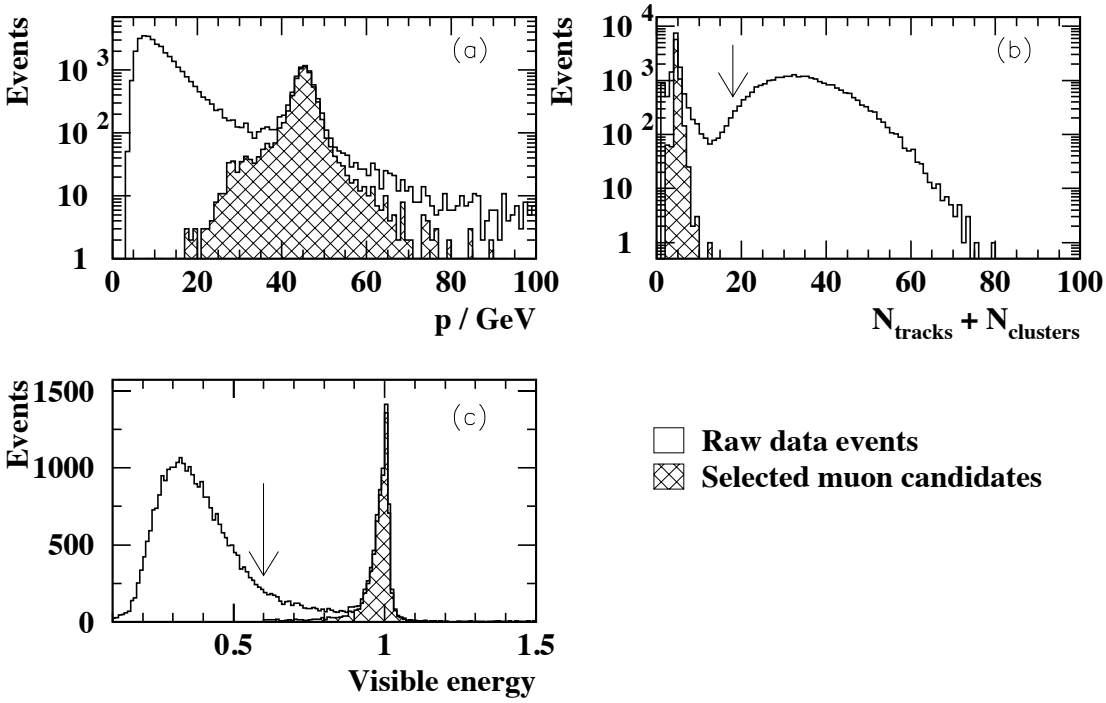

Figure 4.1: Distributions of important quantities used for selecting muon pair candidates from raw data recorded at $\sqrt{s} = 91$ GeV. The open histograms show (a) the momentum (p) distribution, (b) the sum of the number of tracks and clusters in each event and (c), the total visible energy for the preselected data, while the hatched histograms show the same distributions after the muon selection cuts are applied. The arrows show the positions of these selection cuts.

Status type	CV	CJ	TB	EB	EE	ME
Detector	2	2	2	2	2	0
Trigger	0	2	2	0	0	2

Table 4.1: The minimum detector and trigger status requirements for the muon pair analyses presented in this thesis.

data is rejected as unusable. The total luminosity is the sum of that determined using the silicon tungsten luminosity monitor (when status = 3 and data quality is good) and that determined by the forward detector (when detector status of SW is less than 3).

During 1993-1995, a large number of Z° decays were recorded by each of the LEP collaborations. Because data recorded at several "scan" points, above and below $\sqrt{s} = m(Z^\circ)$, is included, the measurement of the integrated luminosity is divided into three regions according to $\sqrt{s}$. The details of the centre-of-mass energy regions chosen and the total luminosity available for each of these arbitrary regions is shown in Table 4.2. The division of the available data in this way ensures a correct approach to the normalisation of Monte Carlo samples to the data luminosity. The errors on the luminosities shown include

	$\int \mathcal{L}\, dt$ pb^{-1}		
Year	$\sqrt{s} < 91$ GeV	$91 < \sqrt{s} < 92$ GeV	$\sqrt{s} > 92$ GeV
1993	8.84±0.48	14.02±0.02	9.35±0.34
1994	–	55.64±3.11	–
1995	8.48±0.02	15.88±0.05	9.16±0.02
Total	17.32±0.48	85.54±3.11	18.51±0.34

Table 4.2: The integrated luminosity of the data, per region of $\sqrt{s}$. The totals are shown, with corresponding total errors obtained by adding the statistical and systematic errors in quadrature.

statistical and systematic uncertainties in the number of $e^+e^- \to e^+e^-$ events counted, theoretical uncertainties, including those from Monte Carlo simulations, and errors on the beam energy.

4.3 Monte Carlo Samples

Events from physics processes other than $e^+e^- \to \mu^+\mu^-$ that are selected because they satisfy the selection requirements and have tracks that are identified as muons are called background events. At energies near to $\sqrt{s} = m(Z^\circ)$, typical background processes can include other 2-fermion decays of the Z° (for example $e^+e^- \to e^+e^-$, $e^+e^- \to \tau^+\tau^-$

and $e^+e^- \to q\overline{q}$), 2-γ or four-fermion processes. The latter type of decay could include the process $e^+e^- \to e^+e^-\mu^+\mu^-$ where the e^+ and e^- in the final state travel down the beampipe leaving two muon tracks in the detector. For muon pair analyses, a dominant background is $e^+e^- \to \tau^+\tau^-$ and includes events where the taus decay to a pair of muons that are detected.

Background processes were modelled using Monte Carlo techniques. Four-vectors were generated using standard generators [37, 44], and all events were passed through a simulation of the OPAL detector and processed in the same way as real data. Signal events for the process $e^+e^- \to \mu^+\mu^-$ were also generated with high statistics and used to obtain the efficiency of the selection cuts. The details of the Monte Carlo samples used are shown in Table 4.3. Any quantities to be compared to real data were normalised to the total data luminosity according to the $\sqrt{s}$ of the generated events.

4.3.1 Experimental Characteristics of Photon Radiation

Many e^+e^- collisions occur at full energy, where there is no hard photon emission from the initial state particles. The final state particles produced in these events usually proceed outwards from the interaction point and through the detector with little final-state radiation. In this situation, the two muons are produced back-to-back in the laboratory frame (Figure 4.2). If a photon is emitted in the initial state from either the e^- or e^+, then the resulting μ-pairs are boosted and are no longer back-to-back in θ. The boost is only a function of the photon energy and occurs along the z-axis for photon emission collinear with the beam. If the photon travels away from the z-axis, then its momentum vector should be taken as the axis for the boost. In this analysis, all initial state photons are assumed to have zero transverse momentum relative to the beam axis. Thus, the spatial effect of ISR is restricted to two dimensions (the $r - z$ plane). The degree to which an event deviates from a back-to-back topology in the $r - z$ plane is called *acollinearity* and distributions of this quantity are shown in Figure 4.3 for on-peak data events with $\sqrt{s} =$

Final state	$\sqrt{s}_{nominal}$ (GeV)	Generator	$\int \mathcal{L}\ \mathrm{d}t\ \mathrm{pb}^{-1}$
$\mu^+\mu^-$	89	KORALZ	202.4
$\mu^+\mu^-$	89	KORALZ	141.7
$\mu^+\mu^-$	91	KORALZ	134.9
$\mu^+\mu^-$	91	KORALZ	404.3
$\mu^+\mu^-$	91	KORALZ	252.9
$\mu^+\mu^-$	93	KORALZ	143.1
$\mu^+\mu^-$	93	KORALZ	143.1
$\tau^+\tau^-$	89	KORALZ	200.8
$\tau^+\tau^-$	89	KORALZ	141.9
$\tau^+\tau^-$	91	KORALZ	202.6
$\tau^+\tau^-$	91	KORALZ	405.1
$\tau^+\tau^-$	91	KORALZ	253.0
$\mathrm{e^+e^-}\mu^+\mu^-$	91	VERMASEREN	433.0
$\mathrm{e^+e^-}\mu^+\mu^-$	91	VERMASEREN	456.1
$\mathrm{q\overline{q}}$	91	PYTHIA	1000.0
$\tau^+\tau^-$	93	KORALZ	147.7
$\tau^+\tau^-$	93	KORALZ	142.5

Table 4.3: The Monte Carlo samples used to simulate data for the efficiency determination, and for estimating background contributions.

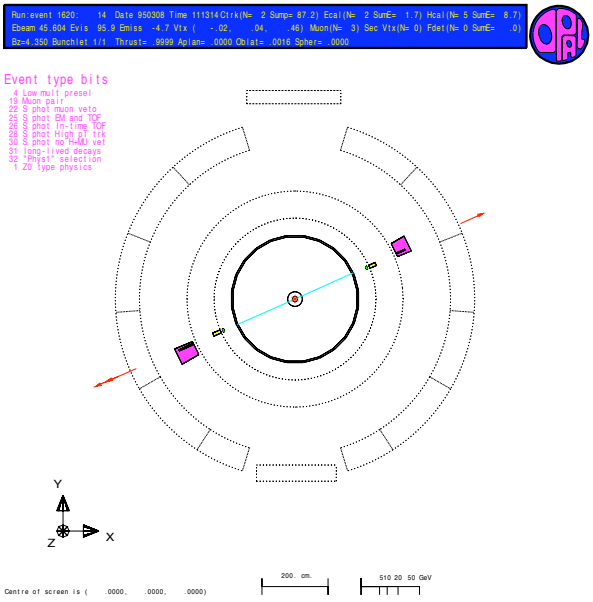

Figure 4.2: A typical dimuon event without initial or final state radiation.

91 GeV. The acollinearity is small for events that do not emit energetic ISR photons but there is a tail containing events where hard photons are emitted.

In the case of final state radiation, where the photon can be radiated in any direction, the sum of the muon momenta can have a component which is non-zero in the $r-\phi$ plane. These events are identified by their acoplanarity[(a)], ζ– the higher the energy of FSR photons, the larger the acoplanarity of the muons. Acoplanarity distributions are shown in Figure 4.4(a) for events recorded at $\sqrt{s} = 91$ GeV. An example of an event with final state radiation seen at OPAL is shown in Figure 4.5 and Figure 4.6.

[(a)]The acoplanarity ζ is defined as $180° - \phi$ where ϕ is the angle between the two muons in the $r-\phi$ plane.

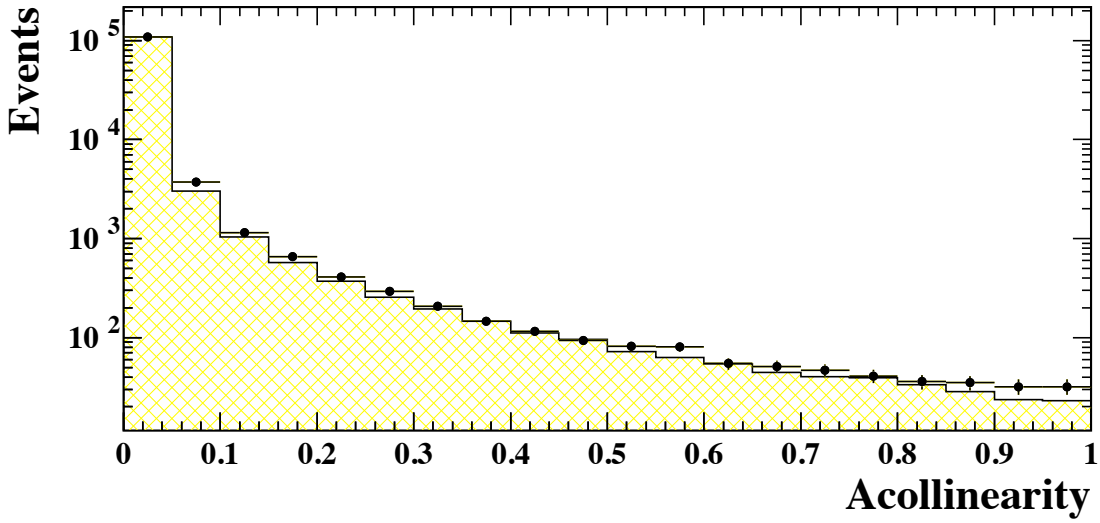

Figure 4.3: Acollinearity distribution for events recorded at $\sqrt{s} = 91$ GeV. The histogram is the signal Monte Carlo and the points represent the data.

4.3.2 Determining the Effective Collision Energy, $\sqrt{s'}$

The effective collision energy $\sqrt{s'}$ can be determined in several different ways. Methods include kinematic fits and techniques that also use a detected initial state photon. The method presented here is the simplest approach and utilises the polar angles, θ_1 and θ_2, of each muon track with respect to the incoming electron to estimate the effective $\sqrt{s'}$ for an event. The angles are determined using the central tracking information if the track is in the barrel region, or using the muon endcap detector if the track is in the endcap region. This method has also been employed for a series of analyses of lepton-pairs at high energy [45, 46]. The assumption is made that any initial state radiation is emitted collinear with the source particle, e^- or e^+ (*i.e.* in the $\pm z$ direction), and is not recorded by the detector. The energy of such a photon can be estimated using massless three-body

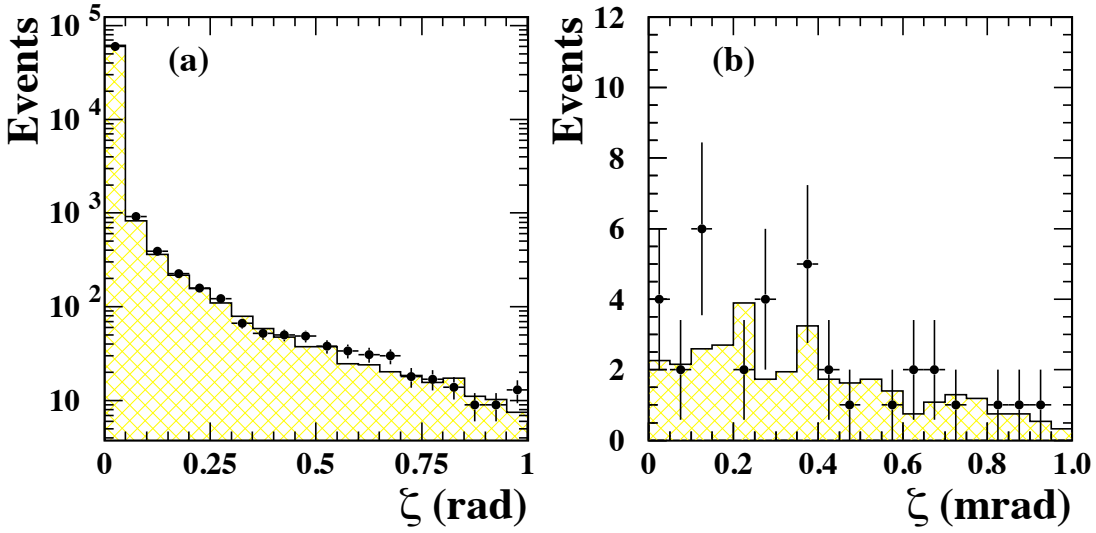

Figure 4.4: Acoplanarity distributions for (a) all events recorded at $\sqrt{s} = 91$ GeV and, (b) selected events in the 80–85 GeV $\sqrt{s'}$ region. The histogram is the signal Monte Carlo and the points represent the data.

kinematics as:

$$E_\gamma = \sqrt{s}\frac{|\sin(\theta_1+\theta_2)|}{|\sin(\theta_1+\theta_2)| + \sin\theta_1 + \sin\theta_2} \tag{4.2}$$

The effective centre-of-mass energy is then given by

$$\sqrt{s'} = \sqrt{s - 2E_\gamma\sqrt{s}}. \tag{4.3}$$

The generated value of the $\sqrt{s'}$ of each event, $\sqrt{s'}_{true}$, is known from Monte Carlo. The correlation between the reconstructed $\sqrt{s'}$, $\sqrt{s'}_{rec}$, and $\sqrt{s'}_{true}$ can be checked as a test of the effectiveness of this technique. Figure 4.7 shows this comparison for events at $\sqrt{s} =$ 91 GeV. For many events there is good agreement between reconstructed and true values, with events clustered along the line where $\sqrt{s'}_{rec} \approx \sqrt{s'}_{true}$. Deviation from this line is a

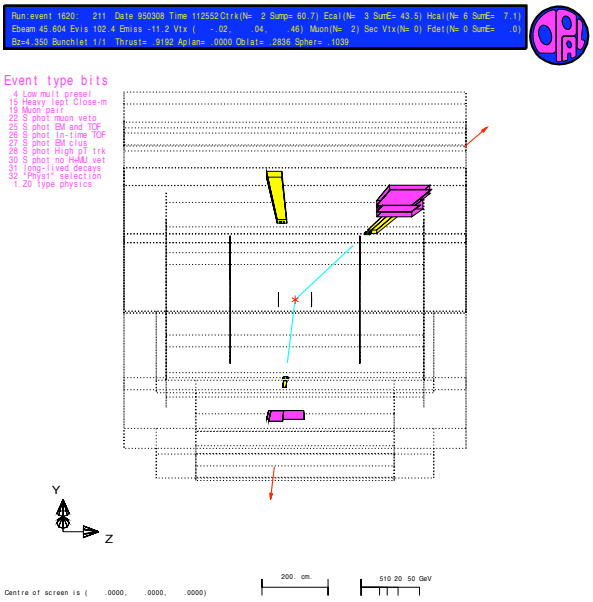

Figure 4.5: A $\mu^+\mu^-$ event with hard final state radiation; $r-z$ Plane.

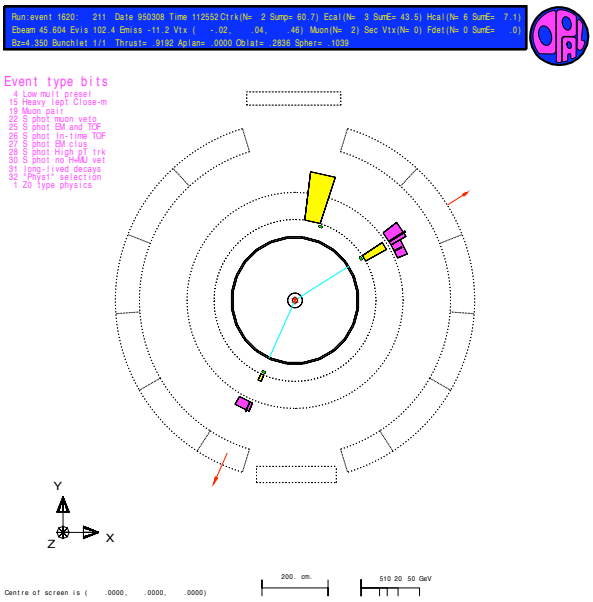

Figure 4.6: A $\mu^+\mu^-$ event with hard final state radiation; $r-\phi$ Plane.

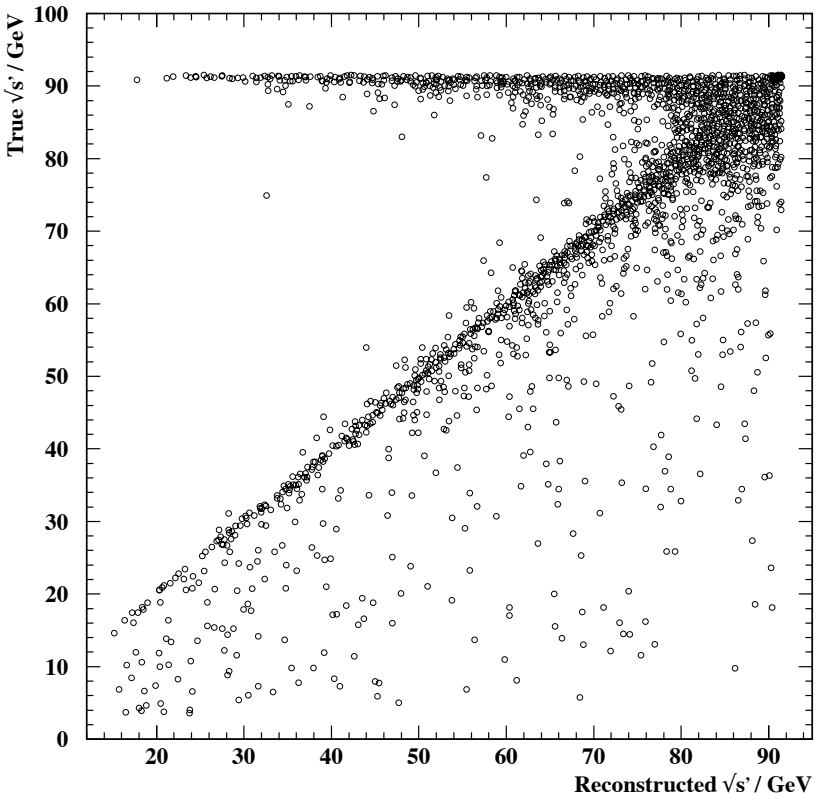

Figure 4.7: $\sqrt{s'}_{true}$ versus $\sqrt{s'}_{rec}$ for the 91 GeV $e^+e^- \rightarrow \mu^+\mu^-$ Monte Carlo.

result of several different effects. These include the presence of final-state radiation, initial state photons with with $p_t \neq 0$ and resolution effects. In some events, the reconstructed $\sqrt{s'}$ is too high as a consequence of there being more than one initial state photon emitted. The assumptions do not hold in this case, which can occur when, for example, both the e^- and e^+ beams radiate a photon prior to collision.

Feedthrough

Events that are reconstructed in an energy region other than that at which they were generated are known as *feedthrough events*. These events have a $\sqrt{s'}_{true}$ value that is above or below that for the region of interest and contaminate the sample of selected

events. Final-state radiative events can have a $\sqrt{s'}_{rec}$ higher or lower than the true value because the reconstructed $\sqrt{s'}$ is a function of θ_i and FSR photon emission alters the measured θ_i for track i ($i = 1, 2$). These events contribute significantly to the feedthrough. The horizontal band at the top of Figure 4.7 illustrates events where FSR has occurred, producing a $\sqrt{s'}_{rec}$ that is too low. To obtain as pure an event sample as possible in the desired energy region, excluding as many final state radiative events is paramount. For each of the $\sqrt{s'}$ regions, the proportion of true events selected in the region and the feedthrough contributions were studied using Monte Carlo. All of the Monte Carlo signal samples generated at $\sqrt{s} = 91$ GeV were used for this purpose, totalling 10^6 events. Table 4.4 lists the numbers of preselected events in the $\sqrt{s'}$ regions, the true events (with $\sqrt{s'}_{rec}$ and $\sqrt{s'}_{true}$ in the same energy region) and the feedthrough events. All numbers are expressed as fractions of the total event sample. The feedthrough contamination is severe

Selection category	Fraction of events in $\sqrt{s'}$ region (%)			
	50–60 GeV	60–70 GeV	70–80 GeV	80–85 GeV
Selected by $\sqrt{s'}_{rec}$ cut	0.09	0.21	0.58	0.90
Selected with $\sqrt{s'}_{rec}$=$\sqrt{s'}_{true}$	0.02	0.03	0.06	0.12
Total feedthro'	0.07	0.18	0.52	0.78
Feedthro' from above $\sqrt{s'}_{rec}$ cut	0.07	0.17	0.51	0.76

Table 4.4: The numbers of events selected from signal Monte Carlo at $\sqrt{s} = 91$ GeV in each of the four $\sqrt{s'}$ regions, expressed as a fraction of the total number of events. A total of 10^6 events were used.

in all regions, with approximately 84% of events selected in the 80–85 GeV region coming from feedthrough. This proportion falls to 78% for the lowest region. The feedthrough from below each region of interest is less than 0.2% for all regions studied. These numbers illustrate the difficulty in the selection of signal events and indicate the need for further selection cuts to reduce the effects of FSR.

4.4 Analysis of $e^+e^- \to \mu^+\mu^-(\gamma)$ Data Events

Other LEP experiments have chosen several ranges of $\sqrt{s'}$ for their analyses, extending to the low energy region. The work presented here is a study of events with $\sqrt{s'}$ in the range 50 GeV to 85 GeV, divided into regions chosen to offer some overlap with both TRISTAN results and those from LEP while maintaining high enough statistics to enable measurements to be made. Four energy regions were chosen– 50–60 GeV, 60–70 GeV, 70–80 GeV and 80–85 GeV.

There are two possible approaches to radiative event selection. Using calorimeter information, one could select for study only events with hard ISR photons that also satisfy any $\sqrt{s'}$ requirements. This is called an *exclusive* analysis. Alternatively, one could just select events on the basis of their $\sqrt{s'}$ (*inclusive* analysis). The latter approach has been used here. Therefore, events were selected at each energy by demanding that

$$\sqrt{s'}_{\text{UPPER}} < \sqrt{s'} < \sqrt{s'}_{\text{LOWER}}$$

where $\sqrt{s'}_{\text{UPPER}}$ and $\sqrt{s'}_{\text{LOWER}}$ are the upper and lower bounds of the region of interest respectively. In addition, the following two criteria had to be satisfied:

- CV stereo hits $\geqslant 1$ for both muon tracks.
  This is necessary to ensure good overall track quality for θ determination.

- Acoplanarity, $\zeta \leqslant$ 1mrad.
  This requirement removes most final-state radiative events. The cut was relaxed to 17mrad for some systematic studies.

The distribution of $\sqrt{s'}/\sqrt{s}$ is shown in Figure 4.8 for all data used in this analysis, before selection cuts. There is good agreement between data and Monte Carlo. The arrow shows the region from which events in the four $\sqrt{s'}$ regions were selected. The analysis was performed individually for the datasets at each of the three originating centre-of-mass energies. The average $\sqrt{s'}$ for the selected raw data events in each $\sqrt{s'}$ region,

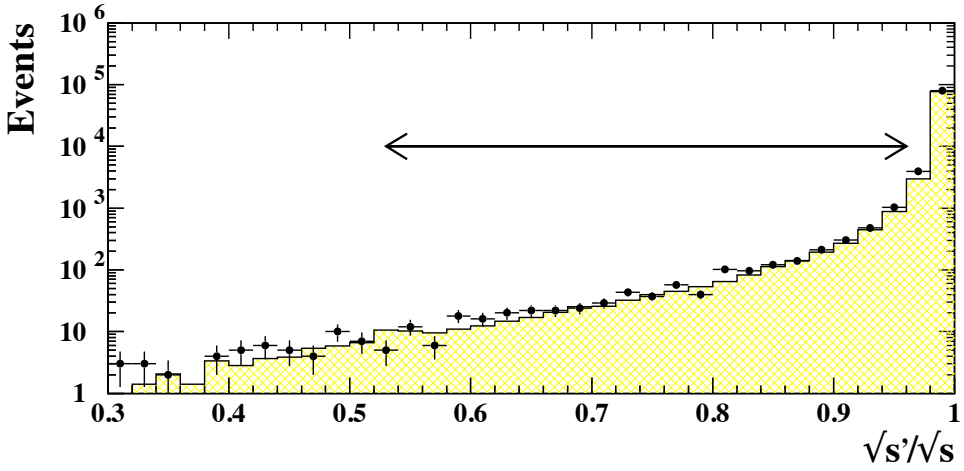

Figure 4.8: The distribution of $\sqrt{s'}/\sqrt{s}$ for all data, before application of selection cuts.

$<\sqrt{s'}>$, was found and used as input to ZFITTER for calculating theoretical predictions for both the asymmetry and cross-section. An overall theoretical prediction for the three collision energies was obtained by finding a luminosity-weighted average. All numbers of selected data and Monte Carlo events were summed to give the total number of raw data, background, feedthrough and signal Monte Carlo events in each $\sqrt{s'}$ region.

4.4.1 Efficiency, Background and Feedthrough

The events selected by cuts applied to data are raw events and include contamination from both feedthrough and non-physics background. The size of this contamination was estimated using the Monte Carlo samples. To determine the background contributions, the selection cuts were applied to the Monte Carlo samples for each background process. A preliminary analysis included studies of approximately 10^6 $e^+e^- \to e^+e^-$ events, none of which were selected as signal. Since it was not possible to increase the number of events available, the $e^+e^- \to e^+e^-$ background was assumed to be negligible. Background processes account for <0.1% of events selected in the two lowest $\sqrt{s'}$ regions; this propor-

tion rises to 0.9% and 0.3% for the 70–80 GeV and 80–85 GeV regions respectively. The majority of these background events come from $e^+e^- \to \tau^+\tau^-$ and $e^+e^- \to e^+e^-\mu^+\mu^-$ processes. The feedthrough contribution to the selected event sample was determined by studying simulated events selected in the reconstructed $\sqrt{s'}$ region: since the Monte Carlo event headers contain the true $\sqrt{s'}$ information, the proportion of selected events having true $\sqrt{s'}$ outside the given range can be found. After final selection cuts, the feedthrough was found to be between 11% for the lowest $\sqrt{s'}$ region to 19% for the highest. The corrected numbers of data events for each energy region were then obtained from

$$N_{corrected} = \frac{N_{raw} - N_{background} - N_{feedthrough}}{\mathsf{E}} \tag{4.4}$$

where N_{raw}, $N_{background}$ and $N_{feedthrough}$ are the number of raw data events, the number of background events and the number of feedthrough events for the $\sqrt{s'}$ region of interest. The efficiency, E, is defined as

$$\mathsf{E} = \frac{N(after\ all\ cuts)}{N(generated\ events)} \tag{4.5}$$

where both the numerator and the denominator are numbers of events where the true $\sqrt{s'}$ is in the same energy region as the measurement.

The numbers of events selected in data and simulated data, normalised to the data luminosity, are shown in Table 4.5. For the asymmetry measurements, angular distributions of the selected feedthrough and background events were obtained and used to correct the angular distributions of raw data using the above expressions. The purpose of the efficiency correction is to compensate for the geometric acceptance of the detector: for this reason, and because of the very low statistics available in the selected regions, an efficiency correction was calculated without imposing any $\sqrt{s'}$ selection, *i.e.* using only events with $\sqrt{s'} \approx \sqrt{s}$. Mainly due to the very harsh cut on acoplanarity, the efficiencies per bin in $\cos\theta$ were low and varied from 40% at the edges of the detector acceptance rising to >60% within the barrel region.

4.4.2 Measurements of the $e^+e^- \to \mu^+\mu^-(\gamma)$ Cross-Section

Establishing a peak cross-section, where only full-energy events are used, is straightforward given the number of events that have been selected and the integrated luminosity for the available data. For the case where measurements are made using radiative events to probe the regions below the collision energy, however, a cross-section cannot be obtained directly because the integrated luminosity is a function of the collision energy $\sqrt{s}$ whereas the measurements involving radiative events are at an effective collision energy $\sqrt{s'}$. Two methods can be used to measure the cross-section for $e^+e^- \to \mu^+\mu^-(\gamma)$.

1. Data to Monte Carlo event ratio

   Use ZFITTER to calculate the standard model prediction for the cross-section at the energy of interest and multiply this by a factor which is the ratio of the numbers of raw events selected in data to the number of raw events selected in Monte Carlo:

   $$\sigma(\sqrt{s'}) = \frac{N_{events}^{data}}{N_{events}^{MC} + N_{events}^{BG}} \times \sigma(\sqrt{s'})^{SM} \tag{4.6}$$

   where N_{events}^{data} and N_{events}^{MC} are the number of events selected in the data and Monte Carlo respectively, N_{events}^{BG} is the number of background events and $\sigma(\sqrt{s'})^{SM}$ is the predicted standard model cross-section.

2. Radiator function, $\boldsymbol{\rho}$

   Take full account of the photon emission by convoluting the raw cross-section with a probability distribution called a *radiator function*. This function expresses the likelihood of an e^+e^- collision occurring at the energy of interest, *i.e.* after ISR.

The radiator function [47] introduces photonic corrections due to initial state radiation and has the following functional form

$$\rho(s', s) = K_1(1 - s'/s)^{K_2} - K_3(1 + s'/s) \tag{4.7}$$

where K_i are constants. As initial state radiation can occur from either the incoming electron or the positron (or both), the radiator function describes the convolution of both of the beam energy distributions, per collision. The shape of this function is illustrated in Figure 4.9. When initial state radiation occurs, a fraction of the energy in the centre-of-mass system is carried away by the photon. The radiator function $\rho(s'/s)$ expresses the probability that the energy in the centre-of-mass, $\sqrt{s}$, will be reduced to $\sqrt{s'}$ by ISR or, put more simply, it says how often an e^+e^- collision will take place at a certain energy. Measurements made in the analysis yield the number of events for a given $\sqrt{s'}$

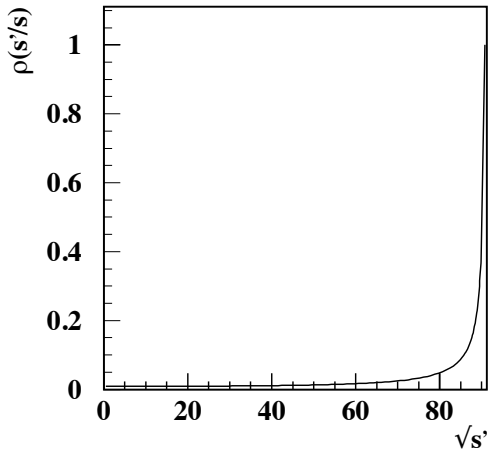

Figure 4.9: The radiator function $\rho(s', s)$ as a function of $\sqrt{s'}$.

range, $N_{events}^{s'_1-s'_2}$, after correction for background, feedthrough and efficiency. The expression relating the number of observed events to $\sigma^{\mu^+\mu^-}(s')$, the radiative cross-section for $e^+e^- \to \mu^+\mu^-(\gamma)$, is obtained using

$$N_{events}^{s'_1-s'_2} = \mathcal{L} f(s') \int_{s'_1}^{s'_2} \rho(s', s)\sigma^{\mu^+\mu^-}(s')ds' \tag{4.8}$$

where $\mathcal{L}$ is the measured integrated luminosity at the peak centre-of-mass energy $\sqrt{s}$. An additional correction factor, $f(s')$, must be introduced to account for effects associated with the $\sqrt{s'}$ reconstruction where events migrate to outside the limits of the selected

region. These corrections amount to between 1.33 for the highest $\sqrt{s'}$ region, to 2.0 for the lowest. The integral over the radiator function in Equation 4.8 reduces to a single number for each energy of interest. A simple calculation then yields the cross-section for muon pairs $\sigma^{\mu^+\mu^-}$ produced in the energy range $\sqrt{s'}_1$ to $\sqrt{s'}_2$.

To use the radiator function method, a cutoff to account for soft ISR photon emission must be introduced, otherwise the radiator function becomes undefined. Studies showed that the results using this method were dependent on the cutoff chosen, and it was difficult to motivate an appropriate choice of cutoff. The radiator function was therefore not considered further. Instead, all cross-sections were calculated using Equation 4.6. The results of the measurements are tabulated in Table 4.5 and illustrated in Figure 4.10. The standard model prediction was calculated using ZFITTER, including electroweak vertex and propagator corrections but excluding all QED radiative effects. The systematic error

$\sqrt{s'}$ GeV	$<\sqrt{s'}>$ GeV	N^{obs}_{events}	N^{MC}_{events}	$\sigma(pb)$	$\sigma^{SM}(pb)$
50–60	56.39	2.0	6.8	$9.4^{+8.7}_{-5.3}\pm0.2$	32.0
60–70	63.53	13.0	11.1	$31.4^{+9.6}_{-7.9}\pm1.2$	26.8
70–80	76.21	39.0	32.3	$33.9\pm5.4\pm0.1$	28.1
80–85	83.10	95.0	87.9	$60.4\pm6.2\pm2.6$	55.9

Table 4.5: The measured values of the cross-section for the inclusive analysis of radiative $e^+e^- \to \mu^+\mu^-$ events, $\sigma(e^+e^- \to \mu^+\mu^-(\gamma))$. The first error is statistical and the second is systematic. The raw numbers of data and Monte Carlo events from which the measurement is obtained are also shown.

on the cross-section measurement was derived by considering individual contributions to this error and combining them in quadrature. The sources studied included errors on the background estimation, the resolution of the $\sqrt{s'}$ reconstruction and the effect of differences in average $\sqrt{s'}$ of the data events and Monte Carlo events on the standard model predictions obtained. The latter contribution is the most significant, accounting for more than 80% of the total systematic error in each region.

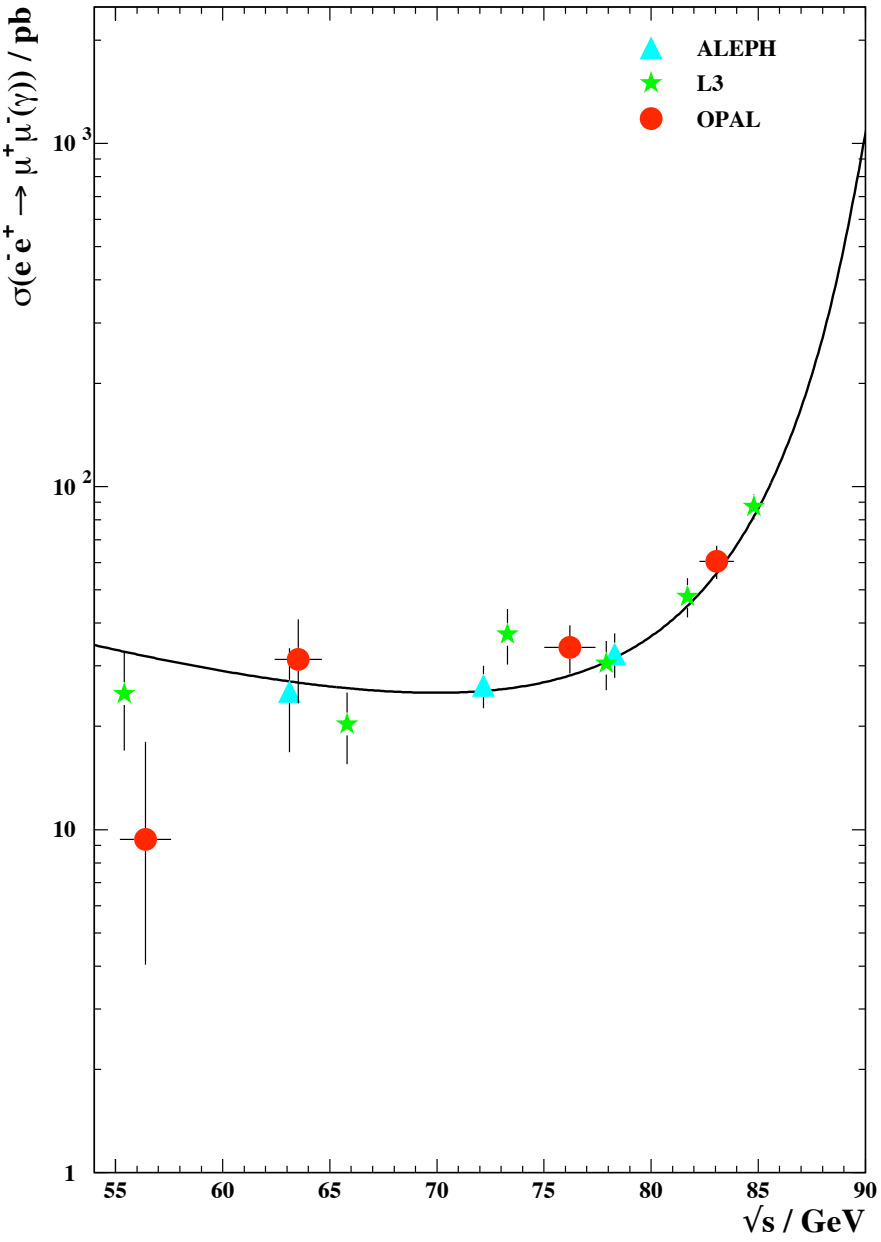

Figure 4.10: The results of cross-section measurements for $e^+e^- \to \mu^+\mu^-(\gamma)$, $\sigma(e^+e^- \to \mu^+\mu^-(\gamma))$. The standard model prediction from ZFITTER is shown as the solid line.

The systematic error on the cross-section from background was calculated by increasing the total background contribution by 50%, recalculating the cross-section and finding the difference between the new cross-section and the measured value. An initial check of the reliability of the $\sqrt{s'}$ reconstruction was made directly by using the Monte Carlo generator information and plotting the difference between the reconstructed and true $\sqrt{s'}$ for each energy region. (Figure 4.11). The spread of the distribution is an approximate

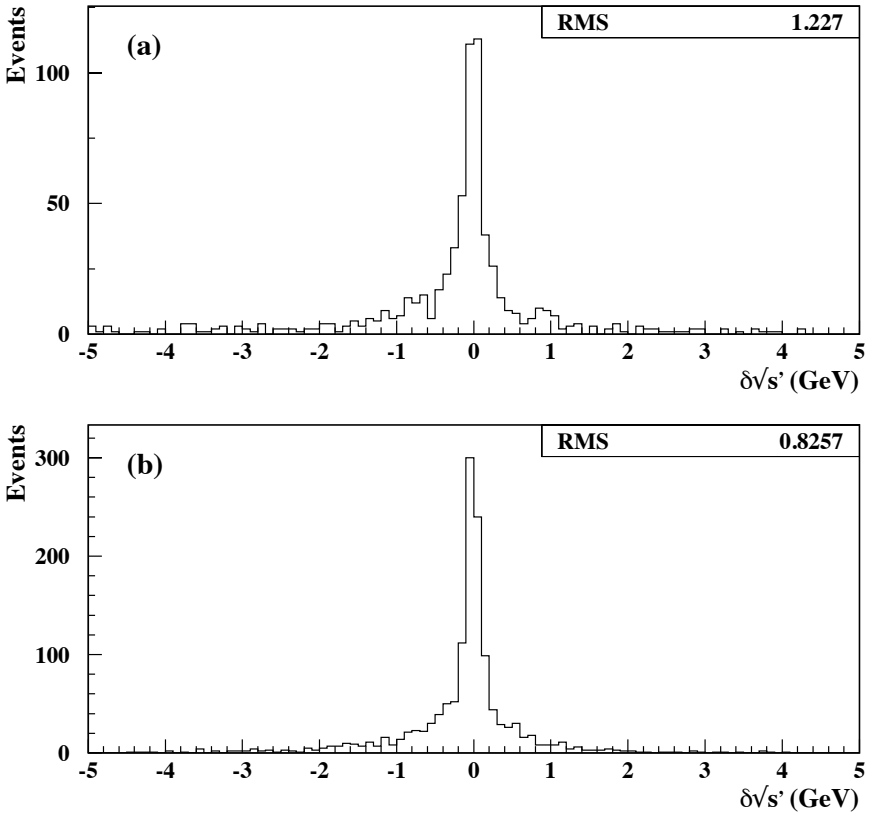

Figure 4.11: The resolution of the $\sqrt{s'}$ reconstruction technique, $\delta\sqrt{s'}$, estimated using Monte Carlo for the (a) 70–80 GeV and (b) 80–85 GeV $\sqrt{s'}$ regions.

measure of the resolution. The RMS values range from 1.3 GeV in the lowest energy region to 0.8 GeV for the 80–85 GeV region. This method does not account, however,

for any discrepancies in the agreement between Monte Carlo and data and so systematic effects arising from the $\sqrt{s'}$ reconstruction were estimated by studying the resolution of the measured θ in both data and Monte Carlo separately using back-to-back tracks. The resolution $\delta\theta$ is defined as θ_1-θ_2 on an event-by-event basis. Distributions of this quantity are shown in Figure 4.12 for Monte Carlo and data events. Barrel events have both tracks reconstructed within the barrel volume; endcap events are events that have one track reconstructed in each endcap. A quality factor, Q, defined as the ratio of the RMS of

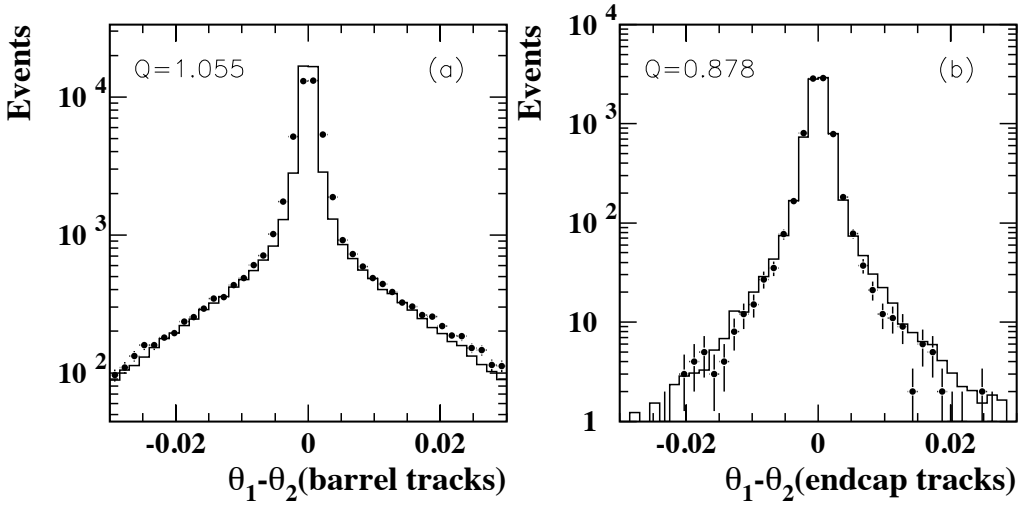

Figure 4.12: The distributions of θ_1-θ_2 for data and Monte Carlo events, before selection cuts, and having both tracks occupying (a) the barrel region and (b) the endcap region. The quantity Q is defined as $\mathrm{RMS}_{data}/\mathrm{RMS}_{Monte\ Carlo}$.

the data to the RMS of the Monte Carlo, was obtained from the resolution plots. For tracks situated in the endcaps, the difference in the RMS between data and Monte Carlo is primarily due to the poorer agreement at large $\delta\theta$, with the data points below the Monte Carlo in the tails of the distribution. For the barrel tracks, however, the modelling at

small $\delta\theta$ is not good and so the overall Q is dominated by the effect of this difference, despite the fact that the agreement at large $\delta\theta$ is good. Given this information, and using a sample of Monte Carlo signal events, a simple smearing technique was used to vary the Monte Carlo reconstructed $\sqrt{s'}$ by a small amount. This was achieved using

$$\sqrt{s'}_{rec}^{smeared} = \sqrt{s'}_{true} + (\sqrt{s'}_{rec} - \sqrt{s'}_{true}) \times Q \tag{4.9}$$

where $\sqrt{s'}_{rec}^{smeared}$, $\sqrt{s'}_{true}$ and $\sqrt{s'}_{rec}$ are the smeared $\sqrt{s'}$, generated $\sqrt{s'}$ and reconstructed $\sqrt{s'}$ respectively. The event selection was applied to the sample of events having smeared $\sqrt{s'}$ and the difference in the numbers of events selected before and after smearing was taken as an estimate of the systematic error from θ resolution effects. Combining the effects of the smearing in endcap and barrel regions showed a fractional change in the number of selected events of around 1.0%, relative to the number of events selected without smearing. This is very small relative to the statistical errors at all energy regions considered and therefore no additional systematic error contribution is included for the θ resolution.

The final contribution considered was from the calculation of the standard model prediction. This was determined by using the $<\sqrt{s'}>$ for Monte Carlo events in the energy region as input to ZFITTER instead of $<\sqrt{s'}>$ for data events, and studying the effect on the measured cross-section. The discrepancy observed was taken as the systematic error.

4.4.3 Asymmetry Measurements and Angular Distributions

Forward-backward asymmetry measurements were obtained from distributions of the charge-signed $\cos\theta$, the product of the track charge and the cosine of the angle of the track measured in the detector, $q_i \cos\theta$, for selected muon events. Only one track was chosen to form this quantity. The choice of track is arbitrary, since the definition of the charge-signed $\cos\theta$ ensures that the track appears in the correct hemisphere of the dis-

tribution. In this analysis, the track was chosen randomly.[b] The counting method, as described in Section 3.1, was used to obtain the asymmetry. Because of the effect of initial state radiation on muon $\cos\theta$ distributions through Lorentz boosting, measurements involving polar angles were made in the rest frame of the μ-pair. Using the estimated initial state photon energy (Equation 4.2), the polar angles measured in the detector were transformed to their rest-frame value, θ^*, which is the angle between the μ^- and the e^- beam in the centre-of-mass frame. Both the charge determination and the θ for each track must be of high quality for precise asymmetry measurements. A reliable measurement of the z coordinate was obtained by demanding that, for barrel events, there were hits in the z-chambers. This gives a good endpoint for the tracks and permits determination of θ using the central detector. For events which have tracks outside the barrel acceptance, the quality of the z position is not as reliable because in this case the jet chamber and vertex chamber information is used. At least three vertex chamber hits were required to exclude any events of this type that might have suffered reconstruction problems. The actual θ measurement for tracks without hits in the z-chambers was determined using the muon endcap detector, since the extrapolation of hits in the endcaps to the interaction point results in a large lever-arm for θ determination. Where possible, the muon endcaps were used, permitting a resolution $\delta\theta$ of order 1mrad to be achieved.

The uncorrected angular distributions for selected events are shown in Figure 4.13. The $\cos\theta^*$ distribution for the 50–60 GeV region was insufficiently populated to enable an asymmetry measurement to be made: both selected events were found to lie in one hemisphere. The data (solid points) are compared to the predicted distributions of Monte Carlo events (open histogram). The feedthrough and background contributions are shown as hatched histograms. Although the statistics are very low, there is reasonable agreement between the data and Monte Carlo and the distributions are noticeably backward-peaked.

Charge mis-assignment is modelled by the Monte Carlo. Figure 4.14 shows the pro-

[b] The assignment of number to the reconstructed muon tracks is made according to the ϕ of the track, which in itself is fairly random.

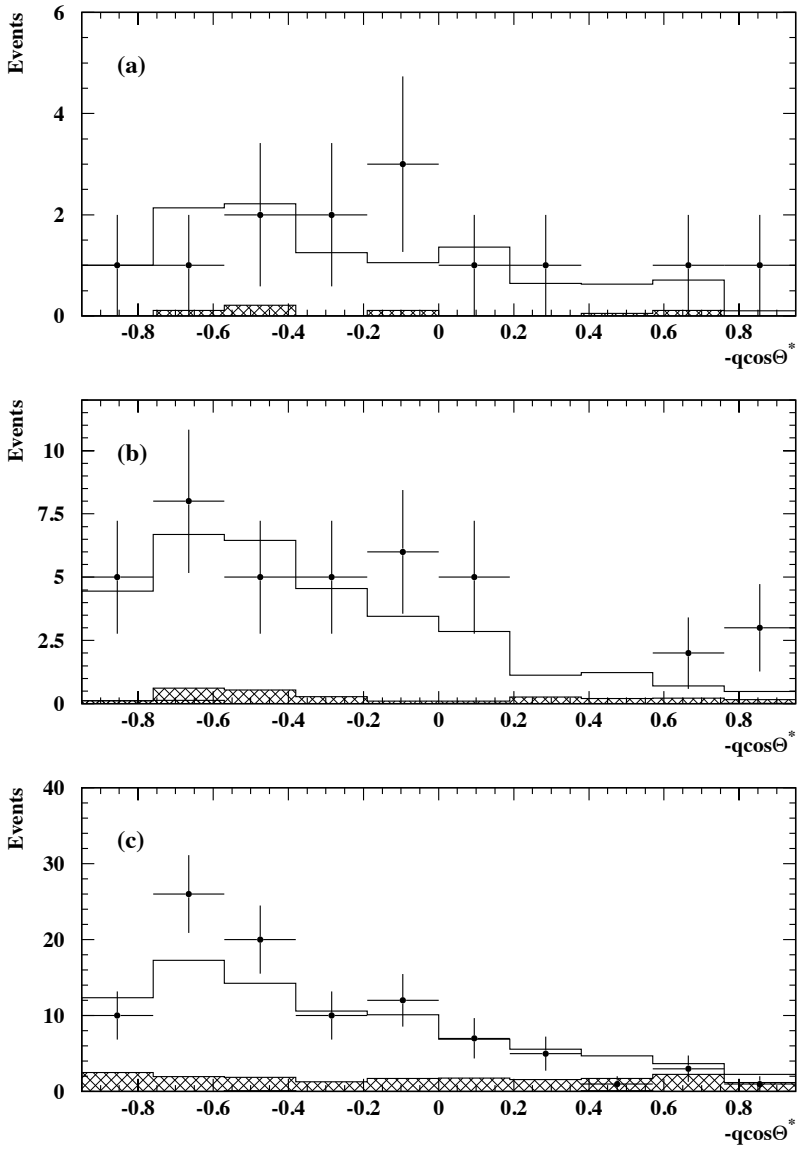

Figure 4.13: The raw angular distributions for (a) the 60–70 GeV region, (b) the 70–80 GeV region and (c) the 80–85 GeV region.

portion of events with the same charge assigned to both tracks for all Monte Carlo muon pair signal events at $\sqrt{s} = 91$ GeV. The quantity $\frac{q}{p}$ is the product of the charge and the

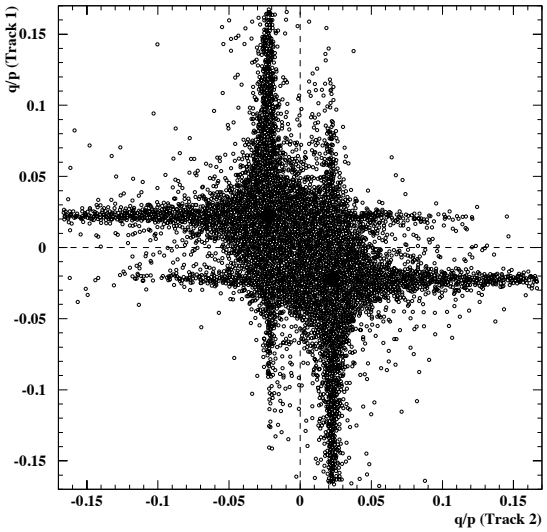

Figure 4.14: The quantity $\frac{q}{p}$ (where p is the momentum and q the charge) for the first muon track plotted against $\frac{q}{p}$ for the second track using all Monte Carlo muon pair signal events at $\sqrt{s} = 91$ GeV.
The top right and bottom left quarters of the plot are the regions that contain events in which both muons are determined as having the same charge.

track curvature measured by the central tracking system. The majority of those events having reconstructed tracks with $q_{track1} = q_{track2}$ typically have high momenta and thus have very little curvature. If tracks have small polar angle they will traverse fewer sense wires in the jet chamber, resulting in less information with which to determine the track curvature as with tracks passing near to the CJ anode wire planes.

Approximately 1.3±0.03% of all data events used in this analysis have mis-assigned track charge. These events were not rejected because discarding such events introduces a very small bias in the measured asymmetry [48]. Instead, other detector information was used to recover most of these events. Firstly, the acoplanarity of the tracks as measured

by the muon chambers was used. For events in which the acoplanarity was measured to be negative and less than 10mrad (*i.e.* events with little final state radiation), the first track was assigned a negative charge. In events that did not satisfy the acoplanarity criteria, either the track with the lowest momentum or the combination of most central detector hits and lowest momentum measurement error, dp, was assigned the negative charge. Approximately 0.3% of these like-sign data events could not be recovered using one of these methods and were rejected. Given that the data statistics is very limited, the exclusion of a very small number of like-sign events has no measurable effect on the asymmetry as any small bias introduced by such rejection is far smaller than the statistical error on the measurement.

The raw angular distributions were corrected for background, feedthrough and efficiency and the corrected distributions are shown in Figure 4.15. The method of efficiency correction, using a distribution of the efficiency as a function of $\cos\theta^*$ derived from full-energy events only (*i.e.* without an $\sqrt{s'}$ selection included), assumes that there is good correlation between $\cos\theta$ measured in the laboratory frame and the rest-frame values. Figure 4.16(a) shows how the muon angles change during transformation to the muon rest-frame for events selected in the 80–85 GeV $\sqrt{s'}$ region from the $\sqrt{s} = 91$ GeV data. There is a strong correlation, with most tracks having very similar $\cos\theta$ and $\cos\theta^*$ values. Figure 4.16(b) shows the distribution of the selection efficiency, derived using Equation 4.5. The numbers of raw and corrected events found in forward and backward hemispheres of the $\cos\theta^*$ distributions, and the asymmetry measurements, are tabulated in Table 4.6. The results are also illustrated in Figure 4.17. An estimation of systematic effects in the selection of events and in angular measurement was performed by following a similar prescription to that used in other analyses of muon events at energies close to the Z° mass. A number of different methods were used to obtain the $\cos\theta$ measurement in the laboratory frame, using different subdetectors, and different requirements were set for some of the quality criteria for these tracks. The selection categories included use of positive tracks instead of negative tracks, imposing additional requirements for numbers of

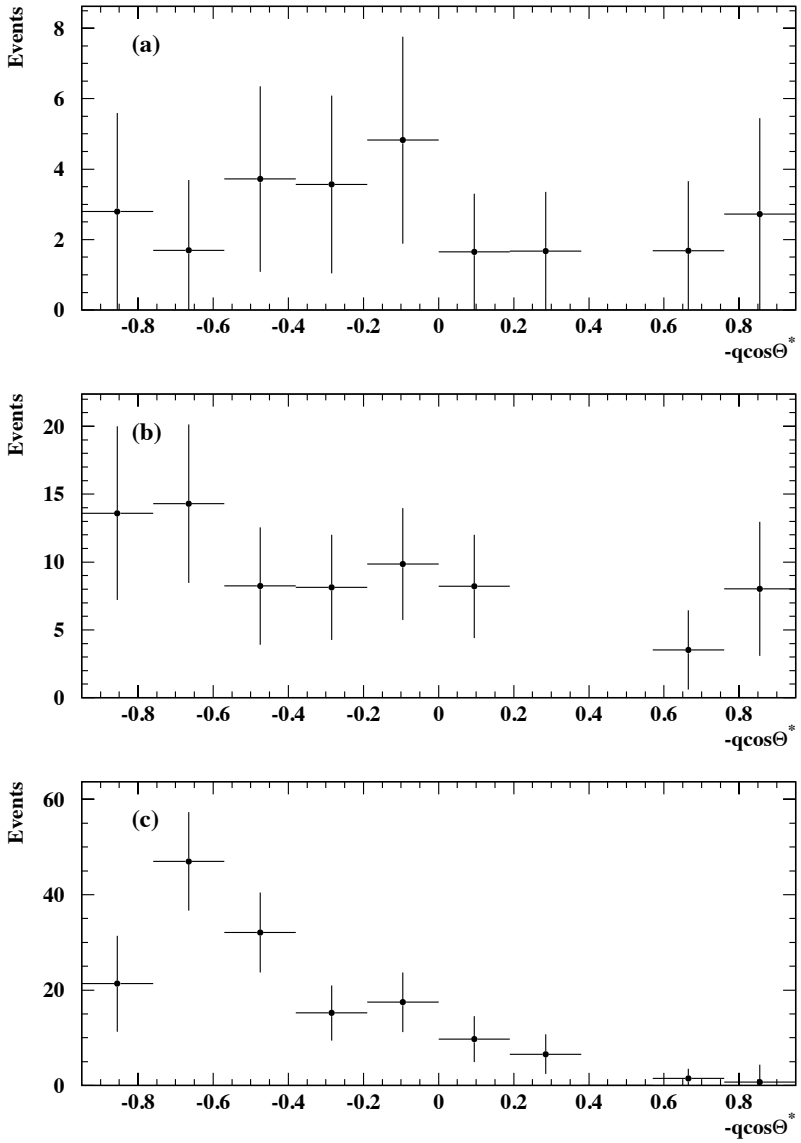

Figure 4.15: The corrected angular distributions for data events in (a) the 60–70 GeV region, (b) the 70–80 GeV region and (c) the 80–85 GeV region.

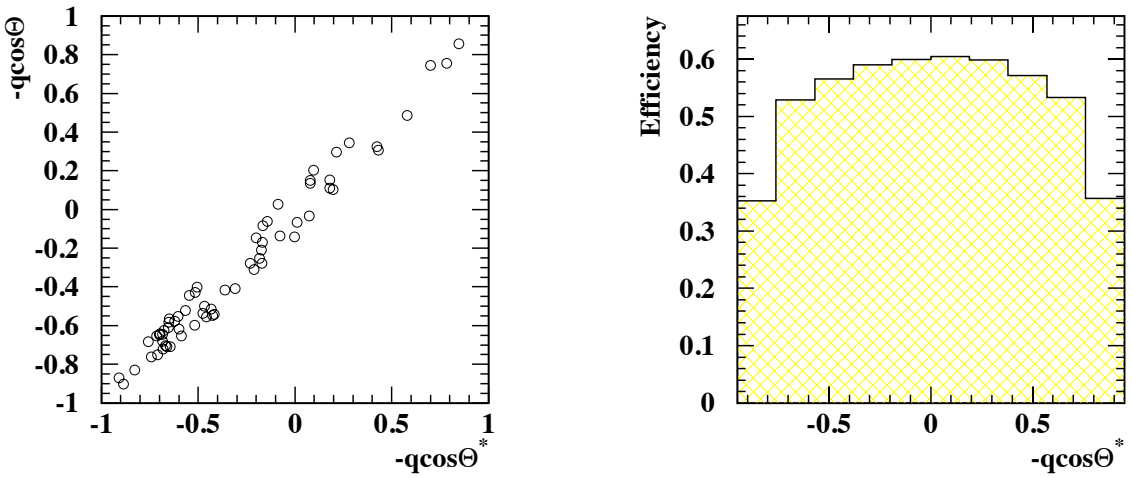

(a) (b)

Figure 4.16: (a) The correlation between laboratory and muon rest-frame $\cos\theta$ measurements for events selected in the 80–85 GeV $\sqrt{s'}$ region, using the $\sqrt{s} = 91$ GeV data only; (b) the binned efficiency distribution as a function of $\cos\theta^*$.

subdetector hits, or using all negative tracks irrespective of their quality. High statistics samples of Monte Carlo signal events were used. The asymmetry was calculated from each of these new angular distributions. The systematic error was obtained by examining the spread of these asymmetries relative to the nominal value. Although the systematic effects from each method are related, a conservative estimate was obtained by combining each of the main contributions in quadrature. A systematic error of ± 0.06 was obtained and is included in the quoted total error on the measured asymmetries.

4.5 Comparison to Other Experiments

Similar analyses to that presented here have been undertaken by ALEPH [49], DELPHI [50] and L3 [51]. Cross-section measurements using radiative events have been made by the

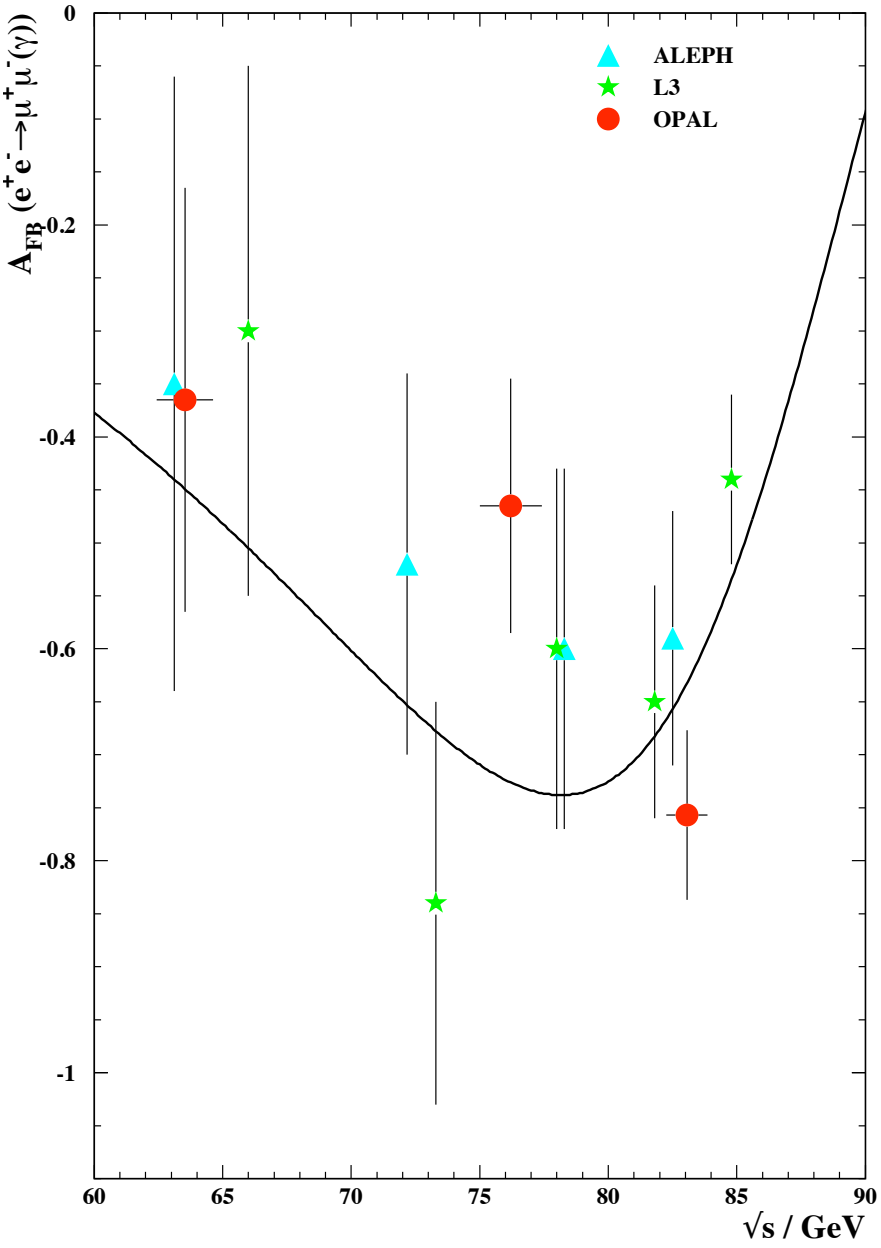

Figure 4.17: The results of the measurements of asymmetries for $e^+e^- \to \mu^+\mu^-(\gamma)$, $A_{FB}(e^+e^- \to \mu^+\mu^-(\gamma))$, made at each of the three energy regions studied. The standard model prediction from ZFITTER is shown as the solid line.

$<\sqrt{s'}>$	Raw data		Corrected data		A_{FB}	A_{FB}^{SM}
(GeV)	$N_{forward}$	$N_{backward}$	$N_{forward}$	$N_{backward}$		
63.53	4	9	7.73	16.59	-0.37±0.20	-0.45
76.21	10	29	19.75	54.11	-0.47±0.12	-0.73
83.10	17	78	18.44	133.06	-0.76±0.08	-0.63

Table 4.6: The numbers of selected data events in the forward and backward hemispheres, N_F and N_B respectively, before and after correction for efficiency, background and feedthrough. The asymmetry at each of the energy points is shown with the expected Standard Model value.

OPAL Collaboration [52] at an average $\sqrt{s'}$ of 75 GeV using a very small data sample corresponding to an integrated luminosity of 7.1 pb^{-1} at centre-of-mass energies between 88 GeV and 94 GeV. The results from the analysis performed by the ALEPH and L3 collaborations compare well to the measurements presented here; DELPHI only present measurements from an exclusive analysis and no comparisons are therefore made to their results. ALEPH present measurements for a range of $\sqrt{s'}$ between 20 and 136 GeV and use data from 1990 to 1992 which adds approximately 15% to the total luminosity. L3 make measurements between 50 and 86 GeV, based on an integrated luminosity of 103 pb^{-1}.

Results of cross-section measurements derived using an explicit radiator function were not presented by any of the other experiments.

Chapter 5

Analysis of $e^+e^- \to \mu^+\mu^-$ Events at $\sqrt{s} = 189$ GeV and $\sqrt{s} = 192$ GeV

The validity of the standard model continues to be tested at the highest energies at LEP. In 1998, data was recorded at 189 GeV and the total recorded luminosity attained in that year was more than the entire luminosity delivered to OPAL during 1990 to 1995. In early 1999, data-taking was resumed at $\sqrt{s} = 192$ GeV with increases in available centre-of-mass energies to above the maximum energy that LEP was designed to achieve following over subsequent months. Significant luminosities were obtained at three other energy points: $\sqrt{s} = 196$ GeV, $\sqrt{s} = 200$ GeV and $\sqrt{s} = 202$ GeV.

This chapter describes the event selection and measurements of cross-sections and forward-backward asymmetries for the process $e^+e^- \to \mu^+\mu^-$ using data recorded during 1998 and 1999 at $\sqrt{s} = 189$ GeV and $\sqrt{s} = 192$ GeV.

5.1 Data Selection

The selection of data events from raw data follows the same principle as for $\sqrt{s} \approx m(Z^\circ)$ data. The major differences are presented in this section.

5.1.1 $Z^\circ \rightarrow \mu^+\mu^-$ Event Preselection

The event preselection for the high-energy ($\sqrt{s} \gg m(Z^\circ)$) data is similar to that at other energies nearer to $\sqrt{s} \approx m(Z^\circ)$. However, some of the preselection cuts are scaled according to $\sqrt{s}$ to ensure as high a selection efficiency as possible and to reduce the amount of non-physics data recorded. The following track and calorimeter requirements are the only differences relative to the preselection of events at lower energies–

1. *Transverse momentum* (p_t)

   The minimum p_t cut requires at least one track with $p_t > 0.0165\ E_{beam}$.

2. *Transverse energy of calorimeter clusters* (E_t)

   Electromagnetic calorimeter clusters must satisfy $E_t > 0.15\ E_{beam}$ GeV.

Either of the above requirements will preselect an event.

5.1.2 Event Vetoes

The track and calorimeter cluster information is used to veto multihadronic events. This criteria is unchanged from the LEP I requirement described in Section 4.2.2. The rejection of cosmic rays follows the method described in Section 4.2.3, using information from the time-of-flight system and measurements of the track parameters near the interaction point.

Figure 5.1(a) shows the time-difference distribution for barrel events with back-to-back TOF counter hits in the data recorded at 189 GeV. There is reasonable separation between the events with -10ns $< \Delta t <$ 10ns and cosmic ray events which have 10ns $< \Delta t <$ 30ns. For all high energy data used in this thesis, the default Δt cut was slightly reduced so that the separation between the signal and cosmic event peaks would be slightly improved. This was done to further reduce the very small contribution from cosmic events remaining in the event sample. Because there are few events in the region between the two Δt peaks, the cut is fairly insensitive to cut position. The new cut was chosen as -10ns $< \Delta t <$ 8ns for the signal events, with events in the region 8ns $< \Delta t <$ 30ns rejected as

cosmics. Figure 5.1(b) shows the distribution of the measured time, t_0, corrected for flight time, for events passing the time difference cut. Figure 5.1(c) shows the t_0 distribution for events in which there is only a single TOF counter hit.

Figure 5.2(a) shows the $\Sigma|d_0|$ versus Σz_0 distribution for barrel events that fail the time-of-flight cuts described in the previous chapter. The cosmic events are scattered throughout the plot, as one would expect. The dashed line indicates the region within which events are recovered by the tight vertex cuts. There are only a few events in this region. Figure 5.2(b) and Figure 5.2(c) show the $\Sigma|d_0|$ versus Σz_0 distributions for events having back-to-back TOF counters or just a single TOF counter hit that pass the TOF cuts. In both of these plots the events are clustered near to the vertex.

Figure 5.2(d) shows the $\Sigma|d_0|$ versus Σz_0 for endcap events. Most events are clustered near to the vertex but a few are distributed throughout the plot. The dashed line indicates the cut. There are not many events close to this boundary but there are a few events scattered inside the box suggesting that some cosmic events remain in the event sample. However, this signal event contamination from cosmic events is still relatively low.

For the high-energy data recorded at $\sqrt{s} = 189$ GeV the tile endcap (TE) subdetector was also used for the first time. The extra timing information provided by the TE detector for events in the endcap regions helps as an additional event veto, especially for cosmic rays. In a similar fashion to the TB timing information, Δt is defined as the difference in times recorded by left and right tiles. The measured time (t_0) distributions for in-time hits are arbitrarily centred on 200ns. Figure 5.3(a) shows the time-difference for all endcap muon pair events recorded at 189 GeV. As expected, most events have Δt centered on zero and these events have both tracks in the endcaps (one left, one right). For events with one track (either left or right) in the barrel and the other in one endcap, it is not possible to use a time-difference cut and so the absolute time from single-hits in the left or right tiles is used instead. These distributions are shown in Figure 5.3(b) and Figure 5.3(c). This independent check using TE confirms that the cosmic contamination from cosmic rays traversing the detector is relatively low. Overall, the distributions

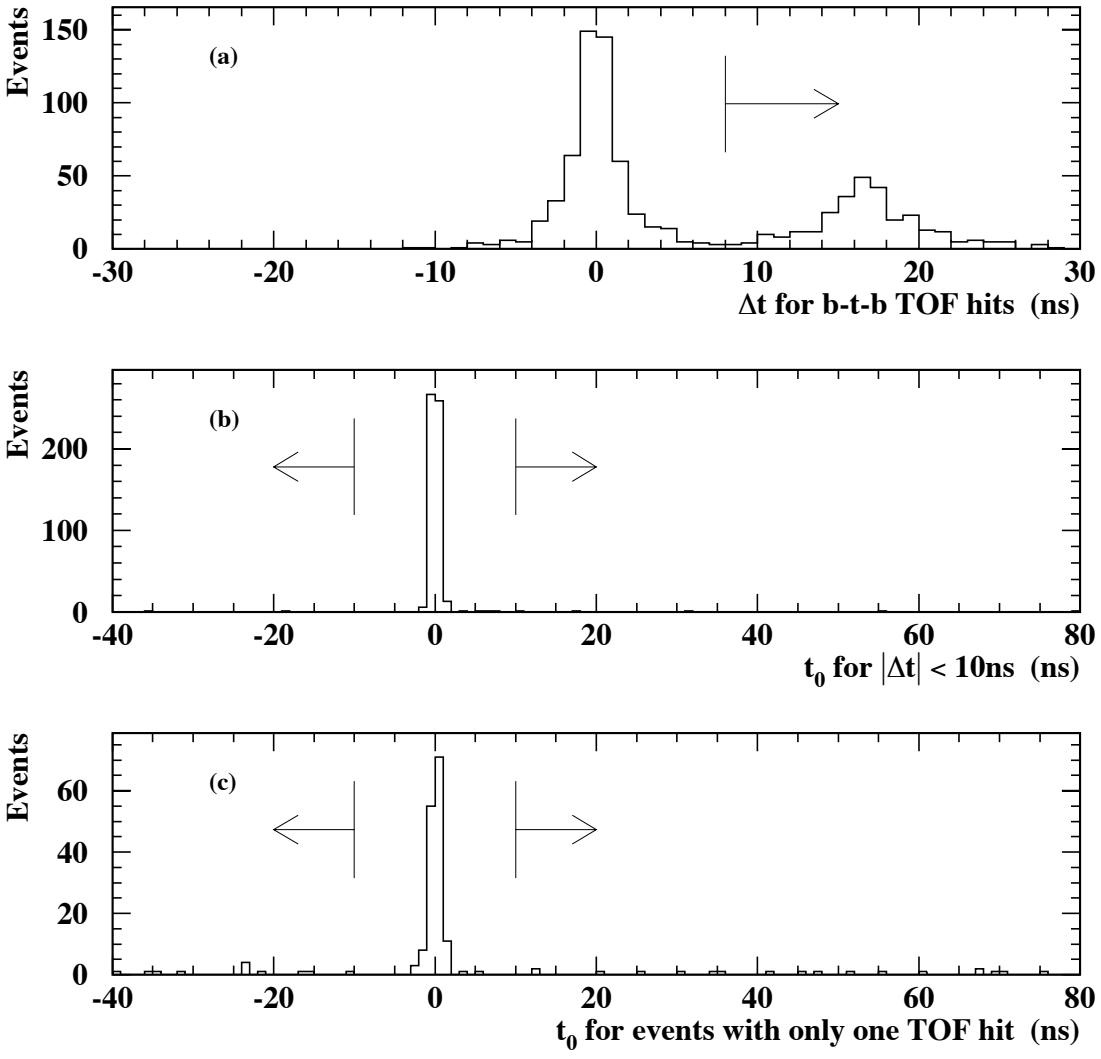

Figure 5.1: Time-of-flight information for the 189 GeV data, showing
(a) the time difference Δt between back-to-back TOF counter hits in the barrel region;
(b) t_0, the measured absolute time, for events passing the Δt cut;
(c) t_0 for events having only a single TOF counter hit.

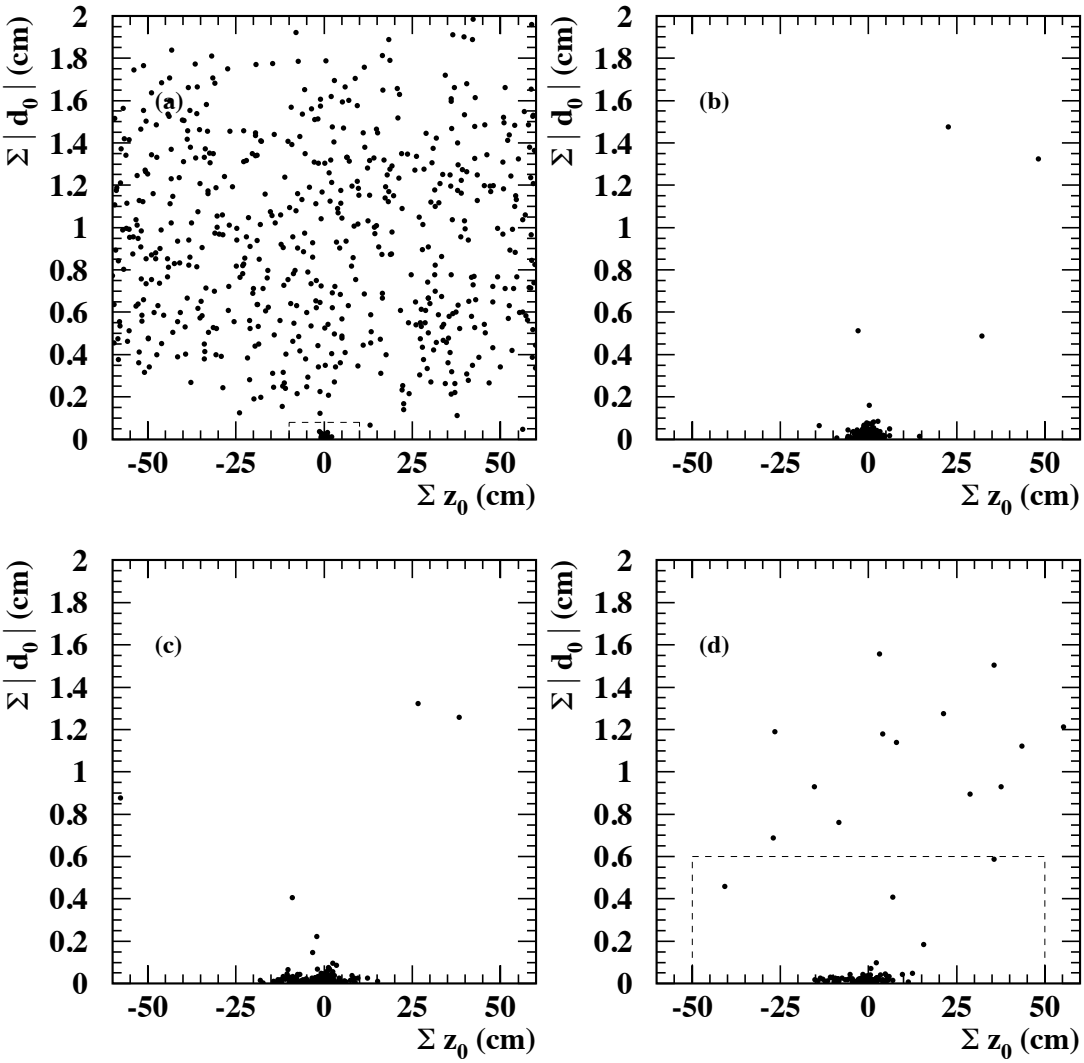

Figure 5.2: Vertex information for the 189 GeV data, showing $\Sigma|d_0|$ versus Σz_0 for
(a) barrel events that fail TOF cuts;
(b) barrel events having back-to-back TOF counter hits that pass TOF cuts;
(c) barrel events that pass the TOF cuts but have only a single TOF counter hit;
(d) events reconstructed in the endcaps.

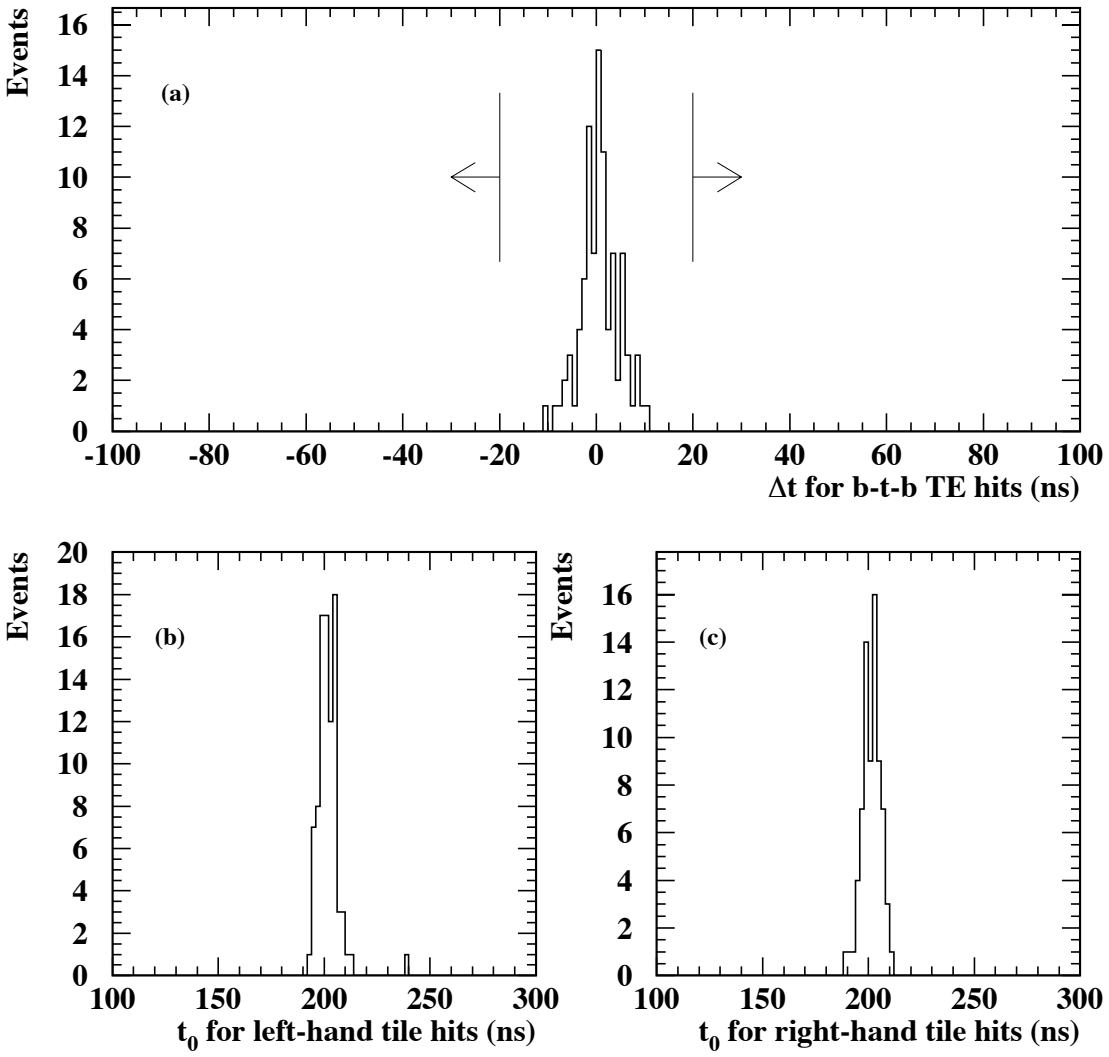

Figure 5.3: Tile endcap (TE) time-of-flight information for the 189 GeV data, showing
(a) the time difference, Δt, between left and right TE tile hits for events where there are hits in both sides of the detector and the hits are back-to-back (the lines show the position of the cut);
(b) the measured time, t_0, for events with hits in left TE tiles only;
(c) the measured time, t_0, for events with hits in right TE tiles only.

indicate that the vertex and time-of-flight information is used effectively, and that the cuts reject most cosmic events cleanly and efficiently. By examining the boundaries of the cuts and looking for events, possible misidentified cosmic events that remain in the final sample are estimated and used to calculate the systematic error in the asymmetry and cross-section measurements.

5.1.3 Effective $\sqrt{s'}$ and Radiative Return

The method for determination of an effective $\sqrt{s'}$ as defined in 4.3.2 is also used with the high-energy data. In this case, the tendency for the incoming lepton beams to radiate a photon is particularly evident as a process called *radiative return* to the Z°. This is very useful because it permits sub-division of the available data according to these classifications –

- A sample containing events which have very little initial state radiation and occur at $\sqrt{s'} \approx \sqrt{s}$, called *non-radiative* events. These are selected by demanding that $s'/s > 0.7225$. The value of this cut was agreed upon by all four LEP experiments to facilitate the combination of results.

- A sample of events which include initial state radiation, called *inclusive* events. These are selected by demanding that $s'/s > 0.01$. This sample includes both events that have initial state radiation and non-radiative events.

Measurements of cross-sections and asymmetries for both of these samples are presented in later sections of this chapter.

5.1.4 Muon Identification and Event Selection

The classification of muon pair events at $\sqrt{s} = 189$ GeV and $\sqrt{s} = 192$ GeV follows that for lower-energy data, described in Section 4.2.4. To reduce the background contamination, particularly from $\tau^+\tau^-$ events, a cut on the the visible energy was introduced into the

91 GeV event selection, with events classified as muons if they had $E_{vis} > 0.6\sqrt{s}$. However, for the high energy data, it was necessary to modify this cut to include the radiative events where there is an undetected, energetic photon. All of the following selection cuts were optimised at other LEP II energies and are used here, unchanged, to maintain consistency with previous results [53]. The motivation for choosing the various cuts is described below.

For events, where all other selection requirements are met, to be classified as muon events, the visible energy cut

$$E_{vis} > 0.35 + \frac{m(\mathrm{Z}^{\circ})^2}{2\mathrm{s}}$$

must be satisfied. The distribution of E_{vis} for muon pair candidates and predicted signal and background from Monte Carlo is shown in Figure 5.4 before the E_{vis} cut is applied. The distribution clearly shows three peaks. For non-radiative events the visible energy fraction is high, with the centre-of-mass energy divided equally between the two back-to-back muons. Thus, the peak situated at $E_{vis} \approx 1$ is due to non-radiative events. The central peak is mostly from radiative events where the emitted photon travels along the $\pm z$ direction and is not detected. The available momentum for each boosted muon is therefore much lower than $\sqrt{s}$ since some of the available energy is carried away by the photon. At higher $\sqrt{s}$ the energy of any emitted photons is larger and causes a shift in the position of the central radiative event peak. The cut position must therefore account for this to maximise the selection efficiency for inclusive events. The region at low E_{vis} is populated by 2-photon background events (*e.g.* $e^+e^- \rightarrow e^+e^-\mu^+\mu^-$). In this case, scattered electrons are emitted at very small angles to the beam direction: only the two muons are detected and the total visible energy is low. By introducing the scaled cut, it is possible to significantly reduce the background contamination while not degrading the efficiency.

Some background and feedthrough events pass the non-radiative event selection, including the visible energy cut. Typically, these events have low invariant mass, $m(\mu^+\mu^-)$,

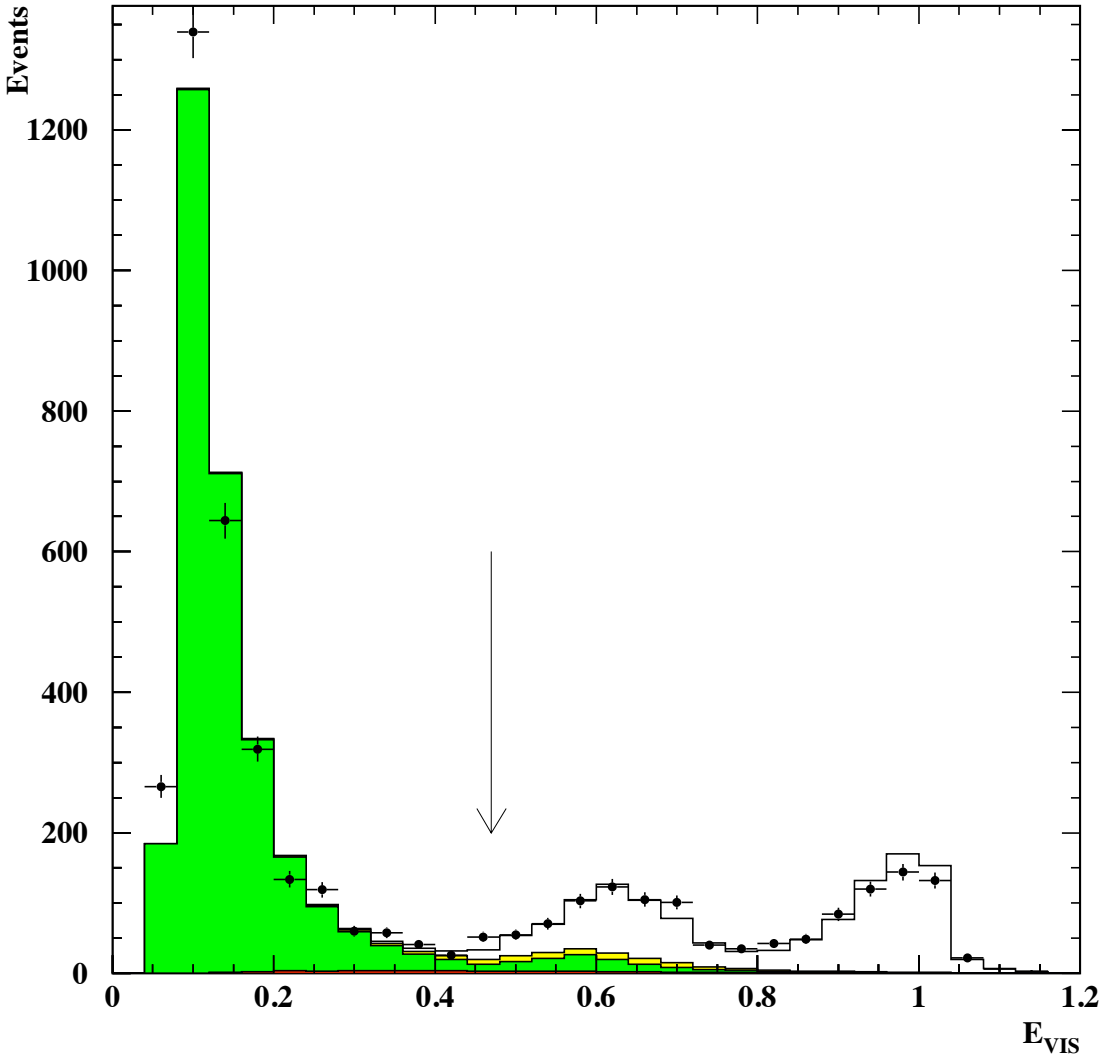

Figure 5.4: The E_{vis} distribution, the visible energy as a fraction of $\sqrt{s}$, for muon candidates in raw data at $\sqrt{s} = 189$ GeV. The points are the data, the open histogram is for Monte Carlo signal events and the grey histogram is the Monte Carlo predicted background. The arrow shows the position of the E_{vis} cut.

and a further cut can be introduced to reduce the number of these events populating the non-radiative sample. The cut

$$m(\mu^+\mu^-) > \sqrt{m(\mathrm{Z}^\circ)^2 + 0.1\mathrm{s}}$$

is positioned slightly above the radiative return peak. Finally, inclusive events must satisfy either of the following cuts

1. $\mathrm{E}_{vis} > 0.75 + \frac{m(\mathrm{Z}^\circ)^2}{2\mathrm{s}}$
2. $m(\mu^+\mu^-) > 70$ GeV.

in addition to the $\mathrm{s}'/\mathrm{s} > 0.01$ cut. This reduces the background contamination in the inclusive event selection.

5.1.5 Data Quality and Luminosity

The detector and trigger status requirements for the muon analysis presented in this chapter are the same as those described in Section 4.2.5. The method for luminosity measurement employs both the forward detector and the silicon tungsten luminosity monitor as with lower-energy data, and uses small-angle Bhabha scattering events. For the data used throughout this chapter, the integrated luminosity and luminosity-weighted mean centre-of-mass energy are listed in Table 5.1. The overall error on the luminosity measurement

Year	$\sqrt{s}$ (GeV)	$\int \mathcal{L}\ \mathrm{d}t$ pb^{-1}
1998	188.63±0.04	180.0±0.39
1999	191.59±0.04	29.2±0.31

Table 5.1: The integrated luminosity and luminosity-weighted mean centre-of-mass energy for the $\sqrt{s} = 189$ GeV and $\sqrt{s} = 192$ GeV data used in this thesis.

at each energy typically amounts to around 0.3%, arising from experimental systematics (∼0.18%), knowledge of the theoretical cross-section implemented in the Bhabha Monte Carlo generator BHLUMI (0.12%) and uncertainty in the beam energy (0.10%). Errors

from the luminosity measurement are included in all the systematic errors on the measured cross-sections.

5.1.6 Muon Trigger Efficiency Calculation

A muon trigger efficiency is derived from the individual efficiencies for each of the subdetectors providing input to the trigger logic. These elements divide the trigger into layers which can be defined when a data-taking run is started. This allows a degree of flexibility in the matching of available trigger signals to run conditions and can be used to cope with background conditions by reducing the trigger rate. Standalone triggers, *i.e.* those that are sufficient in themselves to trigger an event, can be used to estimate the inefficiencies for subdetectors in each layer. Two important categories of event trigger that are required for this are *independent triggers* (event is triggered by a trigger signal independent of the subdetector of interest) and *only triggers* (event is triggered by a signal that is dependent on the subdetector of interest only). To determine the inefficiency due to the track trigger, I_{TT}, the following expression could be used:

$$I_{TT} = 1 - \mathsf{E}_{TT} = \frac{N_{events}(TT_{independent}.NOT(TT_{only}))}{N_{events}(TT_{independent})} \tag{5.1}$$

where E_{TT} is the TT trigger efficiency, and the numerator and denominator of the expression are the numbers of events that have "independent" triggers but not "only" triggers or "independent" triggers alone, respectively. The TO and EM inefficiencies can be calculated in the same way. There are no barrel trigger signals defined that use only the muon chambers because the incident cosmic flux would produce an unmanageable trigger rate. An overall trigger inefficiency is then given by

$$I_{trig} = I_{TT} \times I_{TO} \times I_{EM} \times I_{MU} \tag{5.2}$$

If the trigger inefficiency becomes sizeable, it becomes necessary to introduce corrections to compensate for lost muon events.

5.2 Monte Carlo Samples

The background contamination to the final subset of selected events in the data was estimated using Monte Carlo samples for most of the known processes from which pairs of muons can be observed in the detector. As at $\sqrt{s} \approx m(\mathrm{Z}^\circ)$, these processes include 2-fermion decays of the Z°: $\mathrm{e^+e^-} \rightarrow \mathrm{e^+e^-}$, $\mathrm{e^+e^-} \rightarrow \tau^+\tau^-$ and $\mathrm{e^+e^-} \rightarrow \mathrm{q\overline{q}}$ and 2-γ and four-fermion final states. The percentage of the total background that arises from 2-fermion decays is much higher than the contribution from 2-γ and four-fermion processes. The most dominant backgrounds are $\mathrm{e^+e^-} \rightarrow \tau^+\tau^-$ and $\mathrm{e^+e^-} \rightarrow \mathrm{e^+e^-}\mu^+\mu^-$. Because the centre-of-mass energy is well above the thresholds for $\mathrm{W^+W^-}$ and ZZ production, there is also a very small contribution to the overall background from these processes.

The complete list of event generators used for all background modelling is shown in Table 5.2. All signal event samples were generated using KORALZ with high statistics, subjected to full detector simulation and subsequently treated in the same way as real data. The Monte Carlo samples were generated at centre-of-mass energies, E_{MC}, very close to that of the data, E_{cms}. All Monte Carlo cross-sections were then scaled by a factor E^2_{MC}/E^2_{cms} when the final beam energies were known: because most background contributions come from 2-fermion processes, the use of a $1/s$ scaling term is a reasonable way of scaling the cross-sections. The size of the correction is less than 1% for MC generated at both $\sqrt{s} = 189$ GeV and 192 GeV. Errors in the application of the scaling factors are accounted for in the systematic errors for the cross-sections and asymmetries.

5.2.1 Efficiency of Selection Cuts

The selection efficiency is defined as the ratio of the number of events selected to the number of signal events generated and is determined using the Monte Carlo samples of

Physics Process		Generator
2-fermion	$e^+e^- \to e^+e^-$	BHWIDE
	$e^+e^- \to \mu^+\mu^-$ $e^+e^- \to \tau^+\tau^-$	KORALZ
	$e^+e^- \to q\overline{q}$	PYTHIA
2-γ	$e^+e^- \to e^+e^-\ell^+\ell^-$	VERMASEREN
	$e^+e^- \to q\overline{q}$ tagged	HERWIG
	$e^+e^- \to q\overline{q}$ untagged	PHOJET
4-fermion	$e^+e^- \to e^+e^- f\overline{f}$ $(f\overline{f} \neq e^+e^-)$ $e^+e^- \to f\overline{f}f'\overline{f'}$ $(f\overline{f} \neq f'\overline{f'})$ $e^+e^- \to \ell^+\ell^- q\overline{q}$ $e^+e^- \to \ell^+\ell^-\ell^+\ell^-$ $e^+e^- \to We\nu_e$	GRC4F

Table 5.2: Monte Carlo generators used for producing simulated data and background samples at $\sqrt{s} = 189$ GeV and $\sqrt{s} = 192$ GeV. In the 4-fermion section, $f\overline{f}$ and $f'\overline{f'}$ refer to any pairs of fermions while $\ell^+\ell^-$ refers to any pair of leptons. The 2-γ samples where the scattered e^+ or e^- is detected are described as *tagged* samples.

signal events. The selected and the generated events must both satisfy the $\sqrt{s'}$ cut that classifies the inclusive or non-radiative sample. There are therefore two discrete values of the overall efficiency. The efficiencies primarily correct measurements for the geometric acceptance of the detector.

The efficiencies for the inclusive and non-radiative event selections are listed in Table 5.3. The efficiency for the non-radiative events is high. There is little difference between the 189 GeV and 192 GeV efficiencies since the cuts are the same. The resolution of the Z° peak is slightly less well defined as the separation between the radiative and non-radiative peaks increases, *i.e.* as $\sqrt{s}$ increases and the non-radiative efficiency therefore decreases with $\sqrt{s}$.

The systematic error on the efficiency was calculated using high-statistics Z° data and Monte Carlo. To do this, the E_{vis} cut was relaxed slightly to avoid cutting too harshly into the Z° peak and the modified selection applied to both the Monte Carlo and data.

The number of events selected in the data was compared to the number of events selected from Monte Carlo and the percentage difference was used as the systematic error on the efficiencies. The same technique was used for both the 189 GeV and the 192 GeV analyses.

Four-Fermion Correction to Selection Efficiency

Four-fermion processes of the type $e^+e^- \to \mu^+\mu^- f\overline{f}$ (where $f\overline{f}$ can be any pair of fermions) form a significant fraction of the total background. Both s-channel and t-channel four-fermion production can occur, and the s-channel process, where a radiated initial state photon produces a $\mu^+\mu^-$ pair, can be considered to be signal. This is because this study of lepton-pair final states measures the s-channel vertex in e^+e^- annihilation. These processes are depicted in Figure 5.5. The inclusive and non-radiative efficiencies are

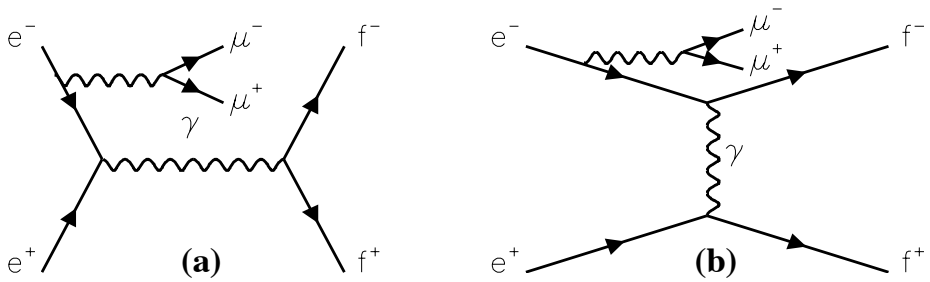

Figure 5.5: Feynman diagrams for (a) s-channel and (b) t-channel four-fermion processes.

corrected to include these "signal-like" events [54]. The small correction is derived from studying simulated four-fermion events that are classified as signal events by satisfying all of the following kinematic requirements—

- The invariant mass of the muon pair, $m(\mu^+\mu^-)$, must be greater than the invariant mass of the $f\overline{f}$ system, $m(f\overline{f})$. In addition, $m(f\overline{f})$ must be less than 70 GeV.

- The s′/s cut must also be satisfied. Hence $m(\mu^+\mu^-)^2 > 0.01s$ for the inclusive events or $m(\mu^+\mu^-)^2 > 0.7225s$ for the non-radiative events.

These cuts were also used for previous muon pair analyses at LEP II.

5.2.2 Backgrounds and Feedthrough

To determine the background contributions, the selection cuts are applied to the Monte Carlo samples for each background process. Feedthrough events are those that have a generated $\sqrt{s'}$ that is below the value of the non-radiative s′/s > 0.7225 cut and is determined using the signal Monte Carlo. A feedthrough correction is not relevant for the inclusive selection. The number of events that are selected as feedthrough or background are expressed as a visible crossection according to the expression

$$\sigma_{bgrnd/feed} = \frac{N_{selected}}{N_{generated}} \sigma_{generated}$$

and used to correct the data cross-sections. The $\cos\theta$ distributions of background and feedthrough events are used to correct the data angular distributions used for the asymmetry determination.

The background and feedthrough estimates for the analyses are shown in Table 5.3. The predicted background cross-sections for the main background sources in the 192 GeV analysis are listed in Table 5.4. At 189 GeV and 192 GeV, the total background contribution amounts to only 6.2% of the selected inclusive sample. For the 189 GeV analysis, about 2.7% of the events come from 2-photon $e^+e^- \rightarrow e^+e^-\mu^+\mu^-$ decays where the e^+ and e^- disappear along the beampipe. Two-fermion τ-pair events account for 1.4% of the events, while other processes which result in visible muons, mostly four-fermion and 2-photon channels, contribute to the remainder. In the non-radiative sample, the background only accounts for 2.3% of the events selected. For these events, only backgrounds with a back-to-back topology are likely to be mis-identified as muon events. Thus, 1%

$\mathbf{s'/s > 0.01}$			
$\sqrt{s}$ (GeV)	Efficiency (%)	Background (pb)	Feedthrough (pb)
188.63	75.4±0.8	0.39±0.11	–
191.59	73.8±0.8	0.37±0.11	–
$\mathbf{s'/s > 0.7225}$			
$\sqrt{s}$ (GeV)	Efficiency (%)	Background (pb)	Feedthrough (pb)
188.63	88.7±0.9	0.07±0.03	0.060±0.003
191.59	88.8±0.9	0.08±0.03	0.059±0.004

Table 5.3: The selection efficiencies, backgrounds and feedthrough for the 189 GeV and 192 GeV analyses. Both the inclusive and non-radiative numbers are shown.

		σ (pb)	
		s′/s > 0.01	s′/s > 0.7225
2-fermion	$e^+e^- \to \mu^+\mu^-$	–	0.066±0.005
	$e^+e^- \to \tau^+\tau^-$	0.0934±0.0038	0.0338±0.0023
2-photon	$e^+e^- \to e^+e^-\mu^+\mu^-$	0.1867±0.0140	0.0146±0.0039
	$e^+e^- \to e^+e^-\tau^+\tau^-$	0.0011±0.0011	0.0000±0.0000
4-fermion	$e^+e^- \to e^+e^-\mu^+\mu^-$	0.0215±0.0021	0.0016±0.0006
	$e^+e^- \to e^+e^-\tau^+\tau^-$	0.0007±0.0004	0.0002±0.0002
	$e^+e^- \to \ell^+\ell^-q\overline{q}$	0.0018±0.0006	0.0002±0.0002
	$e^+e^- \to \ell^+\ell^-\ell^+\ell^-$	0.0646±0.0036	0.0253±0.0023

Table 5.4: The predicted background cross-sections at 192 GeV. Only the background processes which contribute to the inclusive and non-radiative muon pair selections are shown.

of the events come from back-to-back $e^+e^- \to \tau^+\tau^-$ events. Final-state $\ell^+\ell^-\ell^+\ell^-$ and 2-photon processes contribute the remaining 1.3%.

For the 192 GeV analysis, the proportion of the events coming from the various background processes is similar to that at 189 GeV with the largest contributions from 2-photon (3.1% of selected events) and $e^+e^- \to \tau^+\tau^-$ (1.6%). The background to the non-radiative selection at 192 GeV is 2.6% of all events, with $e^+e^- \to \tau^+\tau^-$ events accounting for 1.2% of the events. The relative size of the backgrounds at 192 GeV are not very different to those at 189 GeV because the cross-sections of these processes do not change appreciably over this small energy range. The systematic error on each of the background sources was obtained using distributions of quantities measured in the detector. For many of the backgrounds studied, the E_{vis} distribution was used. Cuts used to reject the background of interest were relaxed; the E_{vis} distribution for data was compared to that of the Monte Carlo prediction over a region where the background was observed to dominate. An example is shown in Figure 5.6. The number of data events in the region indicated was compared to the number of Monte Carlo events. The percentage difference between these datasets was taken as the systematic error for this background. The statistical error on the data was used if this was larger. Using this method, the systematic error on the $e^+e^- \to e^+e^-\mu^+\mu^-$ background was determined as 5.1%. Less significant background processes were conservatively assigned a 50% systematic error.

Because of the increasing separation between the full-energy and radiative return peaks, the feedthrough contamination decreases with $\sqrt{s}$. For analyses at both energies, the feedthrough is small. The systematic error on the feedthrough was determined by comparison of the measured feedthrough contribution using the normal $s'/s > 0.7225$ cut to the sizes of the feedthrough obtained with the cut shifted up or down by a small amount. These upper and lower cut values were $s'/s > 0.75$ and $s'/s > 0.65$.

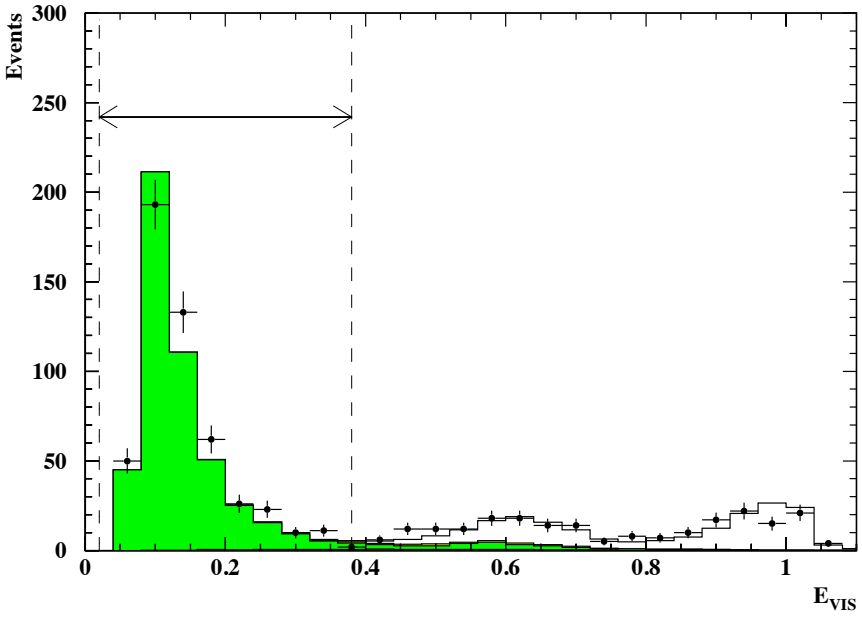

Figure 5.6: The distribution of E_{vis} used for determining the systematic error on the $e^+e^- \rightarrow e^+e^-\mu^+\mu^-$ background at $\sqrt{s} = 192$ GeV.

.

5.2.3 Initial/Final State Photon Interference

The $\sqrt{s'}$ is defined as the effective centre-of-mass energy of the e^+e^- collision after initial state radiation. The presence of final state photons cannot be excluded and the interference between initial and final states introduces extra terms in the matrix elements used for calculating cross-sections. The definition of the $\sqrt{s'}$ therefore becomes ambiguous. The KORALZ Monte Carlo generator used for muon pair generation and for efficiency determination does not have a comprehensive treatment of interference, permitting only a simple calculation of the interference term assuming single-photon emission only (from initial and final states). Interference from multiple photons is not included. Comparisons between data and Monte Carlo would obviously be inaccurate unless the treatment of interference

was made consistent. Using ZFITTER, which allows theoretical predictions to be made with or without interference included, the interference contribution was calculated and used to correct the data for interference effects. These corrections to the cross-section and asymmetry are very small and are listed for 189 GeV in Table 5.5. The cross-sections and

	$\mathbf{s'/s > 0.01}$	$\mathbf{s'/s > 0.7225}$
$\Delta\sigma/\sigma_{\rm SM}(\mu\mu)$ (%)	-0.42±0.05	-1.4±0.4
$\Delta A_{\rm FB}(\mu\mu)$	-0.0054±0.0007	-0.016±0.004

Table 5.5: The applied corrections to the cross-sections and asymmetries at 189 GeV necessary to remove the effect of initial/final state interference. The correction to the cross-section is expressed as a fraction of the standard model predicted cross-section. The absolute value of the correction is shown for the asymmetry. The errors shown are the statistical errors due to the selection efficiency used when determining an interference cross-section.

asymmetry measurements presented in this thesis from data at $\sqrt{s}$ = 189 GeV and $\sqrt{s}$ = 192 GeV are both corrected for the presence of interference in the data which allows comparison to the Monte Carlo which excludes interference.

5.3 Analysis of Data Events

The selections described in the previous sections were applied to preselected muon pair candidates at $\sqrt{s} = 189$ GeV and $\sqrt{s} = 192$ GeV. For the inclusive and non-radiative data subsets, the cross-sections, angular distributions of the muons in the laboratory frame and the forward-backward asymmetries were determined.

The $\sqrt{s'}$ distributions are shown in Figure 5.7. Overall there is good agreement between the data and the predictions from the Monte Carlo. The radiative return peak (at $\sqrt{s'} \approx m(\mathrm{Z}^\circ)$) and the $\sqrt{s'} \approx \sqrt{s}$ peak are well-defined.

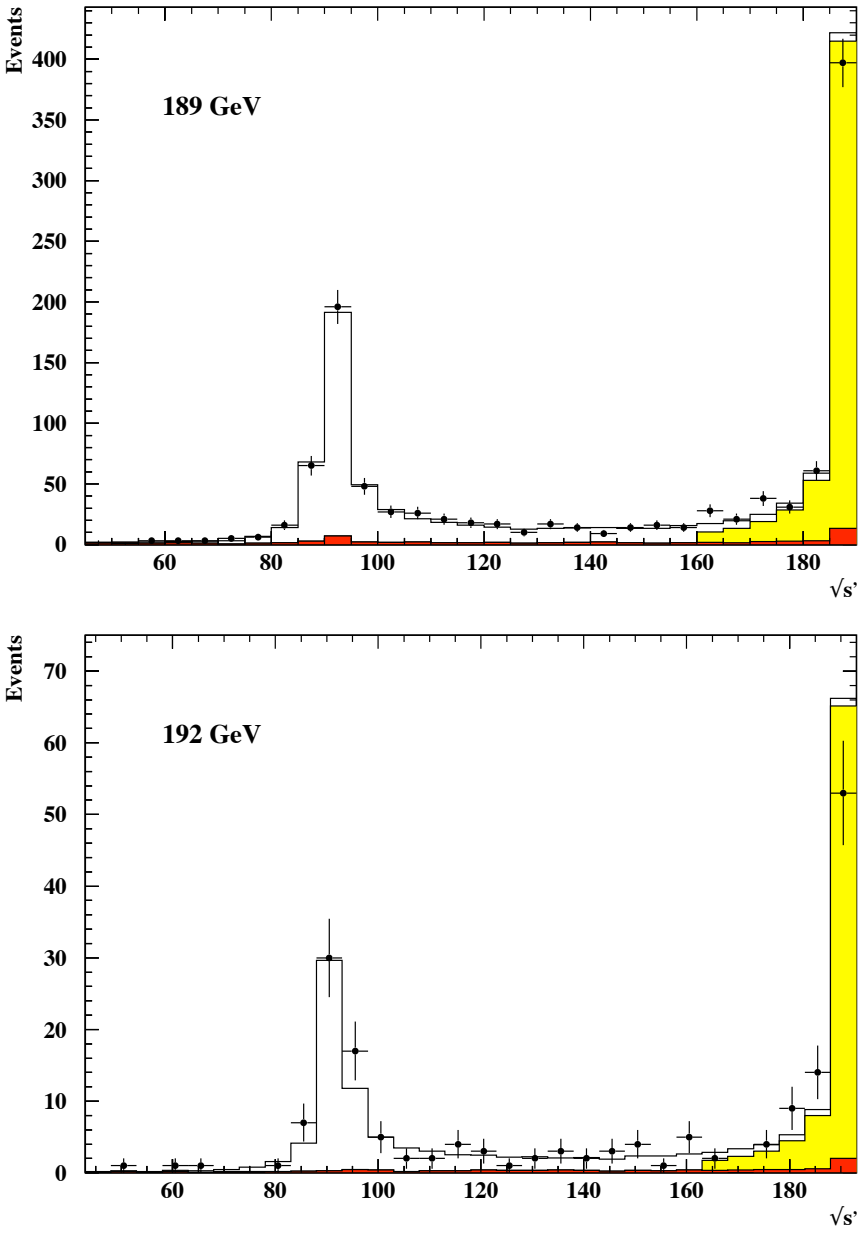

Figure 5.7: The $\sqrt{s'}$ distributions for the $\mu^+\mu^-$ events in the 189 and 192 GeV data. The points are data, the open histogram is the Monte Carlo prediction and the dark grey histogram is the predicted background. The light grey histogram is the Monte Carlo prediction for the true $s'/s > 0.7225$ events.

5.3.1 Measurements of the $e^+e^- \rightarrow \mu^+\mu^-$ Cross-section

The cross-sections, σ, for the two event samples are obtained by using the numbers of events, N_{events}, and the integrated luminosity of the data, $\mathcal{L}$. The cross-sections for the background (σ_{bgd}), feedthrough (σ_{feed}) and interference corrections (σ_{intcor}) are subtracted before an overall efficiency correction (E) is applied. Thus, the final cross-sections for the data are obtained from

$$\sigma = \frac{\frac{N_{events}}{\mathcal{L}} - \sigma_{bgd} - \sigma_{feed} - \sigma_{intcor}}{\mathsf{E}} \tag{5.3}$$

where all of the cross-sections are expressed in pb. The measured cross-sections are illustrated in Figure 5.8 and tabulated in Table 5.6. The measured cross-sections are in

$s'/s > 0.01$

$\sqrt{s}$ (GeV)	N_{events}	σ (pb)	σ^{SM} (pb)
188.63	1129	7.77±0.23±0.18	7.76
191.59	177	7.62±0.57±0.28	7.49

$s'/s > 0.7225$

$\sqrt{s}$ (GeV)	N_{events}	σ (pb)	σ^{SM} (pb)
188.63	527	3.11±0.14±0.06	3.21
191.59	80	2.89±0.32±0.20	3.10

Table 5.6: The corrected cross-sections for muon pair events at $\sqrt{s} = 189$ GeV and $\sqrt{s} = 192$ GeV, and theoretical predictions obtained from a standard model calculation. The first error is statistical and the second is systematic.

good agreement with the predicted standard model cross-sections for both the inclusive and non-radiative data samples.

The total systematic error on the cross-section measurements is determined from the individual contributions to the overall systematic error. These contributions arise from the statistical and systematic errors for feedthrough, background, luminosity, efficiency and interference corrections. The statistics available at $\sqrt{s} = 189$ GeV were far higher than

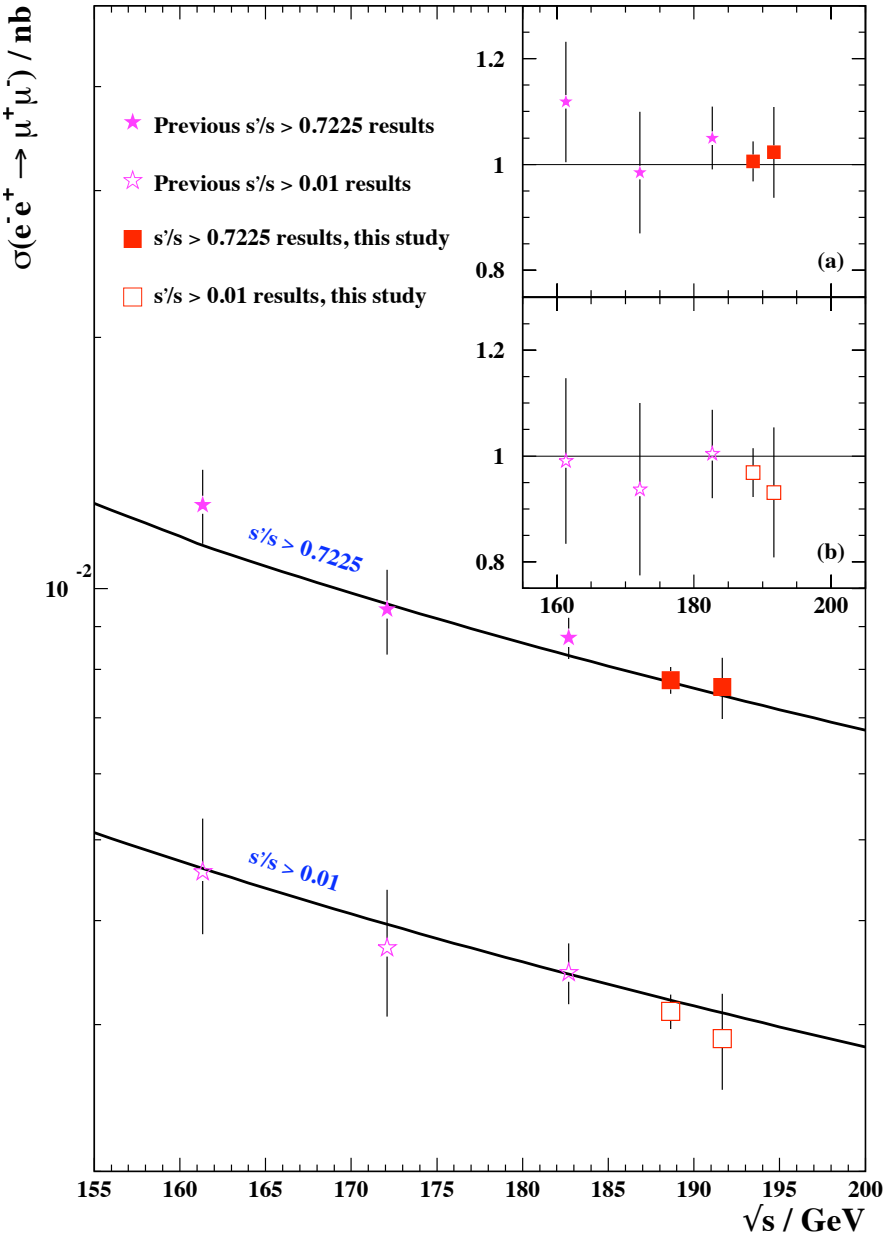

Figure 5.8: The cross-section measurements as a function of $\sqrt{s}$. Similar measurements made at previous energies [53] are shown for comparison. The inset shows the ratio of the measurements to the standard model prediction for (a) non-radiative and (b) inclusive events. The solid lines in the main figure show the theoretical predictions.

that obtained at any previous energy point. Because the statistical errors were therefore much lower, it was important to focus attention on the various sources of systematic effects and try to reduce them. One of the dominant sources of systematic error to the cross-section measurement is from contamination of the data event sample with cosmic events. The cosmic events remain in the sample because they satisfy either the time-of-flight or vertex selection criteria. In order to assign an error for these events, one must first assess the proportion of the selected events that are actually from cosmic rays. This was achieved by varying the cuts used in cosmic rejection and counting the number of events that were accepted, close to these cut boundaries. For barrel events, the time-of-flight cuts were varied and for endcap events, vertex association cuts were varied. The systematic error was derived using Equation 5.3 with the number of data events increased by the number of events obtained from the studies of the cuts. The systematic error obtained is shown in Table 5.7, which also lists the systematic errors from the other sources. The cosmic

	$s'/s > 0.01$		$s'/s > 0.7225$	
$\Delta\sigma$(Source)	189 GeV	192 GeV	189 GeV	192 GeV
$\Delta\sigma(\Delta\mathsf{E}_{stat})$	0.016	0.020	0.006	0.007
$\Delta\sigma(\Delta\sigma_{bgrd_{stat}})$	0.019	0.020	0.005	0.006
$\Delta\sigma(\Delta\sigma_{feed_{stat}})$	–	–	0.003	0.004
$\Delta\sigma(\Delta\mathsf{E}_{syst})$	0.078	0.076	0.031	0.029
$\Delta\sigma(\Delta\sigma_{bgrd_{syst}})$	0.151	0.136	0.033	0.035
$\Delta\sigma(\Delta\sigma_{feed_{syst}})$	–	–	0.002	0.005
$\Delta\sigma(N_{cosmic})$	0.037	0.230	0.031	0.193
$\Delta\sigma(\Delta\mathcal{L}_{stat})$	0.007	0.016	0.003	0.006
$\Delta\sigma(\Delta\mathcal{L}_{syst})$	0.016	0.018	0.006	0.007
$\Delta\sigma(\Delta\sigma_{intcor})$	0.003	0.003	0.012	0.011
$\Delta\sigma_{stat}$	0.2316	0.5737	0.1364	0.3249

Table 5.7: The systematic errors that contribute to the overall systematic error on the cross-section measurements. The error in pb for each source of the systematic error is shown for both the inclusive and non-radiative cross-sections. The statistical errors on the data are also listed.

systematic error is approximately six times larger at 192 GeV than at 189 GeV. This

is due to statistical fluctuations in the number of events near the cosmic rejection cuts, rather than as a result of differences in the structure of the time-of-flight distributions.

Additional studies of the muon trigger efficiency for muon pairs and possible mis-modelling of detector effects due to the CJ anode regions were undertaken. The technique described in Section 5.1.6 for determining trigger efficiencies was used to study trigger effects in data events at $\sqrt{s} = 189$ GeV. Because non-radiative events tend to have a back-to-back topology, the sets of trigger signals that trigger these types of event will normally be collinear. Figure 5.9 shows the number of triggers that fired per event for

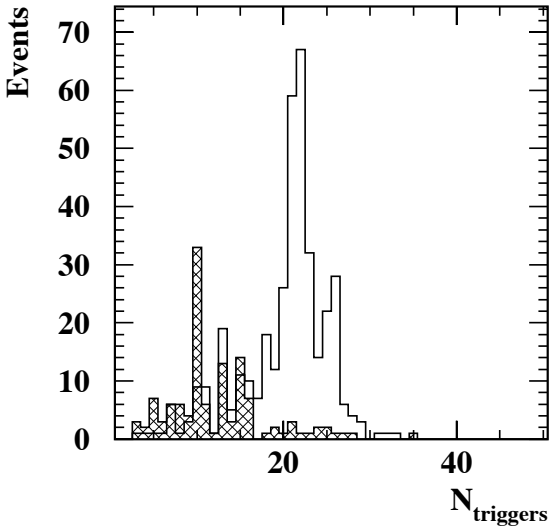

Figure 5.9: The number of triggers fired per non-radiative event at 189 GeV. The open histogram is for non-radiative events that have barrel triggers and the hatched histogram is for events having endcap triggers.

non-radiative events selected at 189 GeV. The selected events were divided according to the region of the detector in which both muon tracks were found. The time-of-flight system in the endcap (TE) was used to provide the endcap triggering information. The efficiencies for each subdetector are listed in Table 5.8. This result compares well with

	E_{barrel} (%)	E_{endcap} (%)
Track Trigger, TT	99.963±0.009	99.920±0.025
ECAL Trigger, EM	99.860±0.017	99.331±0.041
TOF Trigger, TO/TE	99.879±0.017	99.883±0.010
Muon Trigger, MU	–	99.754±0.038
Combined	99.9994±0.0002	99.9985±0.0006

Table 5.8: Estimates of trigger efficiencies, determined using 189 GeV data, for important subdetectors. These numbers are based on a study of collinear triggers and are divided into barrel and endcap regions. The combined results are obtained as the product of the components.

an alternative study using the theta-phi matrix information [55], which gave an overall efficiency of 99.92% using non-radiative events only. The magnitude of the inefficiency from the trigger presented above equates to a change in the non-radiative cross-section of less than 10^{-4} pb which is far smaller than the systematic errors on the cross-section. Therefore, no corrections have been included.

If a charged-particle track passes close to an anode plane of the central jet chamber, there is the possibility that the track may be poorly reconstructed. This results in the appearance of a split track. Different treatment in Monte Carlo relative to data would introduce a bias because data results are corrected using the Monte Carlo. If this effect were not modelled in the simulated data, one would expect a deficiency in the number of events in the ϕ regions near to the anode planes and hence a poorer efficiency in that region. Since the anode planes are centered in each of the 15° ϕ sectors, this would occur at $mod(\phi, 15°)$ of 7.5°. For the 189 GeV data, this was checked by obtaining ϕ distributions of tracks reconstructed in each sector of the jet chamber. To improve the statistics in the distribution, both tracks were used and all sectors were combined. The distribution is shown in Figure 5.10. There are no obvious spikes in the distribution near to the wire planes and the data and Monte Carlo agree fairly well. Therefore, no correction was included for tracking effects.

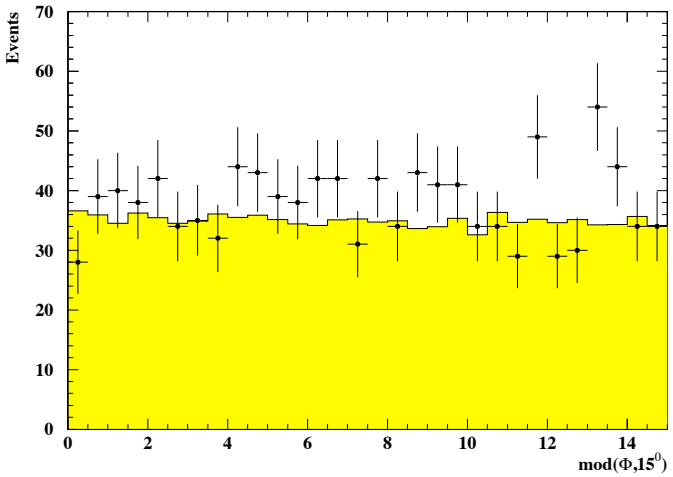

Figure 5.10: Distribution of 189 GeV data events per 15° ϕ sector in the jet chamber. The grey histogram is the Monte Carlo distribution and the points represent the data. All sectors, and both muon tracks, are combined on the plot.

5.3.2 Asymmetry Measurements and Angular Distributions

For the selected inclusive and non-radiative events, the uncorrected angular distributions at 189 GeV and 192 GeV are shown in Figure 5.11. The predicted distributions from Monte Carlo are also shown, as are the distributions for the feedthrough and background events. The points represent the data, with the statistical errors indicated. The agreement between the data and the predicted distributions for both $s'/s > 0.01$ and $s'/s > 0.7225$ events is reasonable, at both $\sqrt{s} = 189$ GeV and $\sqrt{s} = 192$ GeV. The quality criteria for tracks used for these measurements generally follows that for asymmetry measurements at OPAL at lower collision energies. The $\cos\theta$ is considered to be reliably determined for tracks in which there are at least three hits in the CV stereo wires and three hits in the CZ chambers. If tracks do not have sufficient hits in these subdetectors, the muon chambers are used for the $\cos\theta$ measurement if available. For example, this would occur in the case of tracks that are outside the acceptance of the barrel region where there would be no CZ hits (*i.e.* at $\cos\theta > 0.7$). Events with insufficient CV or CZ hits and having no

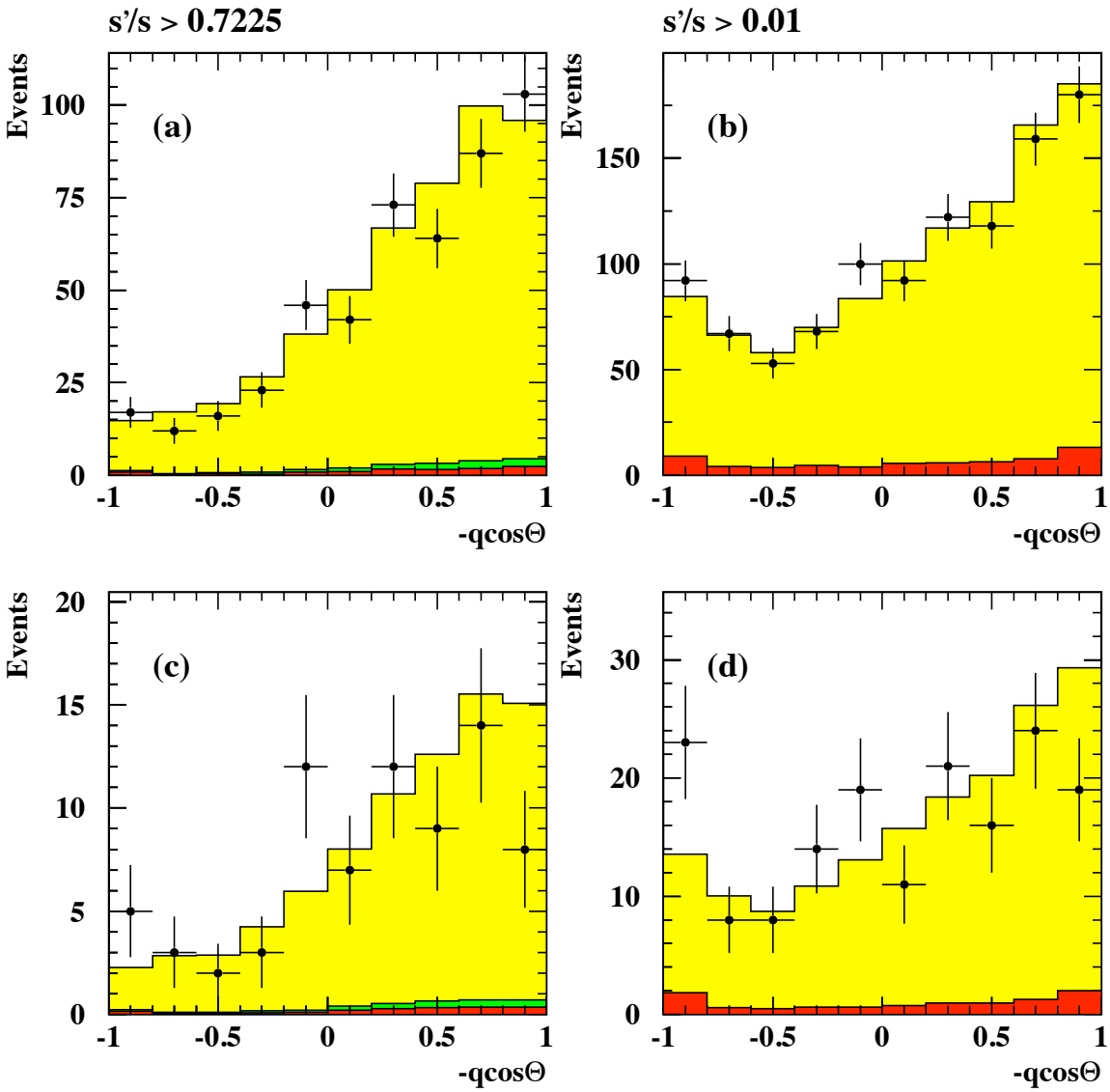

Figure 5.11: The angular distributions for data events selected in the inclusive and non-radiative samples at $\sqrt{s}$ = 189 GeV (a,b) and $\sqrt{s}$ = 192 GeV (c,d). The light grey histogram is for signal Monte Carlo events, the dark grey histogram is the predicted background and feedthrough distribution and the points represent the data.

muon chamber $\cos\theta$ measurement available are rejected. For all data used in this study, approximately $\frac{1}{3}$ of the CV stereo wires were inoperable. Although this introduces an inefficiency in the detector operation, this problem is well-modelled in all Monte Carlo samples used herein.

Charge-misassignment can also occur in the reconstruction of high-energy muon tracks and affects less than 2% of selected Monte Carlo events. The same approach to improving the knowledge of the track charge in such events in the $\sqrt{s} \approx m(\mathrm{Z}^{\circ})$ data can be used here, employing the acoplanarity and momentum studies described in Section 4.4.3. These techniques recover more than 80% of like-sign events in both the 189 GeV and 192 GeV Monte Carlo samples.

Prior to determining the asymmetry from the angular distributions, the background and feedthrough contributions need to be subtracted. The $\cos\theta$ dependence of the efficiency must also be corrected for as follows. The simulated charge-signed $\cos\theta$ distributions are obtained for the selected events of the inclusive and non-radiative event samples, covering the angular region $-1.0 < \cos\theta < 1.0$. Each $\cos\theta$ distribution is sub-divided into forty bins of equal width. The distribution is compared to that obtained using all simulated events, before application of any selection cuts. In this way, a bin-by-bin efficiency distribution is obtained, as illustrated in Figure 5.12 for the inclusive and non-radiative samples at $\sqrt{s} = 189$ GeV.

The selection efficiency for the non-radiative events is symmetric about $-q\cos\theta = 0$. The efficiency for selecting non-radiative events is higher than for inclusive events. Angular distributions of inclusive events include these non-radiative events: in the backward region of these distributions, there is a mixture of non-radiative and radiative events which has a different proportion of radiative events than the forward region. The radiative events are less forward-peaked (there are relatively more radiative events in the region $-1.0 < \cos\theta < 0$ than $0 < \cos\theta < 1.0$) and these have a lower asymmetry. Hence, the overall efficiency for this class of event is lower in the backward hemisphere.

There is a marked lowering of the efficiency for both samples in the regions between

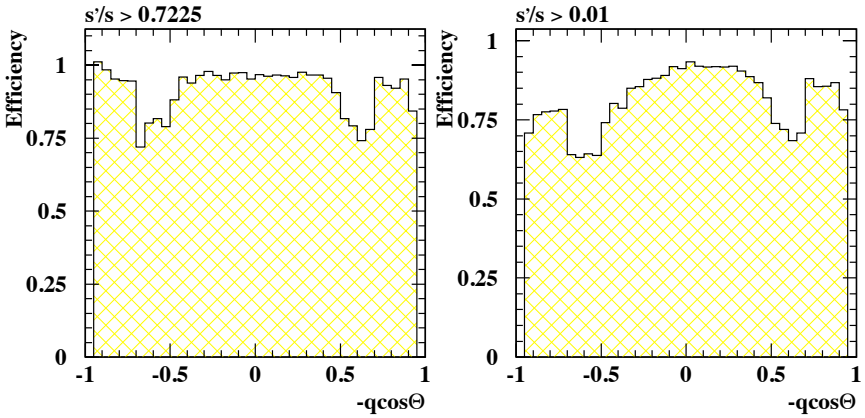

Figure 5.12: The bin-by-bin efficiency distributions as a function of -$q\cos\theta$ at $\sqrt{s} = 189$ GeV.

.

the geometric acceptance of the barrel and endcap, at $0.6 < \cos\theta < 0.7$. In this region there is reduced detector coverage because of the necessity for cabling access and structural supports. The small effect of initial/final state interference is calculated using ZFITTER and is applied as a bin-by-bin correction to the number of data events. The predicted distribution for non-$e^+e^- \rightarrow \mu^+\mu^-$ events selected from background processes is then subtracted; for the non-radiative events, a correction is also made for the feedthrough events which have a $\sqrt{s'}$ below the s′/s cut. The final step is to correct each $\cos\theta$ bin by dividing by the associated selection efficiency in that bin. The corrected angular distributions for the 189 GeV data are shown in Figure 5.13.

Radiative events are produced back-to-back in the rest-frame of the Z° but not in the laboratory. After emission of initial state radiation, the angles of the two muon tracks are modified by the effect of the boost from the photon. The tracks will no longer be back-to-back and there will no longer be a correlation between the occupied $\cos\theta$ bins. The asymmetry measurement could be affected by the dependence of the charge-signed

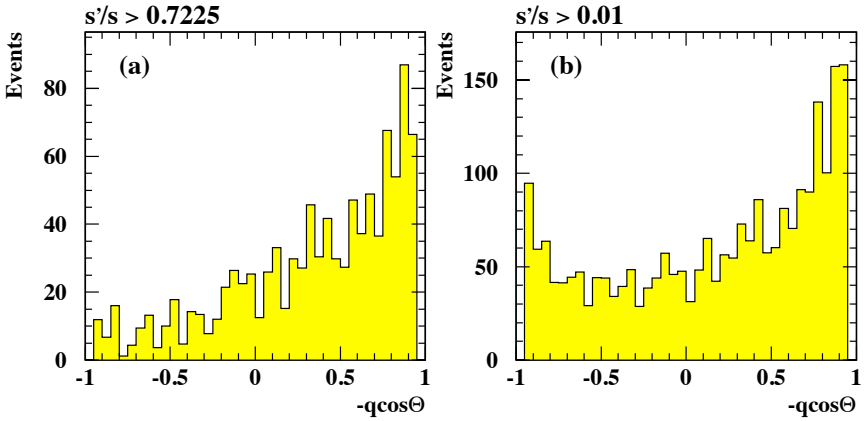

Figure 5.13: The corrected angular distributions for $\sqrt{s} = 189$ GeV data.

$\cos\theta$ on which muon track was chosen because each muon track could have a different background/efficiency correction. Rather than assuming that the effect of any small biases on an event-by-event basis average out, the chance of such an occurrence can be minimised by using the angular information for both muon tracks. The asymmetry measurement presented here uses the counting method.

The statistical error on A_{FB} is usually obtained using the Binomial distribution. However, the expression for the error must be modified since the efficiency is not uniform across all bins in $\cos\theta$ [59]. The error is given by

$$\Delta A_{FB}^2 = \frac{4\sqrt{2}}{N_T^4}(N_B^2 \sum \frac{\Delta N_{F_i}^2}{\mathsf{E}_{F_i}^2} + N_F^2 \sum \frac{\Delta N_{B_i}^2}{\mathsf{E}_{B_i}^2}) \tag{5.4}$$

where N_F, N_B and N_T are the total number of events in the forward hemisphere, the backward hemisphere and the complete angular distribution respectively, after corrections for background and efficiency. The numbers of raw events per bin in the forward and backward hemispheres are denoted by N_{F_i} and N_{B_i}; E_{F_i} and E_{B_i} are the efficiency corrections applied to bin i in the respective hemispheres. The asymmetry measurements for the

angular acceptance -0.95 < $\cos\theta$ < 0.95 must be corrected to the full angular acceptance -1.0 < $\cos\theta$ < 1.0. This is achieved using a correction factor obtained from the predicted asymmetries for these acceptances calculated using ZFITTER. At 189 GeV, these correction factors amount to 0.969 and 1.027 for the inclusive and non-radiative asymmetries respectively. The measured asymmetries are listed in Table 5.9 and illustrated in Figure 5.14.

$s'/s > 0.01$

$\sqrt{s}$	Raw data		Corrected data		A_{FB}	A_{FB}^{SM}
(GeV)	$N_{forward}$	$N_{backward}$	$N_{forward}$	$N_{backward}$		
188.63	1364	744	1525.11	893.11	$0.25^{+0.03}_{-0.04}\pm0.00$	0.28
191.59	189	139	210.55	167.73	$0.11^{+0.08}_{-0.13}\pm0.00$	0.28

$s'/s > 0.7225$

$\sqrt{s}$	Raw data		Corrected data		A_{FB}	A_{FB}^{SM}
(GeV)	$N_{forward}$	$N_{backward}$	$N_{forward}$	$N_{backward}$		
188.63	740	231	762.96	242.06	$0.53^{+0.04}_{-0.06}\pm0.01$	0.57
191.59	96	50	96.67	52.60	$0.30^{+0.12}_{-0.24}\pm0.01$	0.56

Table 5.9: The forward-backward asymmetry, A_{FB}, for $e^+e^- \to \mu^+\mu^-$ at $\sqrt{s}$ = 189 GeV and $\sqrt{s}$ = 192 GeV, and theoretical predictions obtained from a standard model calculation using ZFITTER. The first error is statistical and the second is systematic.

To estimate the systematic error, the same approach to that used in the asymmetry analysis described in the previous chapter was followed: different methods were used to derive the $\cos\theta$ used in the angular distributions, specifically

§1 using central tracking detectors for $\cos\theta$ in the barrel region, and reject events where there are insufficient subdetector hits.

§2 always using the $\cos\theta$ measured using the central tracking system, without imposing any track quality cuts.

§3 using the normal method but with the additional requirement that *both* tracks have at least 3 hits in CV stereo wires and in the z-chambers.

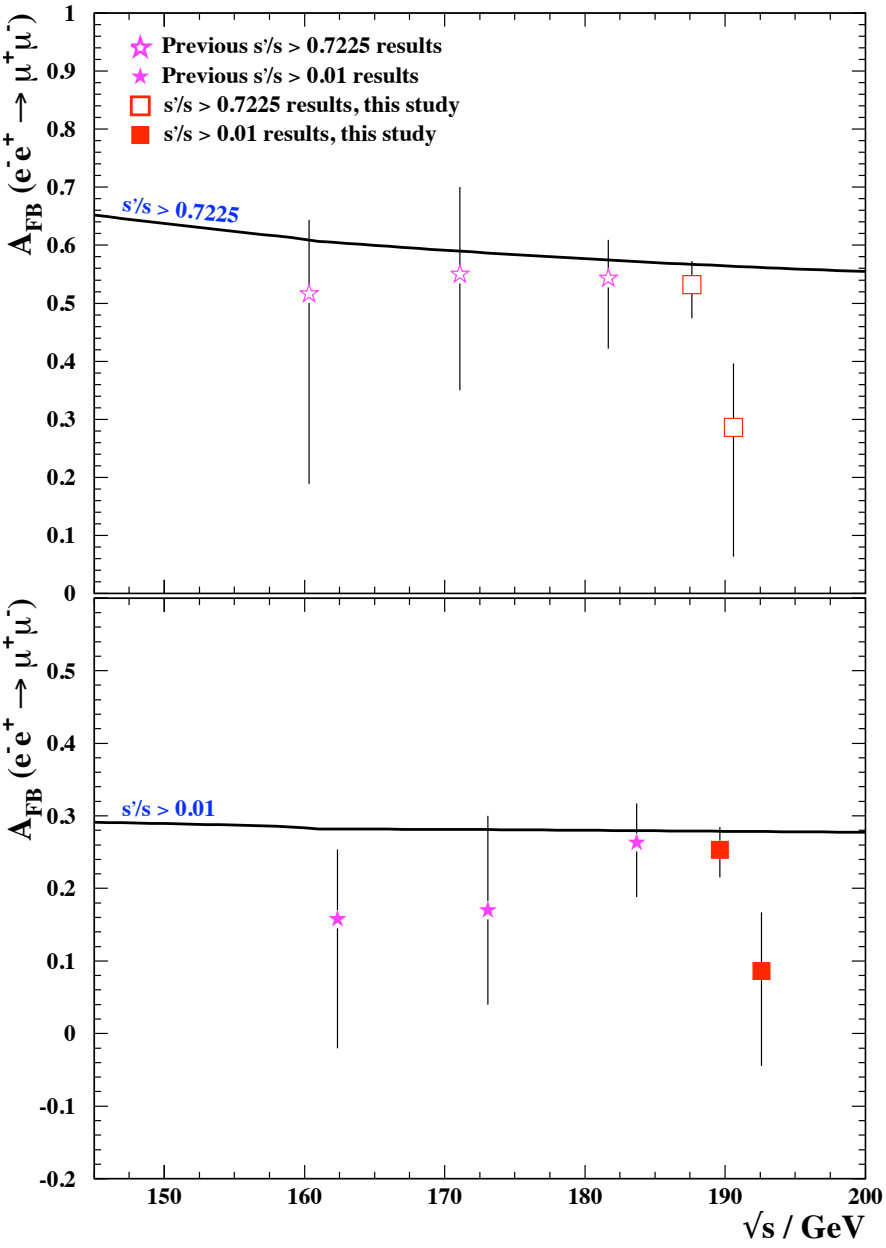

Figure 5.14: The forward-backward asymmetry, A_{FB}, for $e^+e^- \to \mu^+\mu^-$ at $\sqrt{s} = 189$ GeV and $\sqrt{s} = 192$ GeV. Similar measurements made at previous energies [53] are shown for comparison. The solid lines are the theoretical predictions.

Low data statistics limited the precision of these checks and therefore, since the Monte Carlo models the data reasonably well, simulated signal events were used. The asymmetry measurement obtained in the normal way was compared to those values obtained using the methods described above to derive a systematic error.

The method used for asymmetry measurement was tested at both $\sqrt{s} = 189$ GeV and $\sqrt{s} = 192$ GeV using Monte Carlo signal events, treated as real data. The Monte Carlo samples were divided into two, with one half of the events used to determine the efficiency and the other half used to form angular distributions and obtain asymmetry measurements. Feedthrough and efficiency corrections were applied to the selected event distributions in the usual way. The measurements were repeated with the Monte Carlo event subsets reversed. At 189 GeV, the asymmetries obtained for the inclusives and non-radiatives were 0.283±0.006 and 0.566±0.006 respectively. At 192 GeV, the asymmetries were 0.287±0.007 ($s'/s > 0.01$) and 0.567±0.009 ($s'/s > 0.7225$). Both sets of measurements show consistency with the data and theoretical predictions; one can therefore conclude that this method of measurement is relatively bias-free. As a further check, only the negative muon tracks were used in a repeated measurement using the 189 GeV Monte Carlo, performed in exactly the same way as described above. The asymmetries obtained for the inclusives and non-radiatives were 0.280±0.008 and 0.565±0.01 respectively. This result demonstrates that the decision to use the information from both tracks and averaging is compatible with the result using only single tracks.

5.3.3 Comparison to Other Experiments

The results presented in this chapter for inclusive and non-radiative event samples compare well with similar measurements performed by ALEPH [56], DELPHI [57] and L3 [58]. The s'/s cut used by DELPHI and L3 for separating their non-radiative sample is $s'/s > 0.7225$, as presented here; ALEPH, however, choose $s'/s > 0.81$ and use standard model calculations (*e.g.* from ZFITTER) to correct the measurements to $s'/s > 0.7225$. The efficiency

for the DELPHI non-radiative event selection is typically of order 90%– approximately 2% higher than that presented here; their inclusive selection is defined as $\sqrt{s'} > 75$ GeV. DELPHI also use kinematic fitting and likelihood selections based on expected topologies of tracks and detected photons to determine $\sqrt{s'}$ and therefore obtain smaller estimates for feedthrough contamination.

ALEPH have slightly higher non-radiative selection efficiency but similar inclusive efficiency. Backgrounds are at a similar level in both event samples; a value for the feedthrough is not quoted. L3 have much lower efficiencies for both event selections, and have higher feedthrough and background contributions.

5.4 Concluding Remarks

Efforts to describe observable physical phenomena have resulted in a theory from which very precise predictions have been made. Testing the standard model has been the major goal of experimental particle physics at LEP for the past eleven years and has been achieved by studying the s-channel production of the electromagnetic and weak gauge bosons, the photon and the Z°, and subsequent decays to 2-fermion final states. The production of all leptonic final states is described theoretically in terms of electroweak observables. Two important observables, the cross-section (σ) and the forward-backward asymmetry (A_{FB}), can be measured experimentally and used to verify the underlying theory. Precision measurement of lepton-pair production therefore provides a useful way to probe for evidence of new physics beyond the theoretical framework. Muon pairs provide a very clean signal for such studies.

In this thesis, two analyses have been presented. Using a significant fraction of the data recorded using the OPAL detector during 1993-1995, the LEP I era, studies of cross-sections and asymmetries were performed using $e^+e^- \to \mu^+\mu^-$ events that had undergone initial-state radiation, such that energy regions below the nominal LEP energy could be accessed. The measurements using these $e^+e^- \to \mu^+\mu^-(\gamma)$ events were made at effective centre-of-mass energies, $\sqrt{s'}$, between 50 and 85 GeV.

Measurements of the cross-sections and forward-backward asymmetries for $e^+e^- \to \mu^+\mu^-$ were also made using data recorded at $\sqrt{s} = 189$ GeV and $\sqrt{s} = 192$ GeV. At the higher LEP energies, there is a tendency for radiative return to the Z° peak. The high-energy "non-radiative" $e^+e^- \to \mu^+\mu^-$ events were selected separately to permit studies of observables at the highest possible energy, in addition to an "inclusive" measurement where all events were used, including those that had undergone initial-state radiation.

Both analyses presented in this thesis produced results that were consistent with the standard model expectations and comparable to the results from other LEP experiments. This provides further evidence for the success of the standard model in describing electroweak interactions.

References

[1] F. Halzen and A.D. Martin, "*Quarks and Leptons : An Introductory Course in Modern Particle Physics*", John Wiley & Sons (1984).

[2] CDF Collaboration, F. Abe *et al.* , Phys. Rev. Lett. **74** (1995) 2626.
D0 Collaboration, S. Abachi *et al.* , Phys. Rev. Lett. **74** (1995) 2632.

[3] R.P. Feynman, "*Quantum Electrodynamics*", Benjamin (1961).

[4] D.H. Perkins, "*Introduction to High Energy Physics, Fourth Edition*", Addison Wesley (2000).

[5] H. Fritsch, M. Gell-Mann and H. Leutwyler, Phys. Lett. **B47** (1973) 365.

[6] G. 't Hooft, Nucl. Phys. **B33** (1971), 173; Nucl. Phys. **B35** (1971) 167.

[7] M. Kobayashi and T. Maskawa, Prog. Theor. Phys. **49** (1973) 652.

[8] R.M. Barnett *et al.* , "*Review of Particle Physics*", Physical Review **D54** (1998).

[9] S.L. Glashow, Nucl. Phys. **22** (1961) 579.
A. Salam, in : "*Elementary Particle Theory*", *ed.* N. Svartholm, Almqvist and Wikel (1968) 361.
S. Weinberg, Phys. Rev. Lett. **19** (1967) 1264.

[10] P.W. Higgs, Phys. Rev. Lett. **13** (1964) 508.

[11] ALEPH, DELPHI, L3 and OPAL Collaborations, "*Searches for Higgs bosons: Preliminary combined results using LEP data collected at energies up to 202 GeV*", **CERN-EP/2000-055** (2000).

[12] ALEPH, DELPHI, L3 and OPAL Collaborations, "*Combination of Preliminary Electroweak Measurements and Constraints on the Standard Model*", **CERN-PPE/97-54** (1997).

[13] D. Karlen, "*Experimental Status of the Standard Model* ", OPAL Conference Note CR-385 (1998).

[14] The Super-Kamiokande Collaboration, Phys. Rev. Lett. **81** (1998) 1562.

[15] S. Myers and E. Picasso, Contemp. Phys. **31** (1990) 387.

[16] ALEPH Collaboration, Nucl. Instr. and Meth. **A294** (1990) 121.

[17] DELPHI Collaboration, Nucl. Instr. and Meth. **A303** (1991) 233.

[18] L3 Collaboration, Nucl. Instr. and Meth. **A289** (1990) 35.

[19] OPAL Collaboration, Nucl. Instr. and Meth. **A305** (1991) 275.

[20] P.P. Allport *et al.* , Nucl. Instr. and Meth. **A386** (1997) 23;
P.P. Allport *et al.* , Nucl. Instr. and Meth. **A346** (1994) 476;
P.P. Allport *et al.* , Nucl. Instr. and Meth. **A324** (1993) 34.

[21] J.R. Carter *et al.* , Nucl. Instr. and Meth. **A286** (1990) 99;
J.M. Roney *et al.* , Nucl. Instr. and Meth. **A279** (1989) 236.

[22] R.D. Heuer and A. Wagner, Nucl. Instr. and Meth. **A265** (1988) 11;
H.M. Fischer *et al.* , Nucl. Instr. and Meth. **A252** (1986) 492.

[23] H. Mes *et al.* , Nucl. Instr. and Meth. **A265** (1988) 445.

[24] G. Aguillion *et al.* , Nucl. Instr. and Meth. **A417** (1998) 266.

[25] A. Ji-Gang *et al.* , Nucl. Instr. and Meth. **A267** (1988) 386.

[26] P. Mättig, "*Photon Energy Resolution in the Lead Glass Calorimeters*", OPAL Technical Note TN-324 (1995).

[27] C. Beard *et al.* , Nucl. Instr. and Meth. **A286** (1990) 117.

[28] R.M. Brown *et al.* , IEEE Trans. Nucl. Sci. **30** (1983) 479;
M. Akrawy *et al.* , Nucl. Instr. and Meth. **A290** (1990) 76.

[29] A.H. Ball *et al.* , IEEE Trans. Nucl. Sci. **37** (1990).

[30] J. Allison *et al.* , Nucl. Instr. and Meth. **A236** (1985) 284.

[31] G.T.J. Arnison *et al.* , Nucl. Instr. and Meth. **A294** (1990) 431.

[32] D.C. Imrie *et al.* , Nucl. Instr. and Meth. **A238** (1989) 515.

[33] B.E. Anderson *et al.* , IEEE Trans. Nucl. Sci. **41** (1994) 845.

[34] M. Arignon *et al.* , Nucl. Instr. and Meth. **A313** (1992) 103.

[35] C. Hawkes *et al.* , "*ROPE User Guide (V4.09)*", OPAL Offline Note OFFL-0487 (1995).

[36] R. Cranfield *et al.* , "*OPALCAL 506 User Guide*", OPAL Offline Note OFFL-0036 (1992).

[37] S. Jadach, B.F.L. Ward, and Z. Was, Comp. Phys. Comm. **66** (1991) 276.

[38] T. Sjöstrand, Comp. Comm. **82** (1994) 74;
M. Bengtsson and T. Sjöstrand, Comp. Phys. Comm. **43** (1987) 367;
Nucl. Phys. **B289** (1987) 810.

[39] S. Jadach, W. Placzek, M. Skrzypek, B. F. L. Ward and Z. Was, Comput. Phys. Comm. **119** (1999) 367.

[40] J. Allison *et al.* , Nucl. Instr. and Meth. **A317** (1992) 47.

[41] D. Bardin *et al.* , "*ZFITTER–An Analytical Program for Fermion Pair Production in* e^+e^- *Annihilation*", **CERN-TH-6443/92** (1992).

[42] R. Barlow *et al.* , "*A Detailed Description of the 1991 Muon Pair Analysis*", OPAL Technical Note TN-109.

[43] T. Smith *et al.* , "*The LL Processor in ROPE*", OPAL Internal Note (1995).

[44] J.A.M. Vermaseren, Nucl. Phys. **B229** (1983) 347.

[45] T. Smith, P. Watkins and A. Watson, "*Analysis of Muon Pair Events at LEP1.5*", OPAL Technical Note TN-341.

[46] J. Kirk, "*Monte Carlo Studies of Muon Pair Analysis at 161 GeV*", OPAL Technical Note TN-396.

[47] G. Altarelli *et al.* . (Eds.) "*Z Physics at LEP1 v1: Standard Physics*", CERN 89-08 (1989).

[48] P. Bright-Thomas, P. Clarke, "*Systematic Effects in the Measurement of Leptonic Forward-Backward Charge Asymmetry*", OPAL Technical Note TN-287.

[49] Aleph Collaboration, R. Barate *et al.* , **CERN-PPE/97-10** (1997).

[50] Delphi Collaboration, P. Abreu *et al.* , **CERN-PPE/97-45** (1997).

[51] L3 Collaboration, M. Acciarri *et al.* , **CERN-PPE/96-24** (1996).

[52] Opal Collaboration, P.D. Acton *et al.* , **CERN-PPE/91-155** (1991).

[53] OPAL Collaboration, G. Abbiendi *et al.* , Eur. Phys. J. **C6** (1999) 1.
OPAL Collaboration, K. Ackerstaff *et al.* , Eur. Phys. J. **C2** (1998) 441.

[54] OPAL Collaboration, K. Ackerstaff *et al.* , **CERN-PPE/97-101** (1997).

[55] P. Ward, *Private communication.*

[56] ALEPH Collaboration, "*Fermion Pair Production in e+e- Collisions at 189 GeV and Limits on Physics Beyond the Standard Model*", submitted to the International Europhysics Conference on High-Energy Physics, Tampere, Finland (1999).

[57] DELPHI Collaboration, P. Abreu *et al.* , **CERN-EP/2000-068** (2000).

[58] L3 Collaboration, M. Acciarri *et al.* , **CERN-EP/99-181** (1999).

[59] S.D. Talbot, "*Production of Muon and Tau Pairs Using the OPAL Detector at LEP*", Ph.D. Thesis, University of Birmingham (1998).